The University Of Sheffield.

INSIGNEO Institute for *in silico* Medicine

Extended Discrete Element Method for subject specific modelling and analysis of the ankle joint contact mechanics

Ivan Benemerito

A thesis submitted in partial fullfillment of the requirements
for the degree of
Doctor of Philosophy

The Department of Automatic Control and Systems Engineering
The University of Sheffield
Sheffield, UK

Supervisors: Dr Lingzhong Guo
Prof Damien Lacroix

August 2018

Abstract

Osteoporosis related bone fractures and osteoarthritis affect the lifes of millions of people in the world and constitute a significant burden on the healthcare systems of several countries. It is believed that mechanical factors such as excessive joint loading during daily activities might play a role in their onset. Predictive methods based on computational modelling could identify the early development of such diseases and, among these techniques, the multiscale modelling approach shows promising potential in view of its capability to describe the musculoskeletal (MSK) system across different spatial and temporal levels. The development of a multiscale model of the MSK system, however, poses great computational challenges and requires the determination of multiscale links such as the joint contact pressure, which is typically predicted by means of computationally expensive methods such as the finite element method. An accurate low cost alternative is represented by the discrete element method (DEM), a computational method in which a spring mattress is used to describe the contact interactions within the joints. The method, however, has been developed for static cases and does not offer the possibility of tracking the physiological motion of the contacting bones over time. Furthermore, time dependent properties such as viscoelasticity are often neglected within these frameworks. This thesis aims at extending the discrete element method (EDEM) to track the bone motion and include the viscoelastic phenomena. The methodology is used, in conjunction with subject specific MSK models, for the development of subject specific ankle models to compute the con-

tact pressure during gait. Evaluation of EDEM and DEM outputs found that not considering the physiological displacement of the talus causes an underestimation of the joint pressure distribution, while the peak values remain substantially unaffected. Comparison against experimental pressure data shows that EDEM can identify the patterns of pressure in cadaveric ankle specimens. Finally, the viscoelastic formulation of EDEM proved successful in describing the typical creep behaviour of articular cartilage.

Contents

Listing of figures

Duolmi un poco questo pié, questo braccio e questa mano.

W. A. Mozart, Don Giovanni, act 2, scene 6

Acknowledgements

Firstly, I would like to express my gratitude to my supervisors, Dr Lingzhong Guo and Prof Damien Lacroix, for giving me the occasion of studying with them and for their invaluable support during the years of my PhD.

I would like to thank Prof Marco Viceconti and Dr Claudia Mazzà for their precious suggestions during the group meetings.

I would like to thank Dr Tassos Natsakis and Dr Ilse Jonkers from KU Leuven who agreed to share with us the experimental data which made Chapter 5 possible.

I want to thanks the Engineering and Physical Sciences Research Council (EPSRC) and the European Commission, which funded this research through the Multisim project (Grant number: EP/K03877X/1) and the MD-PAEDIGREE project (FP7-ICT Programme, Project ID: 600932) respectively.

Thanks to all my INSIGNEO friends, particularly my best PhD friend Sara, my chess mate Alessandro and Giuliano The Bomber, for all the time we spent together drinking beer, coffee... and sometimes even talking of science!

My biggest thanks go to Erica and to my family for the continuous support throughout my studies.

1 Introduction

1.1 Motivation

The human musculoskeletal system is a complex system of organs which, thanks to the close cooperation of bones, muscles and connective tissue, gives humans the ability to move. It provides form, support, stability and movement to the body. Despite its extreme resilience, events can happen during life which trigger the onset of diseases which limit the functions of the musculoskeletal system, causing pain, discomfort and in some cases even reduced mobility to the affected people.

Bone fractures and osteoarthritis (OA) are two among the most common diseases which can greatly affect the musculoskeletal system. Bone fractures can occur either following traumatic events, such as falls [203], or because of natural processes which weaken the bones, such as osteoporosis [55, 191]. In the former case the bones are not strong enough to resist to the force generated during

falling [192], while in the latter case they cannot resist the forces which muscles exert on the bone during walking [154].

Osteoarthritis is a degenerative joint disease which causes breakdown of all the joint structures, including the articular cartilage and both subchondral and trabecular bone [89], leading to joint pain [160], stiffness [60] and reduction of the range of joint motion [12, 158]. Its etiology is still debated and uniform consensus is yet to be reached. It is believed, however, that traumas [205, 235] and biomechanical factors such as excessive joint loading [52, 73] can trigger the onset of the disease. Even though the joints most susceptible to OA are the hip, knee and shoulder [104], it is reported than 1% of the world population suffers from ankle OA as well [188].

In addition to the pain and discomfort caused to single individuals, these pathologies represent also a significant burden on the healthcare system. The annual incidence of hip fractures in the UK, 79 000 cases [105], is estimated to cost the NHS approximately £1.1 billion [138]. Because of the increasingly ageing population this number is expected to grow in the future, also considering that older age groups are more susceptible to osteoporosis related hip fractures [72].

Recent estimates suggest that approximately 54 million adults in the US [107] and 8.5 million in the UK [76] show symptoms related to OA. The incidence is related to age: 7.1% of adults aged 18 to 44 and 29% of subjects between 45 and 65 years show signs of OA in at lest one joint. The prevalence grows to 49.6% when considering individuals older than 65 years [18]. These percentages are expected to increase in view of the again population [107]. OA related costs in the UK are estimated at £3.2 billions [40].

Whereas for bone fracture the treatment consists essentially of immobilisation of the affected region [216, 243], existing therapies for OA involve management of the symptoms [48, 157] and the administration of pain killers[16]. Most severe cases are treated with total joint replacement surgery [235], which represents a significant burden on the healthcare system. The cost of over 400 000 total knee replacement surgeries performed every year in the US is estimated to $10 billions [128].

Adopted treatment strategies have been developed in the course of the years

after analysing the outcomes from large cohorts of subject and selecting the ones which had the better results in the majority of cases [4]. This approach has undeniably led to important progresses, although the very evident fact that each human being is unique was rarely if never taking into consideration. Also, *ex-post* strategies do not offer prevention against the arise of a disease.

Predictive methods can identify the features of a disease before it completely develops, giving the doctors greater possibilities to successfully tackle the problem. Image-based predictive methods are diffused in the clinical practice. In recent years the research community has started to apply mathematical modelling to clinical problems. The development of a mathematical model requires first to identify a certain phenomenon, and then to use mathematical equations to correctly describe it and, possibly, identify its causes [238, 240]. Because of the important role that mechanical stimuli play in the onset and development of OA and bone fractures, the determination of the mechanical environment within the musculoskeletal system is fundamental. Forces in the body can be estimated by using simple engineering principles [254]. Recently, the multiscale modelling approach has gained popularity among researchers of the musculoskeletal system in view of its capability to model different sub-parts of the musculoskeletal system and at the same time to describe their mutual interactions [24, 238]. As shown in Figure 1.1.1, within the context of modelling of the musculoskeletal systems one can identify the following scales: environment, population, body, organ, tissue, cell and molecule.

The population level is comprised of several individuals which, even though they may vary for gender or ethnic origin, share some common features. The human motion is described at the body level, where the human body is modelled as composed merely of bones and muscle [238]. Muscle forces and joint load are computed at this scale. The organ level is responsible for the description of the mechanical response of the bones when subject to external load [238]. At the tissue level the bone remodelling unit is modelled: it is responsible for bone apposition and resorption [238]. The cells forming the bone tissue are described at

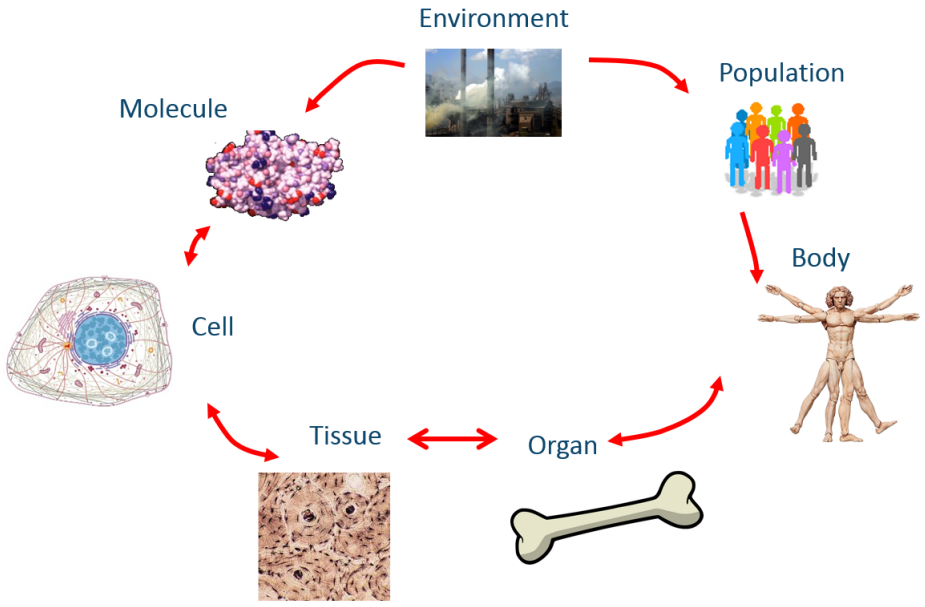

Figure 1.1.1: Hierarchy and connections of the scales.

the cell level [238], which characterise the material properties of the tissue [238]. Figure 1.1.2 shows a diagram of scale separation with the characteristic time and space lengths of each scale. The full integration of all the scales of musculoskeletal system shows promising potential for application to clinical problems such as the prediction of the risk of hip fracture [240].

However, developing such a multiscale model of musculoskeletal system poses many great challenges and one of them is that the simultaneous numerical treatment of equations spanning several order of magnitudes in time and space is currently beyond the available computational capacity. It also requires the definition of multiscale links which carry information across the scale. In the context of study of osteoporosis and osteoarthritis we will focus on the body and organ level which, as Figure 1.1.3 shows, can be connected by means of the joint contact pressure. The bones (organ level) which articulate to form the joints are covered, at their extremities, by a layer of articular cartilage. Forces generated during movement activities (body level) press the bones one against each other, causing the layer of cartilage

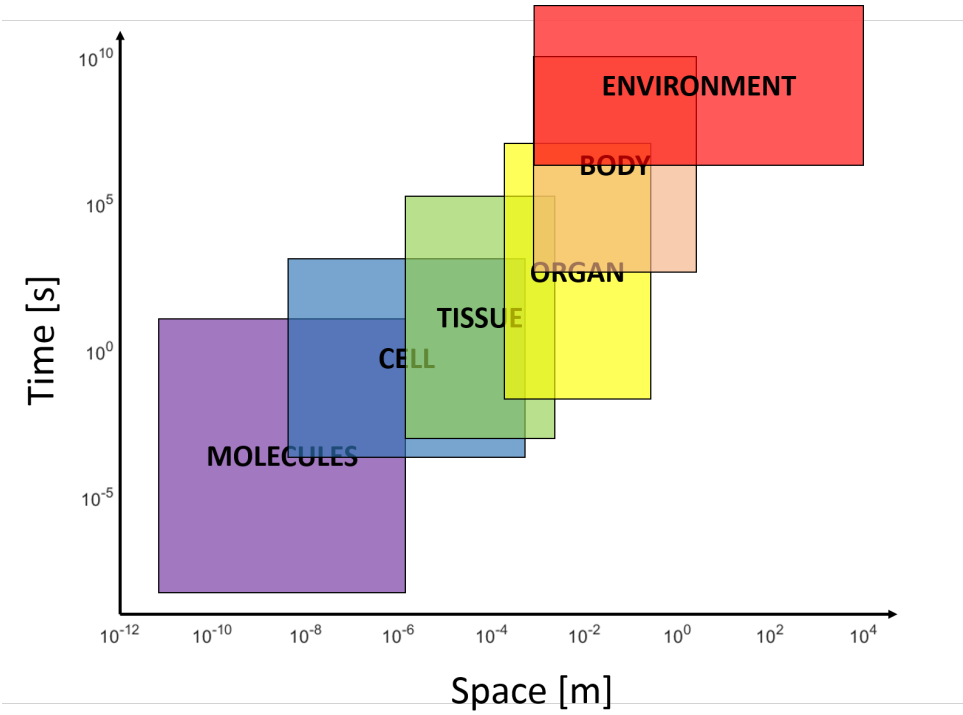

Figure 1.1.2: Scale separation in multiscale musculoskeletal biomechanics.

to make contact. It is the contact pressure generated between the cartilage layers that transmits the external load to the bones which then respond according to their mechanical properties. Since modifications of the structure of the cartilage affect the load transmission within the joint it is clear that the joint contact pressure acts as a multiscale link between the two scales.

This project will focus on developing a computationally efficient modelling and simulation methodology to build a link between body and organ. This study is an indispensable part of multiscale modelling of musculoskeletal system, which will provide quantitative knowledge related to the risk of fracture and better understanding of the mechanical factors contributing to articular stress induced by joint motion.

The estimation of joint contact pressure, originally performed through analyti-

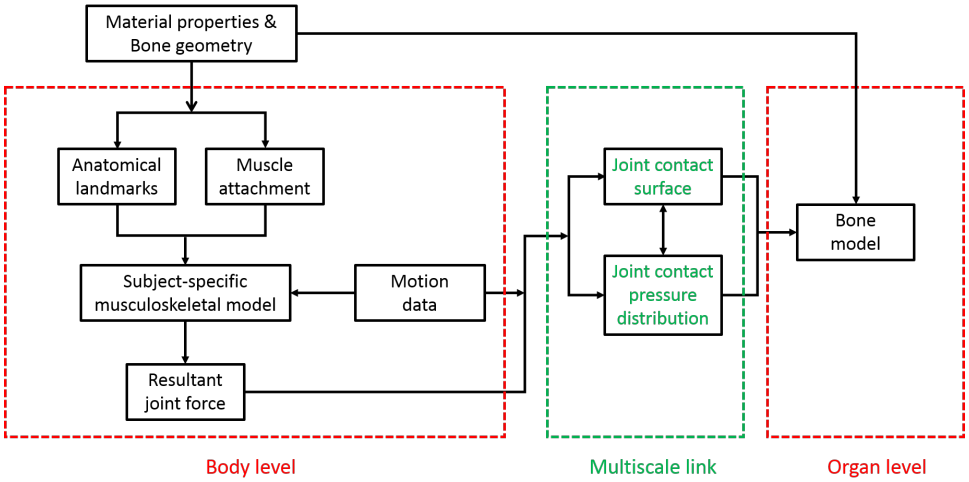

Figure 1.1.3: Coupling between body and organ levels

cal techniques on simplified geometries [25, 90, 113, 116], has received great impetus from the advance in medical imaging and the increase in available computational power which allowed the simulation of increasingly complex scenarios. At the same time researchers acknowledged that each individual is different and, thanks to technological advances, were able to develop the first subject specific models of the human joints [123, 228, 239, 250]. Today, most of the available subject specific joint models focused either on the hip [8, 69, 97, 118, 195] or the knee [37, 125, 135] joints. Such models involved descriptions of the bone and cartilage geometries built from medical images, and were written in terms of partial differential equations (PDE), typically solved using the finite element (FE) method.

However, despite the availability of powerful computing machines, the development of subject specific FE models of the joints remains a time consuming task, both in the pre-processing and the computation phases [1, 122]. Furthermore, the coupling between body and organ levels requires the simultaneous solutions of the PDEs describing the deformation of the cartilage and of the equations describing the motion of the body. The solution of a PDE is usually found through a series of intermediate steps, which have to be performed multiple times if the equation

is coupled with body level equations, making the solution of the coupled problem more challenging.

Even restricting the reasoning to the investigation of contact patterns in the joints, it is clear that costly simulations restrict the applicability of subject specific modelling techniques to small cohorts and datasets , whereas fast but still accurate computational methods could be of use for preliminary evaluation of the state of the joints in subject specific scenarios, or for population-wide investigation [9]. In a possible scenario fast methods are used to compute the contact pressure distribution, which is then passed as boundary conditions for FE simulations, making possible to avoid costly FE contact simulations. The reduced computational cost would enhance the coupling between the scales, and make possible to run such analyses in shorter time [1] and on population-wide datasets [9].

An example of such fast methods is the discrete element method (DEM), a fast and reliable technique primarily used for static contact modelling in the human joints [1, 122]. It considers the bones as rigid bodies, interconnected by a mattress of springs which models the articular cartilage. These modelling assumptions drastically reduces the number of degrees of freedom of the system and lead to a description of the problem by means of ordinary differential equations, whose solution is significantly less computationally expensive.

1.2 Scope of the work and summary of chapters

This work is devoted to the application of DEM, and of a time dependent extension we developed, to the subject specific modelling of the ankle joint.

This thesis is organized as follows.

Chapter 2 presents the relevant literature, discussing the anatomy of the ankle joint and its components. In addition, details on the techniques for the analysis of the human motion and the development of musculoskeletal models are also given. After a review of the existing joint models the aims and objectives are stated.

Chapter 3 presents the mathematical theory behind the discrete element method (DEM), exposes its limitation and presents the extended discrete element method

(EDEM).

In Chapter 4 the details of the development of subject specific ankle joint models are presented. Outputs from DEM and EDEM are compared on simplified and subject specific geometries in static and dynamic situations.

In Chapter 5 the predictions of EDEM in terms of contact pressure are compared against experimental data collected at KU Leuven, Belgium.

Chapter 6 extends EDEM to viscoelastic systems, and presents a simple application.

Chapter 7 draws the conclusions of the study, exposes the limitations and future directions, and highlights the contributions of the thesis.

2

Literature review

As discussed in Chapter 1, osteoarthritis and osteoporosis represent a common disorder of the human musculoskeletal system. It is estimated that 1% of the world population suffers from osteoarthritis related pathologies at the ankle joint [188]. Mathematical modelling can be used with the purpose of preventing the onset of such disorders, or at the very least to understanding their causes. Among the possible choices for modelling the human musculoskeletal system, the multiscale approach shows great potential. It has been shown that the musculoskeletal system can be subdivided in different levels, or scales, and that the body and organ ones are the more relevant to the determination of the mechanical environment within the joints. The joint forces are computed at the body level using multibody dynamics and optimisation techniques, commonly grouped under the name musculoskeletal modelling, and then transferred to the organ level by means of the joint contact pressure, which acts as a multiscale link.

The aim of this chapter is to present a literature review on musculoskeletal modelling and joint contact mechanics. Firstly, the anatomy of the foot and its components, including bones, muscles, ligaments and articular cartilage is introduced. The main features of the human gait cycle are then explained, followed by a review of the techniques commonly used in the analysis of the human motion. Results from experimental and computational studies of the contact mechanics of the ankle joint precede the statement of the aims and objectives of the work.

2.1 Foreword

To study human movement and musculoskeletal systems, the definition of a terminology to indicate the different parts of the body is essential. To this end three planes are defined which divide the human body into sections. Figure 2.1.1 shows the anatomical planes of the human body.

The sagittal plane divides the body into a right and a left parts. The frontal, or coronal plane, identifies an anterior and a posterior part. The transverse plane is orthogonal to the sagittal and coronal. The three planes have in common one point, which is the centre of mass of the human body.

2.2 Ankle joint structure and function

The ankle joint complex is comprised of the lower leg and foot forming the kinetic linkage between them which allows the lower limb to interact with the ground, a key requirement for human locomotion. This section will highlight key anatomical bony structures and soft tissue that form the ankle joint complex.

2.2.1 Anatomy of the ankle joint

The human foot is a complex system, whose global behaviour is determined by the coordinated action of different parts: bones, capsules, tendons, muscles, synovial fluid and articular cartilage [248] are just a few of the components. It is usually

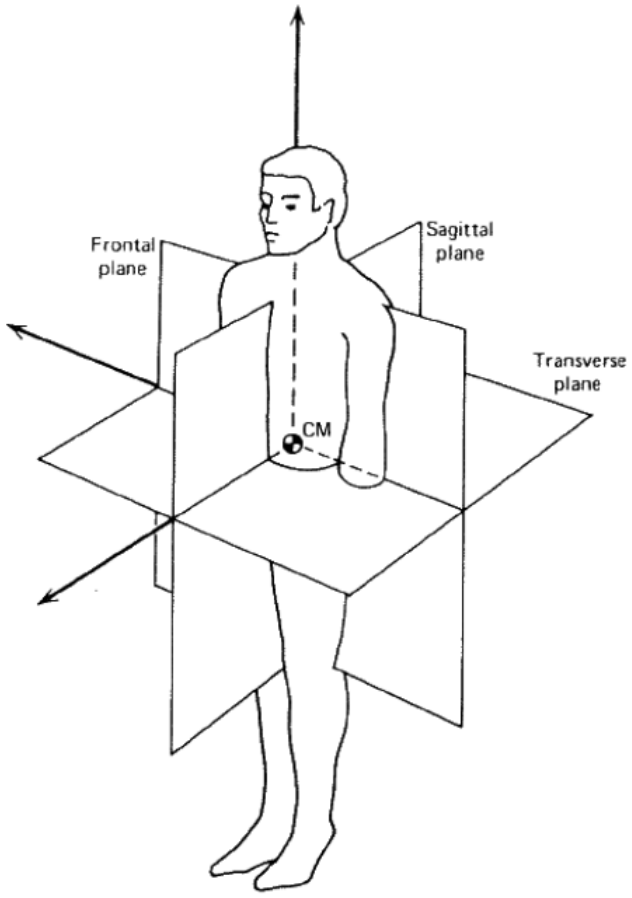

Figure 2.1.1: Anatomical planes of the human body. Figure adapted from [251].

subdivided into three segments: the hindfoot, the midfoot and the forefoot [83] and consists of 26 bones associated with 33 joints [29]. Five bones and three joints constitute what it is commonly referred to as ankle joint. These joints are the subtalar joint, the transverse tarsal joint and the tibiotalar joint, formed by the junction of talus and calcaneus, talus and navicular, talus and tibia respectively.

The subtalar joint is formed by the articulation of the inferior part of the talus with the anterior portion of the calcaneus, and provides attachment for the Achilles tendon. The two bones articulate in two regions , on the anterior and posterior

parts of the calcaneus, respectively, through a stable concave-convex connections. Besides, further stability is provided by a number of ligaments.

The transverse tarsal joint, also known as Chopart's joint, is formed at the junction between the talus and navicular. Studies from functional anatomy revealed that its axis of motion is the same as the subtalar axis [159].

The main load bearing joint in the ankle complex is the tibiotalar joint, formed at the junction of the distal end of the tibia and fibula with the superior part of the talus. The distal end of the tibia presents, on its medial compartment, a process named medial malleolus. The distal end of the fibula, located on the lateral side of the joint, forms the lateral malleolus. In between the two malleoli there is the tibial plafond, which is the inferior part of the distal end of the tibia. These three constitute the articular joint with the talus. The talus presents a head, a neck and a body. The talar dome, the superior aspect of the body, is the part which ultimately articulates with tibia and fibula. Figure 2.2.1 shows the distal tibia and the talus.

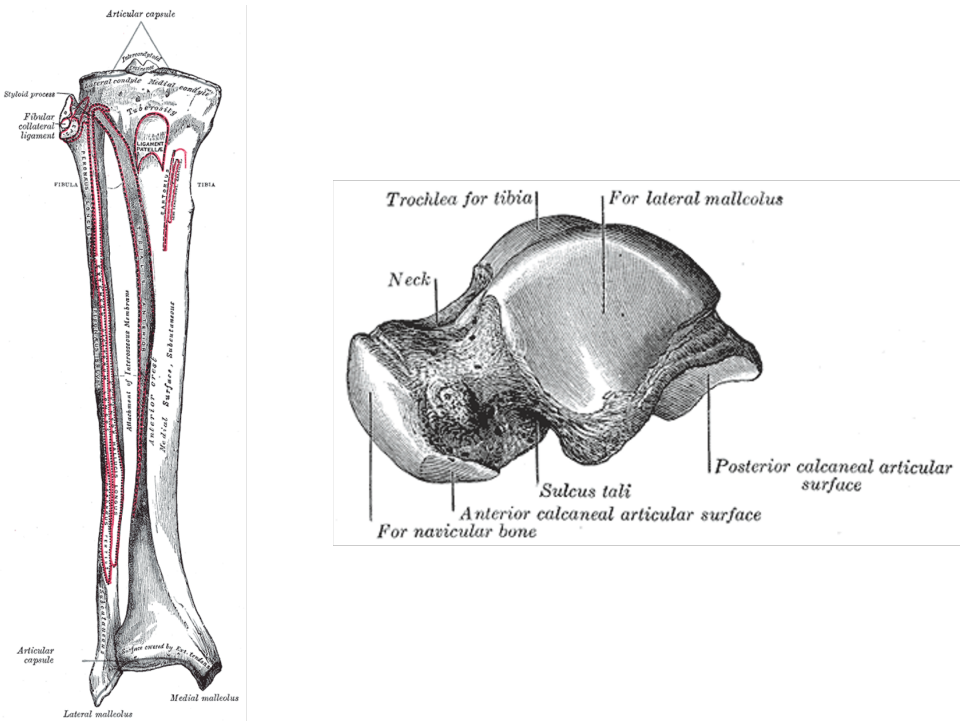

Figure 2.2.1: Right tibia (left) and talus (right). Figure from [248].

Seen in its lateral profile the talar dome has the aspect of a circle and, as illustrated in Figure 2.2.2, the whole talar dome can be approximated with a cylinder [19]. Physiological measures of the radius are approximately 20 mm [99].

As shown in Figure 2.2.3, several ligaments span the ankle complex providing connection between the bones and stability during the movement. Talus and fibula are connected at the anterior side by the anterior talofibular ligament and at the posterior side by the posterior talofibular ligament. Anterior and posterior tibiotalar ligaments join the talus and tibia. Tibia, talus and calcaneus are further connected by branches of the deltoid ligament.

The ability of the foot to perform a large variety of complex movements is guaranteed, in addition to the highly specialised bone geometry, by twelve extrinsic muscles [29]. These muscles can be grouped into compartments according to their

Figure 2.2.2: Lateral view of the ankle joint. Figure from [159].

function. A possible classification distinguishes between anterior (tibialis anterior, extensor digitorum longus, extensor hallucis longus, peroneus tertius), posterior (gastrocnemius, soleus, plantaris), lateral (peroneus longus, preoneus brevis) and deep (tibialis posterior, flexor digitorum longus, flexor hallucis longus) compartments [194] but different ways of grouping are possible [173].

2.2.2 Articular cartilage

The extremities of the articulating bones are covered by layer of articular cartilage, which provides lubrication and smooth transmission of the loads generated during living activities [77, 104]. It is avascular and aneural [46, 178], and owes its remarkable mechanical properties to its internal composition. It is considered as a porous composite material [168] composed of cells, *chondrocytes* and their precursors *chondroblasts*, and a solid matrix, called *extracellular matrix*, which is mostly

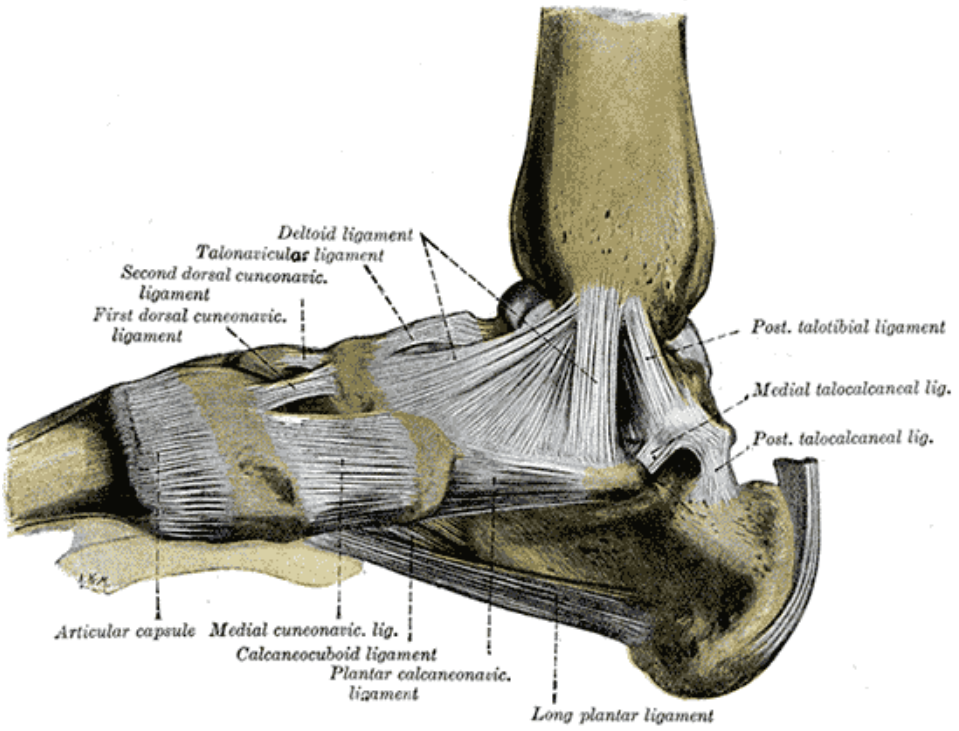

Figure 2.2.3: Ligaments of the foot. Figure from [248].

formed of water, type 2 collagen fibres and various proteins.

Articular cartilage exhibits a layered structure which can be subdivided into four main zones: superficial tangential zone, middle zone, deep zone and calcified zone [165]. The separation between these zones is not neat, as they are distinguished according to the predominant orientation of the collagen fibres. As shown in Figure 2.2.4, the fibers are parallel to the surface in the superficial zone, and rotate in the middle zone until reaching an orientation orthogonal to the bone surface in the deep zone [190].

Chondrocytes, which represent just a small portion of cartilage's volume, are the living heart of the tissue. During their lifetime these cells are responsible for constructing and deconstructing the surrounding matrix through the synthesis of Type II collagen and proteoglycans. Because of the avascular, aneural and alym-

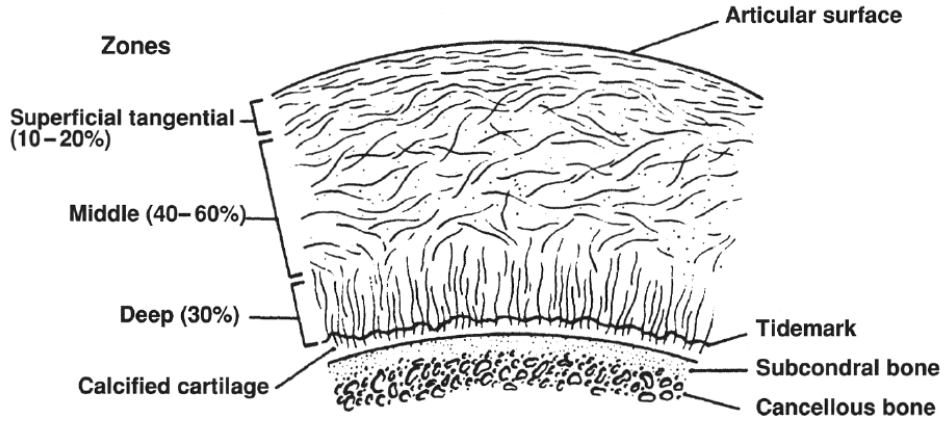

Figure 2.2.4: The layered structure of articular cartilage. Figure from [165]

phatic nature of the cartilage the cells can not be fed directly and must resort to diffusion processes within the extracellular matrix [77, 178]. Wastes are then taken away by the synovial fluid that flows within the matrix.

The mechanical behaviour of the articular cartilage under loading arises from its complex structure. The tissue can be thought as composed of two phases: a fluid phase and a solid phase. As said above, water constitutes roughly 80% of its wet weight. The sudden application of a compressive load such as those generated during gait causes an immediate increase of the interstitial fluid pressure, which pushes the fluid out of the extracellular matrix. Because of the low permeability of the matrix, however, large frictional drag forces are generated which oppose to a quick exudation of the fluid [167–169]. The release of the load allows the fluid to flow back into the tissue. These dissipative processes confer the cartilage two different viscoelastic properties. It is possible to identify both flow dependent and flow independent viscoelastic effects. The flow dependent effect is due to the movement of the interstitial fluid and to the frictional forces which are generated when the fluid is moving inside the tissue [13, 168], while the flow independent effect is generated by the motion of the macromolecules which form the collagen fibres of the extracellular matrix [102].

2.3 The human gait cycle

A gait cycle is the time period, the sequence of events, or the movements during human movement in which one foot contacts the ground to when that same foot again contacts the ground. The human gait cycle is divided into two phases [124]: the stance phase and the swing phase. The stance phase occupies around 60% of the gait cycle, while the swing phase comprises the remaining 40%. One gait cycle is normally defined as the period of time between two consecutive events, typically the heel strike of the same foot.

The stance phase begins with the contact between the heel and the ground. The foot then rotates to increase the contact with the ground, leading to the instant of foot flat, at around 15% of the gait cycle and with the ankle typically in dorsiflexion. The foot remains flat until the instant of heel rise, which is then followed by push off. Immediately afterwards, the toe-off concludes the stance phase at about 60% of the gait cycle. During swing the foot is off the ground and undergoes a series of dorsiflexion, plantarflexion, inversion and eversion until it touches the ground again. Figure 2.3.1 schematises the phases of the gait cycle.

2.4 Musculoskeletal modelling of the lower limb

During gait the articular cartilage can be subject to a variety of loads of different magnitude and direction. In the previous sections we have explained the basic deformation mechanism of the cartilage but we did not provide any details on the origin of such loads.

2.4.1 Direct and inverse modelling of the musculoskeletal system

In this section, the musculoskeletal modelling methodologies and the modelling of the ankle joint will be reviewed. The investigation of how joint loads are generated is the main aim of musculoskeletal modelling. Musculoskeletal models typically describe the human body as composed of rigid segments representing different

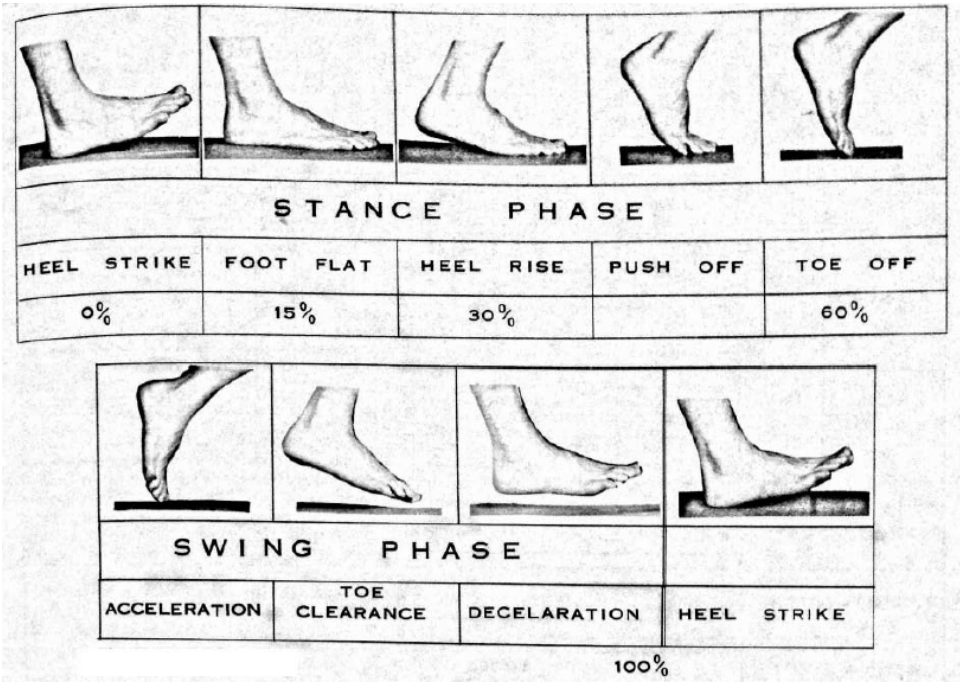

Figure 2.3.1: Subdivision of the gait cycle. Figure from [120].

parts of the body, interconnected by joints with various properties and put in motion by actuators, i.e. muscles. Two approaches are possible: direct and inverse. Direct methods compute the body kinematics resulted from a set of muscle activation patterns through direct integration of the equation of motion [238]. The knowledge of the muscle activation pattern is a delicate issue: surface electromyography (EMG) can provide an estimate, but they fail with deep muscle and suffer from noise [44]. Also, numerical instability when integrating the equations of motion can be common [175].

Inverse approaches, instead, start from the observation of the kinematics to compute the muscle activation pattern responsible for the generation of the observed movement [254]. A typical pipeline of the inverse approach, is depicted in Figure 2.4.1. The first stage is the data collection, followed by inverse kinematics, inverse dynamics, static optimisation and joint reaction analysis. In what follows we

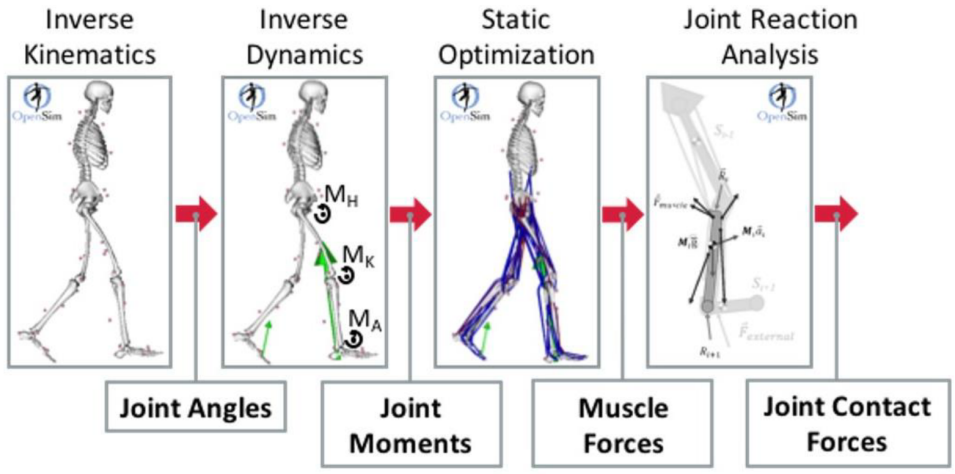

Figure 2.4.1: Typical pipeline of inverse methods in musculoskeletal modelling.

will discuss each of these stages.

During data collection the input data, which can be categorised into anatomical, kinematic and kinetic data, are collected. Anatomical data are used to assign each segment its length, mass, centre of mass and tensor of inertia. Rough estimates can be obtained from regression equations [54, 183], or statistical analysis of data from cadavers [39]. These values, useful for the generation of so-called "generic" musculoskeletal models [36, 58, 162] are of little use when conducting subject specific investigations. Subject specific data are typically collected using medical imaging techniques such as magnetic resonance imaging (MRI) [163] or computed tomography (CT) [152]. The images are then segmented [223] and used, through mapping of the grey level of the voxels into the density of the tissues [65, 66], to estimate inertial properties such as mass, centre of mass and moments of inertia. Kinematics data are gathered through flashing LEDs [54, 153] or reflective markers [103, 163] attached to the skin of the subject during a motion. Their trajectories are recorded using photographic cameras [54], infrared cameras [103] or optoelectric systems [255].

During the inverse kinematics modelling stage the recorded trajectories are used, in conjunction with the chosen joint definition, to compute the joint angles. It is

common to model the hip as a ball and socket joint, and knee and ankle as ideal hinges. The trajectories of the experimental markers are first imported into a software for musculoskeletal modelling, and then a set of virtual markers is defined. At each time frame a least square minimisation algorithm is used to place the virtual markers in a position as close as possible to the measured ones, at the same time guaranteeing that the segments move coherently with the adopted joint representation [59]. The choice of the locations of the experimental markers is crucial as it can affect the estimation of the joint angles, especially when multi-segments foot models are adopted [182]. Ground reaction force, which is the force that the body exerts on the ground while making contact with it during walking and, because of Newton's third law [177], is also the force that the ground exerts on the body, is recorded using force platforms or insole pressure sensors [50, 117].

The inverse kinematics stage allows to position the rigid segments in space and to orient them relatively to each other accordingly to the measured kinematics. By taking the time derivatives of the position the velocity and acceleration of the segments can be computed, leading to a full knowledge of the kinematic state of the system. The aim of the inverse dynamics stage is to compute the internal joint contact forces and moments which are exchanged among the segments during the dynamic activity[184]. To this end the original link-segment model is broken into its elementary parts, which are then examined separately and solved sequentially from the ankle towards the hip. Together with the joint kinematics, the ground reaction forces served as input for the determination of internal forces and moments. Figure 2.4.2 shows the free body diagram of each segment of the lower limb at a generic time instant during gait.

After inverse dynamics the joint moments responsible for the generation of the observed motion are known. The entities responsible for the generation of the motion are the articular muscles, which contract and exert a force at a given distance from the centre of rotation of the joint. In a musculoskeletal model the number of muscles is typically higher than the number of total degrees of freedom they control, making the determination of the muscle forces an indeterminate prob-

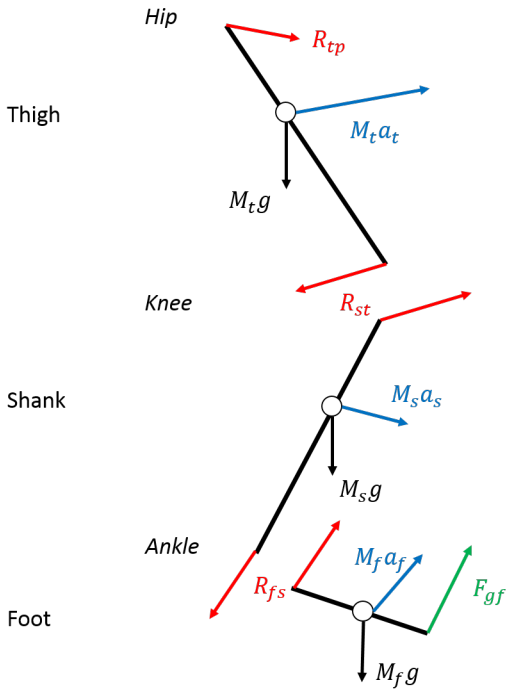

Figure 2.4.2: Free body diagram of the lower limb during walking. Green arrow is the ground reaction force, blue arrows represent the inertia of the rigid segments, black arrow is the gravity. Red arrows represent the unknown joint contact forces.

lem [115]. This means that there exist an infinite number of possible muscle activation patterns which generate the desired joint moments and observed kinematics. Two main methods have been developed to deal with this problem: the reduction method [114, 184] and the optimisation method [54, 210]. In the reduction method, muscles with similar functions are grouped together until the number of unknown forces to be determined matches the number of available degrees of freedom. Optimisation methods were first used in 1973 by Seireg and Arvikar [210]. In this approach, a function of the muscle forces is minimised or maximised, subject to the constraint that the computed activation pattern of the muscle forces generates the observed joint moments. Typically, the sum of squared muscle activation is minimised [47, 87, 163], but formulations where the objective function

involves the sum of the n^{th} powers of the muscles forces [53] or the weighted sum of muscle forces [201, 218] are also used. After the muscle forces have been determined, the total joint load is determined as the sum of the muscle forces and the joint contact force [221, 254].

2.4.2 Kinematics of the ankle joint

The complex anatomical structure of the foot allows for several different movements to be performed. The key movement of the ankle joint complex is the plantar-/dorsiflexion, which happens in the sagittal plane about an inclined axis which passes through the two malleoli. The ab-/adduction motion, also known as internal/external rotation, happens in the transverse plane around the long axis of the tibia. Inversion/eversion, the movement in the frontal plane, are permitted by the subtalar joint [260]. Figure 2.4.3 summarises the elementary motion of the foot.

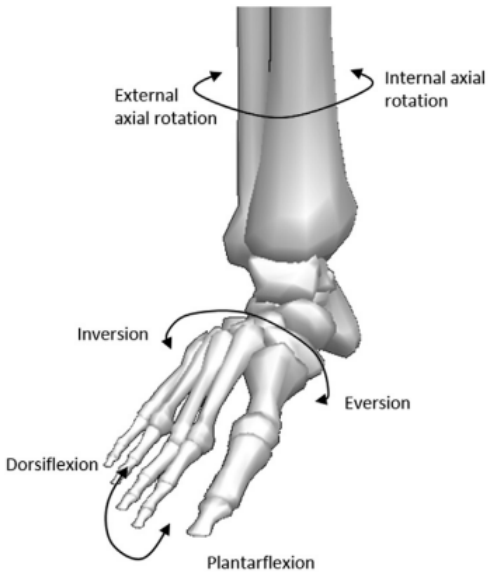

Figure 2.4.3: Axes of rotation of the foot-ankle complex. Figure from [29].

Since the foot and ankle complex are able to perform a variety of different movements, the possible modelling choices are numerous as well. Estimation of the

joint kinematics relies on the collection of marker trajectories, which are then post-processed using an inverse kinematics approach where the experimental trajectories of the markers are matched with the trajectories of virtual markers compatible with the chosen description of the joint.

Single segment foot models represent the simplest idealisation of the geometry of the foot: they consider the foot as a rigid body connected to the tibia through the ankle joint, which can be assigned different degrees of freedom. In [119] Kadaba and colleagues, using a small set of markers, developed a single segment foot model able to capture the motions of ankle rotations and plantar-/dorsiflexion. Few markers were also used in [56] to define a single degree of freedom ankle joint.

Single segment models, although useful for preliminary evaluation of the kinematics of the ankle and foot complex [119], fail to provide a more realistic representation of their structure and kinematics. Multi segments models have proven able to accurately describe the motion of the foot in both healthy and diseased conditions [181]. They are obtained by grouping several neighbouring bones together, creating the so called foot segments. Such segments are interconnected by joints which allow rigid motion between them. Through the use of a two segments model, Scott and colleagues [209] measured *in-vivo* ankle angles ranging from 10° plantarflexion to 10° dorsiflexion.

Several models are based on a three segments foot model plus one segment for the tibia. Kidder et al. [126] subdivided the foot into calcaneus, talus and navicular, cuneiforms, cuboid and metatarsal, and hallux. Observed kinematics in the sagittal plane showed dorsiflexion for the whole duration of the gait cycle, with values ranging from 5° to 25°. Carson and colleagues [38] developed a three segments foot model, comprising of hindfoot (calcaneus and talus), forefoot (five metatarsal) and hallux (hallux proximal phalanx) and investigated the gait patterns in healthy adults, finding angles of plantar-/dorsiflexion ranging from −10° to 5°. Similar ranges of motion were found by Stebbins et al. [220] when applying a similar model to a population of 14 healthy children, and by Okita [181] using frozen cadaveric feet. A similar models, which drew analogue conclusions, was presented in [200]

Despite three segments models succeeded in giving an insight on the kinematics of the ankle-foot complex, more complex and detailed models were also developed to deal with inaccuracies arising from lack of rigid body motion [170, 176] and motion artefacts due to skin and soft tissues [181]. Cobb [45] presented a four segments food model, and Leardini and coworkers showed that their five segment shank-foot model guaranteed high repeatability of the measured kinematics among different subjects [139].

The model developed by Simon [215] included seven segments and showed a kinematics of the tibiotalar joint in good agreement with that from simpler models. In 2003 MacWilliams and coauthor presented a nine segments foot model able to predict the load transmission between the rigid segments, in addition to the usual study of their kinematics [150]. An eight segments model was proposed by Scott and Winter in 1993 [209]: the joints between the segments were described as ideal hinges, and a set of springs and dampers was used to simulate the contact between the foot and the ground.

Although different modelling strategies can lead to different definition of the neutral position of the ankle joint, the amplitude of its range of motion is consistent over the model existing in the literature. During the majority of stance the ankle increases its state of dorsiflexion. The trend reverses towards the instant of heel-off, reaching its most plantarflexed position at toe-off. The ankle angle increases again during half of the swing to then decrease until heel strike. A typical pattern is shown in Figure 2.4.4.

2.4.3 Kinetics

The movement of the body would not be possible without the propulsive action forces and moments. Forces and moments are generated by muscles and then transmitted through the joint. Instrumented prostheses exist for *in-vivo* estimation of the joint load, and they have been used to measure the joint loading at the hip [23] and the knee [61]. Their use however is restricted to a limited number of situation, and researchers have often to rely on musculoskeletal models to obtain

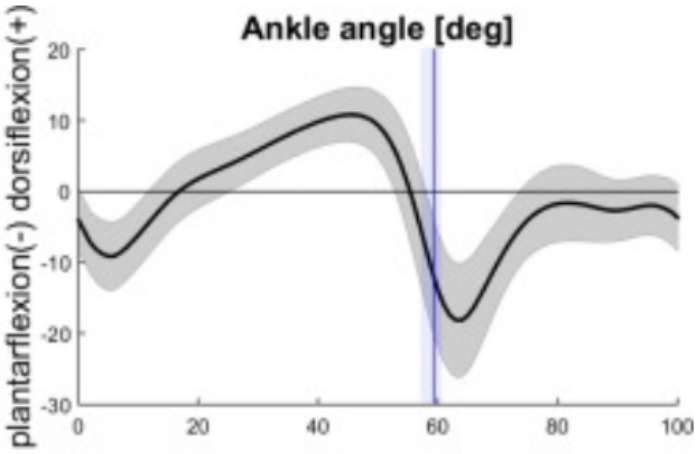

Figure 2.4.4: Ankle angle during gait. The blue vertical line indicates the instant of toe-off. Figure adapted from [163].

an estimation of such loads, especially when investigating the ankle joint.

In 1975 Seireg and Arvikar [211] used generic input data to compute analytically the ankle load acting on a foot modelled as a single rigid segment, obtaining values of peak force around 6 body weights (BW). Similar results have been obtained in [219], with the ankle being subject to 6 BW. The use of penalisation methods led Komistek and colleagues [131] to predict 1.5 BW at the ankle. Recently, several subject specific models of the musculoskeletal system have been proposed, with studies focusing on the investigation of the effect uncertain parameters have on the quantification of the output. Valente et al. [236] predicted the peak ankle reaction force to be 6 BW and relatively insensitive to a number of parameters such as position of bony landmarks and tendon and muscles paths and insertion points. Similarly, Martelli et al. [155] evaluated the maximum force as 4 BW, being affected by 10% from modification of the joint axes. In [193] subject specific lower limbs model of juvenile individuals was presented, with joint forces peaking around 6 BW. The investigation of inter and intra-operator variability in [95] showed that the prediction of muscle forces and ankle contact forces in subject specific lower limbs models can be affected up to 64% and 23% respectively. Maximum reported values of ankle contact pressure ranged from 4 to 8 BW.

Modenese and colleagues [163] developed a series of fully subject specific lower limb models of children to investigate their gait features, obtaining forces from 5 to 8 BW.

A typical ankle joint reaction force is shown in Figure 2.4.5, where it can be observed that the ankle force increases steadily during most of the stance, reaching its peak value in proximity of toe-off and then sharply decreasing afterwards. Residual force is still present during swing, due to the muscles driving the rotation of the foot as the leg swings.

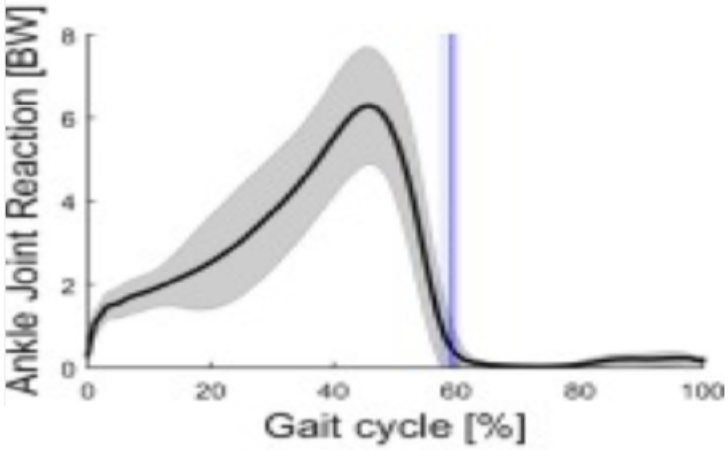

Figure 2.4.5: Ankle reaction forces during gait.

2.5 Ankle contact mechanics

During gait, or physical activities in general, the force generated by the muscles causes the bones forming the joint to be pushed one against the other, causing the interposed layers of articular cartilage to make contact [90]. This field of contact pressure is the multiscale link ultimately responsible for the load transmission within the joints. It is speculated that deviations of the contact pressure distribution from physiological patterns may be related to the onset of degenerative joint diseases such a osteoarthritis [27]. The determination of such patterns, however,

is not feasible in *in-vivo* scenarios, and researchers had to either measure it *in-vitro* or to estimate it *in-silico*.

2.5.1 Experimental studies

Experimental measures are generally performed on cadaveric specimens using pressure sensitive films, placed in between the articular surfaces of talus and tibia, which allow the collection of data regarding contact area and pressure.

In [129], eight cadaveric specimens from adult subjects were placed into a static loading devices which applied loads ranging from 200 N to 1500 N. Recorded values of pressure varied between specimens , but in all cases they were reported to increase with load. Values ranged from 2 MPa to 13 MPa. A similar trend was observed in the contact area, which increased with load from a minimum of 1.5 cm^2 to a maximum of 5.5 cm^2. The maximum loading was observed in the anterior compartment of the joint, and grew towards the medial part as the load increased.

Bruns and Rosenbach [32] investigated a variety of different joint positions before and after ligaments resection in 13 cadaveric ankle joints. The pressure distribution and the location of its maximum were found dependent on the joint position, with the maximum being attained at the centre of the joint when in neutral position and posteriorly when in dorsiflexed position. These observations also held after ligament resection. The obtained values of contact area varied with the position, with average values of 1.6 cm^2. Peak values of contact pressure were around 5 MPa in dorsiflexion and 2.7 MPa in plantarflexion, and increased slightly after ligaments resection. Similar trends were also observed in [64, 133].

Contact area in non-weight bearing conditions in twenty cadaveric feet was investigated in [253]. The specimens were studied under a variety of dorsiflexion and plantarflexion configurations . Cartilage engagement was high, on average above 50%. Contact patterns were dependent on the local cartilage thickness, a result also confirmed in [161]

Hunt and colleagues [110] applied 700 N of axial load on eight amputated feet specimens, finding that the average contact pressure increased from 2 MPa to 5 MPa

when an external rotation is superimposed to the vertical load.

Recently, despite the limitation of long acquisition times which might induce scanning errors, advanced imaging techniques have made it possible to estimate *in vivo* some features of the ankle contact. Wan et al. [244] studied ankle contact area at heel strike, mid-stance and toe-off using a fluoroscopic system which measured the *in-vivo* bone kinematics. The contact area was then computed as the intersection of estimated cartilage volumes. Average values ranged from 2.7 cm^2 at heel strike to 4.16 cm^2 at mid stance. A comparison against experimental data showed that the imaging technique tended to underestimate the contact area. In a following study [245] the fluoroscopic system was used to measure cartilage thickness and strain. The thickness varied with the location in the joint and the maximum strain was observed in the anteromedial part of the joint, where also the thickness was minimum.

Eight specimens from adult subjects were used for a dynamic study in [224], where the stance kinematics and kinetics were simulated by means of a dynamic loading device. Under a 350 N vertical load, 4.8 MPa of peak pressure were measured in the anterolateral section of the joint. Overall, the behaviour of the peak pressure resembled the shape of a typical ankle contact force during stance.

2.5.2 Computational studies

Because of costs, ethical issues, availability of specimens and complex setup, experimental studies of joint contact mechanics have been limited in the variety of scenarios they can reproduce. They are usually performed on specimens collected *ex-vivo* and simulate only a limited range of activities. Moreover, such studies are performed in conditions which are substantially different from the *in-vivo* scenarios they are trying to mimic. The use of devices for the *in-vivo* measurement of the joint contact pressure is limited to the hip joint [106, 132], knee joint [79] and intervertebral discs [252].

Computational models make possible to run a virtually infinite number of simulations of the same phenomenon, varying the input parameters and studying sit-

uations which would be too complex to study experimentally. This is paid with the long time needed to build and run the models. Also, results from *in-silico* can rarely be trusted as they are, and need to pass a stage of comparison against experimental data collected in similar situations.

To develop a computer model it is indispensable to describe the physical phenomenon under investigation using mathematical equations, which are then solved using a variety of techniques. Continuous or discrete modelling philosophies can be adopted. In the former case, the behaviour of the bodies is described by means of the equations of elasticity. These are a system of partial differential equations (PDEs) which describe how the bodies generate an internal stress field which equilibrates the applied loads, accompanied by information on the kinematics of the deformation process and on the relationship between stress and deformation [42, 80]. In the simplest case the deformations, also called strains, are assumed to be small when compared to the characteristic length of the problem, and the stress-strain relationship, also known as constitutive relationship, is taken as linear [92]. It is the constitutive relationship that discriminates whether the behaviour of the body is modelled as isotropic or anisotropic, and homogeneous or heterogeneous. Under these assumptions, the resulting system of PDEs is linear [6, 7, 69, 97]. Contact conditions are usually expressed through inequalities formulated on the contact region whose location, however, is not known *a priori* as its location depends on the solution of the elastic problem [217, 257]. Inequalities and solution dependent conditions are common in nonlinear problems and, indeed, the formulation of a contact problem will always be nonlinear, even when the strongest modelling assumptions are made on the linearity of the mechanical response of the bodies. Adopting more complex constitutive relationships, hyperelastic [30, 189] or multiphasic [136, 185] are common options to model the cartilage, or loosening the hypothesis of small displacements will further increase the degree of nonlinearity of a formulation which was nonlinear from the beginning.

The increasing complexity of the models makes the problems extremely hard if not impossible to solve analytically, and lead to the development of techniques for the numerical treatment of the equations. In most implementations the equations

of contact are usually solved through the finite element method (FEM) [26], a well-established, mature and general technique for solving differential equations. It relies on projecting the solution of a PDE from its original infinite dimensional solution space into a finite dimensional one [196]. This latter space is built on a finite set of basis functions, which in turn are defined over a discretised version of the physical domain under consideration. This projection yields a system of algebraic equations whose solution, under general hypotheses, converges to the solution of the original PDE when the discretisation step converges to zero [88, 196].

The numerical solution of a differential problem, the load transmission within the joint is no exception, can be subdivided into three phases: preprocessing, solution and post-processing [88]. The preprocessing stage is concerned with the discretisation of the physical domain, better known as meshing, and with the choice of the basis of the approximating space, this step is commonly referred to as the choice of the element type. After this, the discrete system of equations is assembled and passed to the solution stage. A variety of algorithms can be used to solve the resulting system of equations, which is typically large and nonlinear [257]. After the solution has been found it can be manipulated in the post-processing phase to extract quantities of interest such as stress and strain, and visualised on the meshed domain.

As FEM is a general and powerful technique, its applications span many fields of biomechanics [28, 74, 81, 98, 108, 208]. Restricting only to joint contact mechanics, several studies exist in the literature, heterogeneous for adopted constitutive models and simulated loading conditions. Most of the studies, however, focus either on the hip [1, 6, 31, 69, 97, 199, 234, 247] or the knee [63, 143]. They typically make use of elastic representation of the cartilage, either linear [1] or hyperelastic [69, 97], which is an appropriate assumption for short loading times [104], but multiphasic representations have also been adopted [91, 144, 185].

Limited literature is available regarding computational ankle contact mechanics. Anderson and colleagues [7] proposed a subject specific FE model of the tibiotalar joint for the prediction of the contact pressure. The articular cartilage

was modelled as a linear elastic isotropic material. The geometry of the cartilage layers was estimated after extrusion from the underlying subchondral bone. A selection of 13 time points from the stance phase were selected and simulated. The talus was weakly constrained, and able to change its orientation when seeking for the equilibrium configuration. Reported values of peak contact pressure were between 9 MPa and 14 MPa.

In 2007 the same authors developed two specimen specific static FE models of two cadaveric ankles, and compared the patterns and values of contact pressure against collected experimental data, finding a good agreement.

Li and colleagues [147] extended the previous studies to predict, in addition to pressure patterns, also the contact stress exposure over time in FE models of 11 intact and fractured ankles. The contact pressure was found higher in the fractured case. Similar results were reported in [9].

Chitsazan and colleagues in 2015 [41] applied compressive loads increasing from 0 N to 1000 N in 70 seconds and then decreasing at the same rate to a cadaveric sample. Five different positions were investigated. The strain of the bones was measured using strain gauges and then compared to prediction from the corresponding FE model, finding high values of correlation. Although the contact pressure was not measured experimentally, the FE model predicted peak values of 4 MPa in the anterolateral region of the joint.

Peak pressure of 6 MPa in plantarflexion and 2.4 MPa in dorsiflexion are predicted by the FE ankle model presented in [3].

Predictions from this powerful tool are paid with time consuming preprocessing phase and resource intensive solution algorithms [137, 257], making FEM not suitable for the integration within a multiscale modelling framework. For this purpose discrete modelling strategies can be used as alternative. Such modelling approach does not consider the bodies as continuous, and gives a simplified representation of the contact interactions [104]. On one hand, this restricts the spectrum of possible scenarios that can be simulated. On the other hand, it can give valuable answers in a short time and, if its field of validity is well delineated, these answers can be as valid as those from continuous models [142]. The discrete ele-

ment method (DEM) is a computational technique developed for the solution of static contact problems, whose fields of application span from the elbow joint [5], to the hip joint [1, 51, 85, 122, 231, 259], the patellofemoral joint [2, 25, 71, 134], the knee joint [22, 25, 207] and the ankle joint [96, 122], which has shown its capacity to produce predictions of joint contact pressure in good agreement with FE results [1, 122, 142] and experimental measurements [2, 71]. Its main assumptions are that the bodies can be considered as rigid, while the interposed layers of cartilage can be regarded as a bed of non-interacting springs.

These assumptions make possible the description of a joint as a low degrees of freedom system, with substantial savings in terms of solution time. The joint contact pressure computed using DEM could then be used as boundary condition for FE simulations of the bones, avoiding the time consuming nonlinear part of the solution. Furthermore, its low computational cost would make DEM ideal for the integration with the multibody systems used at the body level, favouring the development of a multiscale model of the musculoskeletal system. One of the main limitations of DEM, however, is that it has been developed for static problems. When used in time dependent problems every time point is considered independent of the others, which implies that the implicit assumption that the position of the contact bodies does not change over time. However, the use of intra-cortical bonepins [78, 197], skin reflective markers [148] and *in-vivo* imaging [212, 214, 232] have shown that translations happen in the joints during daily activities. The distance of the contacting bones is therefore not constant, and affects the contact pressure distribution [198]. The translations of the bones can be described at the body level by using appropriate joint models [59]. The coupling of such models with the computation of the joint pressure requires a contact method able to include the effects of bone kinematics but the DEM, in its original formulation, is not capable of this. Also, as pointed out in [22], time dependent behaviour such as viscoelasticity cannot be included within DEM without adding additional variables which track the contact status of the cartilage over time.

2.6 Aims and objectives

The development of a time dependent extension of the DEM would make possible to overcome the aforementioned limitations while at the same time preserving the features which makes DEM a powerful fool in view of the development of a multiscale model of the human musculoskeletal system. In this thesis we will develop such an extension, and present its applications to the study of the contact mechanics of the ankle joint.

The aim of this study is the development of reliable and fast to run subject specific ankle joint models able to include time dependent effects during the simulation of the gait cycle using subject specific input data.

Objectives of this study are:

- To implement a static version of DEM.
- To develop a time dependent extension of DEM (EDEM).
- To implement the EDEM in a computationally efficient manner.
- To compare the predictions on idealised and subject specific geometries.
- To compare the outcomes of DEM and EDEM.
- To assess the sensitivity of EDEM to input parameters which may be not well determined.
- To compare the outcomes of EDEM against experimentally collected data.
- To simulate the viscoelastic behaviour of the articular cartilage in simplified scenarios.

3

Discrete modelling in joint contact mechanics

3.1 Introduction

As mentioned in Chapter 2, the finite element method (FEM) is the most used method for the estimation of the joint contact pressure. The mathematical theory behind the FEM involves the use of partial differential equations to describe the mechanical behaviour of the contacting bodies. On one side, this permits a detailed representation of the contact process but, on the other, it requires the use of large computational resources to solve the problem. This led the research community to develop alternative low cost, but still accurate, techniques such as the discrete element method (DEM). DEM is a methodology to treat static contact problems in which the contacting bodies are assumed to be rigid, while the

contact interactions are described by a mattress of non-interacting springs. These modelling assumptions drastically reduce the number of degrees of freedom of the system and lead to a description of the problem by means of ordinary differential equations, whose solution is significantly less computationally expensive. Being developed for static problems, DEM can not be used for the simulation of time dependent contact processes which physiologically happens within the joints of the musculoskeletal system, whereas the use of FEM in time dependent scenarios results even more challenging from a computational point of view. The aim of this chapter is therefore to present an extension of DEM which is suitable for the simulation of time dependent contact processes.

This chapter will begin with a detailed presentation of the mathematical theory behind the Discrete Element Method (DEM), an existing technique for the computation of the pressure between two contacting bodies in static scenarios. The presentation of a simple problem will highlight some of the limitations of DEM and lead to the formulation of the Extended Discrete Element Method (EDEM), a novel technique for the treatment of time dependent contact problems and main theoretical contribution of this thesis.

3.2 The Discrete Element Method

In this section the main hypotheses and features of the DEM, as originally developed in [5], [85] and [241], are discussed. In what follows the method will be described for the case of two contacting rigid bodies only, and without making reference to a specific biomechanical problem. Generalisation to the n-bodies case is straightforward and will not be treated here. DEM is a static method, therefore the discussion in this section will refer to a single time point.

The main hypothesis in DEM is that the contact of two elastic bodies can be modelled using two rigid bodies connected by a mattress of springs. The springs represent the tendency of the two bodies of opposing to the deformation consequent upon the application of an external load. When dealing with contact problems in biomechanics the bones will be modelled as rigid bodies, whereas the ar-

ticular cartilage is represented by a layer of springs. In continuum mechanics the contact state of a point is expressed through inequalities which prescribe the direction of the reaction force a point can exert, and specify that a point in non-adhesive contact experiences a state of compression [217]. These properties are enforced within DEM by giving the springs purely compressive resistance. The external load causes the rigid body to displace from their initial position, and this displacement is then translated to the individual spring which reacts by exerting a force. The force expressed by the spring is related to the contact pressure at that specific point.

Let $\{O; \mathbf{e}_1, \mathbf{e}_2, \mathbf{e}_3\}$ be a Cartesian frame for a three dimensional space. The two contacting bodies will be represented by two disjoint subsets $\mathcal{F}$ and $\mathcal{M}$ of the three dimensional space. We will consider $\mathcal{F}$ to be stationary in space, while $\mathcal{M}$ will be allowed to move to reach the mechanical equilibrium with the external applied loads. The position vector of the centroid G of the moving body, shown in Figure 3.2.1, is expressed in Cartesian coordinates as $\mathbf{r}_G^{\mathrm{T}} = (x_G, y_G, z_G)$. The contact region is estimated through a two stage procedure, one geometrical and one mechanical. The geometrical stage provides the first estimate of the contact region, based on the specific surface shapes of the two contacting bodies, determining its maximal extension, and will be discussed in details in Chapter 4. This maximal extension estimate is then refined during the mechanical stage. Throughout this section we will assume the maximal estimate to be known and describe the mechanical considerations that are drawn for estimating the contact region.

Let $S \subset \mathcal{M}$ denote the maximal contact region. Within the framework of DEM, contact interactions between two bodies $\mathcal{F}$ and $\mathcal{M}$ are modelled by springs, which carry compressive and shear resistance in response to the external loading. The springs are defined to have initial direction normal to S, with one end attached to $S \subset \mathcal{M}$ and the other to $\mathcal{F}$. The un-deformed length of each spring depends on its location on S, and varies according to the shape of the surfaces and the location of the spring. A representative point of S, that is the attachment point of a generic contacting spring, can be denoted by the vector $\mathbf{r}^{\mathrm{T}} = (x, y, z)$. A complete definition of the springs requires also the definition of their stiffness parameters, which link the deformation of the springs to the force they express when deformed. The

resistance to compressive loads is modelled by the parameter k_d, while the resistance to shear loads is modelled by k_s. This scalar field is not homogeneous over the surface S and varies according to the local length of the springs and to the local material properties of the contacting bodies.

The application of external forces and moments will cause $\mathcal{M}$ to displace, rigidly, from its original position, reaching the equilibrium configuration $\mathcal{B}(\mathcal{M})$. Such displacement can be characterised through two additive components: a translation, common to all the points, and a rotation. The magnitude of the displacement induced by the rotation varies from point to point, according to the distance with respect to the centre of rotation of the rigid body. Using the centroid G as centre of rotation and assuming the rotations to be infinitesimal, the displacement $\mathbf{u_r}$ of a point on the surface S identified by the position vector $\mathbf{r}$ can be expressed as

$$\mathbf{u_r} = \mathbf{u}_G + \mathbf{q} \times (\mathbf{r} - \mathbf{r}_G). \tag{3.1}$$

In Eq. 3.1, the vector $\mathbf{u}_G \in \mathbb{R}^3$ denotes the rigid translation of $\mathcal{M}$, and the vector $\mathbf{q} \in \mathbb{R}^3$ denotes its infinitesimal rigid rotation, as shown in Figure 3.2.1.

To derive the contact equilibrium equation we will here introduce two operators, the *particulariser operator* and the *displacement-to-stress operator*, which will provide clearer physical insight of the method. First, note that for each $\mathbf{v} \in \mathbb{R}^3$ it is possible to find a skew-symmetric matrix $\mathbf{W_v}$ such that, for a given $\mathbf{a} \in \mathbb{R}^3$, one has

$$\mathbf{W_v a} = \mathbf{v} \times \mathbf{a}, \tag{3.2}$$

where "$\times$" denotes the standard vector product in $\mathbb{R}^3$. The meaning of Eq. 3.2 is that the rotation of a vector $\mathbf{a}$ can be characterised either using the skew-symmetric matrix $\mathbf{W_v}$ or its axial vector $\mathbf{v}$. This, however, holds only for infinitesimal rotations.

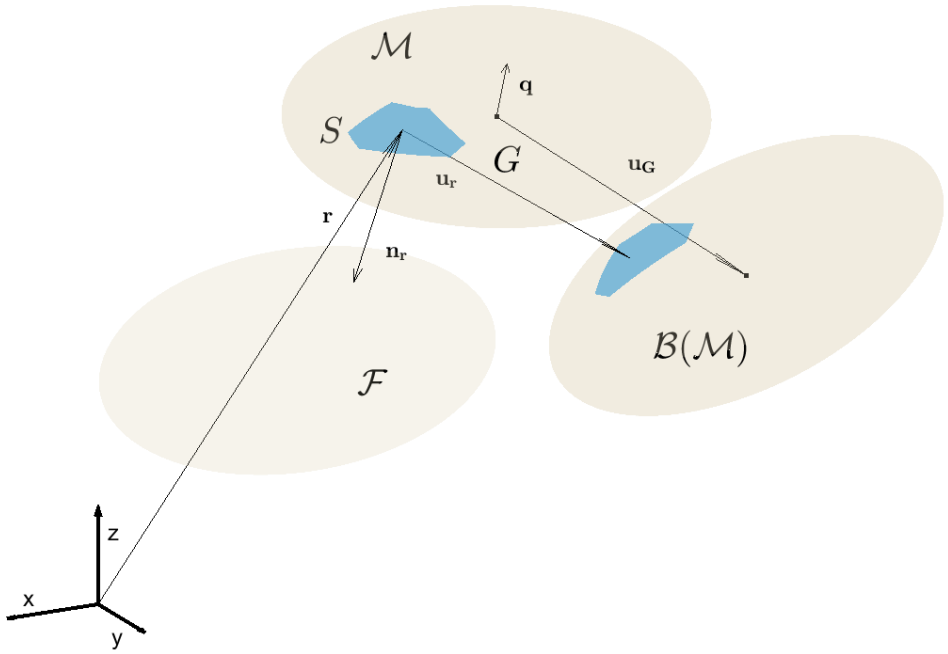

Figure 3.2.1: The kinematics of the discrete element method. The transformation $\mathcal{B}(\mathcal{M})$ which brings $\mathcal{M}$ to its equilibrium position is described by the translation $\mathbf{u}_G$ and the rotation $\mathbf{q}$. S indicates the articular part of body $\mathcal{M}$, $\mathbf{r}$ is a generic point on S, G is the centroid of $\mathcal{M}$ and $\mathcal{F}$ is the fixed body.

If $\mathbf{v} = (l, m, n)$ one has

$$\mathbf{W}_\mathbf{v} = \begin{pmatrix} 0 & -n & m \\ n & 0 & -l \\ -m & l & 0 \end{pmatrix}.$$

Now we define the *particulariser operator* as the following 3×6 matrix

$$\mathbf{B}_\mathbf{r} = \begin{pmatrix} \mathbf{I}_{3\times 3} & \mathbf{W}_{\mathbf{r}_G - \mathbf{r}} \end{pmatrix},$$

where $\mathbf{I}_{3\times 3}$ is the 3×3 identity matrix and $\mathbf{W}_{\mathbf{r}-\mathbf{r}_G}$ is the skew-symmetric matrix associated with the vector $(\mathbf{r} - \mathbf{r}_G)$. $\mathbf{B}_\mathbf{r}$ is called *particulariser* because it links the rigid displacement of the body, which is a global quantity, to the local displacement

of its points and allows to rewrite Eq. 3.1 in a more concise form

$$\mathbf{u_r} = \mathbf{B_r u}. \tag{3.3}$$

The vector $\mathbf{u} = (\mathbf{u}_G^T \, \mathbf{q}^T)^T \in \mathbb{R}^6$ collects the components of the rigid displacement.

To construct the equilibrium equation it is necessary to compute how the springs deform and how, following the deformation, they generate the associated normal and shear forces. Since the body $\mathcal{F}$ is assumed to be fixed, the deformation of the springs is driven by the displacement of $\mathcal{M}$ only. Thus the deformation of the spring located in position $\mathbf{r}$ coincides with its own displacement:

$$\delta_\mathbf{r} = \mathbf{u_r} = \mathbf{B_r u}. \tag{3.4}$$

To determine how the springs carry the applied load it is necessary to define how the deformation is translated into forces. This information is provided by a discrete form of the elastic tensor from the linearised theory of elasticy [92], which we will call *displacement-to-stress operator*. To construct the *displacement-to-stress operator* consider that, given two vectors $\mathbf{a}$, $\mathbf{b}$ in $\mathbb{R}^3$ their dyadic product is defined as the matrix $\mathbf{a} \otimes \mathbf{b}$ such that

$$(\mathbf{a} \otimes \mathbf{b})\mathbf{c} = (\mathbf{b} \cdot \mathbf{c})\mathbf{a}, \quad \forall \mathbf{c} \in \mathbb{R}^3. \tag{3.5}$$

The application of $(\mathbf{a} \otimes \mathbf{b})$ results in a vector parallel to $\mathbf{a}$, whose magnitude depends on the combined magnitudes of $\mathbf{a}$, $\mathbf{b}$ and $\mathbf{c}$.

Now we introduce a second operator, the *displacement-to-stress operator*, as

$$\mathbf{D_r} = k_d \mathbf{n_r} \otimes \mathbf{n_r} + k_s(\mathbf{I}_{3\times 3} - \mathbf{n_r} \otimes \mathbf{n_r}), \tag{3.6}$$

where $\mathbf{n_r}$ is the unit vector normal to the plane tangent to the contact point $\mathbf{r}$, k_d is the stiffness of the contact in the same direction, and k_s is the stiffness on the tangent plane, due to the friction between the two layers[84]. The normal stiffness k_d

is not homogeneous over the contact domain as it depends on local un-deformed length h and material properties of the springs [1, 85, 96, 122]:

$$k_d = \frac{E(1-\nu)}{(1+\nu)(1-2\nu)}\frac{1}{h} \tag{3.7}$$

Here E and ν are the Young's modulus and Poisson's ratio of the materials which are making contact. The tangent stiffness k_s depends on the local length of the springs and on the shear modulus C as

$$k_s = \frac{C}{h} \tag{3.8}$$

Because of the dyadic products, the action of the *displacement-to-stress operator* is in projecting the displacement of a point into its components over the normal direction and the tangent plane, and then scaling these components according to the stiffness values. The stress in the spring is then computed as

$$\sigma_{\mathbf{r}} = \mathbf{D}_{\mathbf{r}}\delta_{\mathbf{r}} = \mathbf{D}_{\mathbf{r}}\mathbf{B}_{\mathbf{r}}\mathbf{u}. \tag{3.9}$$

Because of the definition of $\mathbf{D}_{\mathbf{r}}$, the stress has one component along the direction normal to S and one on the tangent plane:

$$\begin{aligned} \sigma_{\mathbf{r}_n} &= k_d \mathbf{B}_{\mathbf{r}}\mathbf{u} \cdot \mathbf{n}_{\mathbf{r}} \\ \tau_{\mathbf{r}} &= k_s \sqrt{\|\delta_{\mathbf{r}}\|^2 - \delta_n^2} \end{aligned} \tag{3.10}$$

where $\delta_n = \mathbf{B}_{\mathbf{r}}\mathbf{u} \cdot \mathbf{n}_{\mathbf{r}}$ is the normal component of the strain.

The equilibrium equation can be derived using an energetic approach. To this end first notice that the strain energy density is the scalar product between stress and deformation $\sigma_{\mathbf{r}} \cdot \delta_{\mathbf{r}}$. The strain energy, which is in this case the energy due to the contact, is the integral of the strain energy density over the contact regions. The total energy of the system takes into account also the contribution of the applied

generalised external load $\mathbf{T}$, containing forces and moments, and is therefore

$$\begin{aligned}\mathcal{E}(\mathbf{u};\mathbf{T}) &= \frac{1}{2}\iint_S \sigma_{\mathbf{r}} \cdot \delta_{\mathbf{r}}\, dS - \mathbf{u}\cdot\mathbf{T} \\ &= \frac{1}{2}\iint_S \mathbf{B}_{\mathbf{r}}^{\mathrm{T}}\mathbf{D}_{\mathbf{r}}\mathbf{B}_{\mathbf{r}}\, dS\mathbf{u}\cdot\mathbf{u} - \mathbf{u}\cdot\mathbf{T} \\ &= \frac{1}{2}\mathbf{K}\mathbf{u}\cdot\mathbf{u} - \mathbf{u}\cdot\mathbf{T}.\end{aligned} \tag{3.11}$$

The vector $\mathbf{T} = (\mathbf{F}^{\mathrm{T}}\,\mathbf{M}^{\mathrm{T}})^{\mathrm{T}} \in \mathbb{R}^6$ contains the force $\mathbf{F}$ and moment $\mathbf{M}$ acting on the mobile body $\mathcal{M}$. The matrix

$$\mathbf{K} = \iint_S \mathbf{B}_{\mathbf{r}}^{\mathrm{T}}\mathbf{D}_{\mathbf{r}}\mathbf{B}_{\mathbf{r}}\, dS \tag{3.12}$$

is the stiffness matrix of the system. It is a 6×6 symmetric and positive definite matrix, which encompasses the global geometrical and mechanical properties of the system.

The equilibrium equation is obtained under the condition which minimises the total energy of the system. Imposing that the gradient of the energy is identically zero yields

$$\nabla_{\mathbf{u}}\mathcal{E}(\mathbf{u};\mathbf{T}) = \mathbf{K}\mathbf{u} - \mathbf{T} = 0. \tag{3.13}$$

Eq. 3.13 must be solved for the displacement of the rigid body. The unilateral nature of the contact [217], however, imposes that the solution $\mathbf{u}$ meets the requirement that any of the springs is stretched:

$$\mathbf{D}_{\mathbf{r}}\mathbf{B}_{\mathbf{r}}\mathbf{u}\cdot\mathbf{n}_{\mathbf{r}} \geq 0. \tag{3.14}$$

DEM deals with the constraints by solving Eq. 3.13 iteratively. After $\mathbf{u}$ has been determined, it is checked that all the springs are compressed by verifying the sign of the normal stress $\sigma_{\mathbf{r}_n}$. If a spring is found to be in tension it is removed from the load bearing domain. After this, the matrices are computed again and the equilibrium equation is formulated on the new estimate of the contact region. The proce-

dure continues until the normal stress is non-negative everywhere. The resulting domain represents the active contact region.

3.3 The Extended Discrete Element Method

This section will explain the limitations of DEM, in particular in tracking the relative movement of the contacting bodies over time, and how they can be overcome by modifying its original formulation. This will lead to EDEM, whose details are presented at the end of the section.

Consider the joints of the human body. They are formed by articulating bones, whose extremities are covered by layers of articular cartilage which provide lubrication and smooth transmission of the loads generated during the gait [77, 104]. This process causes the layers of cartilage to come in contact and be compressed one against the other. The resultant field of contact pressure can be estimated through the methodology of DEM with underlying assumptions that the bones are rigid, their role is played by $\mathcal{M}$ and $\mathcal{F}$, and that the contact interactions between the layers of cartilage can be modelled using springs. The length of the springs is estimated according to the distance of the bodies and physiological considerations, as it will be presented in greater details in Chapter 4, and is crucial for the determination of the contact region. The algorithm presented in Section 3.2 applies to problems determined by a single time point. The loads acting in the human joints, however, are not constant and vary in direction and magnitude depending on the activities, such as walking or running, the individual is performing. The articulating bones are continuously displaced from their resting position [197, 212, 214], moving closer or further to each other and modifying their relative distance during the contact process. Since in DEM the estimation of the contact region is based on the estimation of the distance between the contacting bodies, it appears necessary for a more realistic estimation to keep track of the modification of their distance as time progresses. In addition to this, the modelling of complex mechanical properties as the strain dependent stiffness shown by the articular cartilage [146] requires the capability to follow the evolution of cartilage strain over time. We will now

present an example inspired by the load transmission in the human joints, without making reference to any in particular, to explain what are the limitation of DEM in dealing with such situations.

To introduce the problem imagine two elastically deformable bodies in contact. We will call the stationary one $\mathcal{F}$ and the mobile one $\mathcal{M}$. The external load, composed of force $\mathbf{F}$ and moment $\mathbf{M}$, pushes $\mathcal{M}$ against $\mathcal{F}$ and will be denoted as $\mathbf{T}$. For simplicity we will consider the applied moments $\mathbf{M}$ to be zero and the line of action of $\mathbf{F}$ to be fixed. The magnitude of $\mathbf{F}$ varies in time as shown in Figure 3.3.1 and reaches its maximum for $t = t^*$. As long as the applied load is increasing, that is for $t < t^*$, $\mathcal{M}$ is displaced towards $\mathcal{F}$. At the same time, because of the increasing force and reduced distance between the bodies, the contact region enlarges and reaches its maximum extension when the force is maximum. As time goes to $t > t^*$ the force decreases: it is still pushing, although to a minor extent, causing $\mathcal{M}$ to move back towards its resting position. We want to describe this phenomenon and compute the contact pressure using a DEM based approach, neglecting the inertial effects. This will clarify what are the limitations of DEM when dealing with time dependent problems and why an extension is needed.

To this end we will model the two contacting bodies as discussed in Section 3.2, that is two rigid bodies connected by a mattress of springs which model the contact interaction. As the time plays a role in this problem, the applied force will be discretised in a finite number N of time points. When needed, we will make use of a superscript to indicate to position of the bodies at time point t and the load which is acting at that time. With this notation the initial position of the mobile body is $\mathcal{M}^\circ$, and that at a generic time t is identified by $\mathcal{M}^t$. We will not consider in this example the case that $\mathcal{F}$ changes position with time. For example, $\mathcal{F}$ could represent the tibia, which articulates together with the talus to form the tibiotalar joint. During the gait cycle the tibia rotates about the talus of angles known from experimental measures, assuming different orientations over time. Such change of the orientations of $\mathcal{F}$ can be included in the modelling process by imposing the position $\mathcal{F}^t$ as a boundary condition which defines the configuration of the sys-

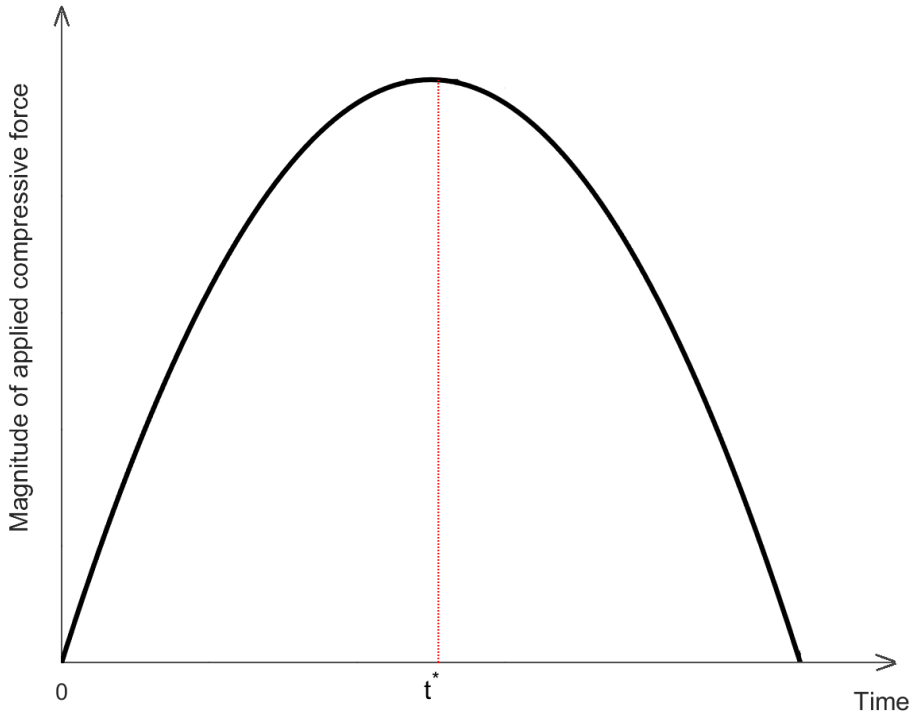

Figure 3.3.1: Time behaviour of the magnitude of the compressive force applied to $\mathcal{F}$. The maximum is reached at $t = t^*$.

tem. The position of $\mathcal{F}^t$ is not modified during the computation of the equilibrium position within a time step, but can change from time to time to reflect the orientation of the joint. The kinematics of $\mathcal{F}$ will be used as input data in Chapter 4. All the following reasoning applies in the same way, with the additional consideration that in that case the contact region depends on the movement of $\mathcal{F}$ through its instaneous position $\mathcal{F}^t$.

A possible approach to compute the contact pressure using the static features of DEM is to solve N independent contact problems, one for each time point. This means that at every time instant t the load $\mathbf{T}^t$ is applied to $\mathcal{M}^\circ$ to compute its equilibrium displacement $\mathbf{u}^t$. Then, although the displacement is used to compute the tensional state of the springs according to Section 3.2, the body is not moved from its position $\mathcal{M}^\circ$, which is used as initial configuration for all the time points.

However, this is not what is happening in reality. As discussed previously, the articulating bones are continuously displaced from their resting position [197, 212, 214], moving close or further to each other modifying their relative distance during the contact process. Therefore, new methods need to be developed to tackle this problem.

A naive solution to this problem is simply to update the position of $\mathcal{M}^t$ at each time instant of computation. More specifically, once $\mathbf{u}^t$ is known at time t, the position of $\mathcal{M}^t$ is updated by applying the rigid displacement to all of its points, producing $\mathcal{M}^{t+1}$ which is then loaded with $\mathbf{T}^{t+1}$ to compute the displacement $\mathbf{u}^{t+1}$ used to obtain the next configuration, and to iterate this procedure until the solution for $t = t^* + 1$ is to be found. What we expect to happen is that $\mathcal{M}^{t^*+1}$ moves back because the force, which is still pushing but less than before, is decreasing. The application of $\mathbf{T}^{t^*+1}$, however, would push the two bodies further closer because the force points towards $\mathcal{F}$. The desired displacement could be obtained if the applied force pointed towards $\mathcal{M}^\circ$, but in that case all the springs would be evaluated as stretched and removed from the load bearing domain, leading to a failure of the algorithm.

The key for solving these issues lies in the observation that when an elastic material is compressed it exerts a force which tries to restore its original configuration. When the system is in equilibrium under a load $\mathbf{T}^t$ it is exerting a force equal and opposite to the applied load. If then a load $\mathbf{T}^{t+1}$ of greater magnitude is applied, the springs, already exerting $\mathbf{T}^t$, will only have to equilibrate the difference $\mathbf{T}^{t+1} - \mathbf{T}^t$. This behaviour can be enforced by modifying Eq. 3.9, the constitutive relationship of the springs, so that they exert at time $t + 1$ the same force they were in equilibrium with at time t, plus an increment of force due to the difference of magnitude at the two consecutive time points. Note that now at $t = t^* + 1$ the system is subject to external force $\mathbf{T}^{t^*+1}$, pushing $\mathcal{M}^{t^*+1}$ towards $\mathcal{F}$, and to the force expressed by the springs, which has a magnitude greater than that of the applied force. The resulting force pushes the two bodies apart. The preexisting compression of the springs gives margin for the decompression due to the decrement of force to happen, without reaching a tensile state. Figure 3.3.2 shows the free body diagrams

for EDEM.

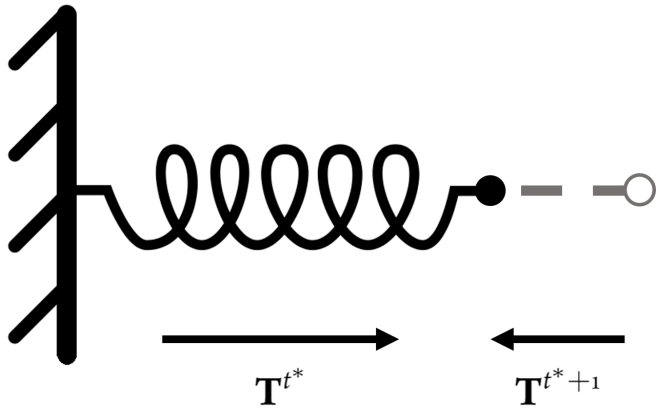

Figure 3.3.2: Free body diagram of EDEM. The force $\mathbf{T}^{t^*}$ pushes the spring towards its rest position, depicted in grey. The force $\mathbf{T}^{t^*+1}$ compresses the spring. Although $\mathbf{T}^{t^*} > \mathbf{T}^{t^*+1}$ causes an release of compression, the pre-existing compression state impedes the overall tension of the spring.

The problem of determining the contact pressure over time is solved by adopting an incremental description, computing the increments of force and displacement with respect to the configuration attained by the system at the previous time point.

This section will present the details on the EDEM. EDEM can be formulated within the DEM framework by using an energetic approach. Although the springs used to model the contact are still purely compressive, their energy density contains an additional term derived from the tensional state at previous time steps, which allows them to reduce their compressive state without being removed from the computational domain.

As the time plays a role in this formulation the variables and operator are time dependent and, as in the previous paragraphs, we will indicate this dependency with a superscript. The details on how the contact problem at time t is solved, and how the algorithm is set for the solution at time $t + 1$ will now be given.

For a given time instant t define the contacting bodies in the three-dimensional

space and, for a point $\mathbf{r}$ in the contact region S^t, the *particulariser operator* $\mathbf{B}_\mathbf{r}^t$ as in Sec. 3.2. This operator allows to relate the generalised displacement $\mathbf{u}^t$ of the rigid body to the deformation $\delta_\mathbf{r}^t = \mathbf{u}_\mathbf{r}^t = \mathbf{B}_\mathbf{r}^t \mathbf{u}^t$ of the corresponding spring at time t. To include the additional term in the strain energy we will extend the *displacement-to-stress operator*. The *push back* force needed to reformulate DEM in an incremental fashion is introduced as the accumulated stress $\sigma_\mathbf{r}^\circ$ and contribute to redefine the stress as

$$\sigma_\mathbf{r}^t = \mathbf{D}_\mathbf{r}^\circ \mathbf{B}_\mathbf{r}^t \mathbf{u}^t = \sigma_\mathbf{r}^\circ + \mathbf{D}_\mathbf{r}^t \mathbf{B}_\mathbf{r}^t \mathbf{u}^t. \tag{3.15}$$

Here $\mathbf{D}_\mathbf{r}^t$ is defined as in standard DEM, but the direction of the normal vectors and the values of the stiffness (Eq. 3.6) are updated as time progresses.

The strain energy of a single spring [241] is defined as

$$\begin{aligned} \varepsilon_\mathbf{r}^t(\mathbf{u}^t) &= \int \sigma_\mathbf{r}^t \cdot \, d\delta_\mathbf{r}^t = \int \mathbf{D}_\mathbf{r}^\circ \mathbf{B}^t \mathbf{u}^t \cdot \, d\mathbf{B}_\mathbf{r}^t \mathbf{u}^t \\ &= \mathbf{B}_\mathbf{r}^{t^T} \sigma^\circ \cdot \mathbf{u}^t + \frac{1}{2} \mathbf{B}_\mathbf{r}^{t^T} \mathbf{D}_\mathbf{r}^t \mathbf{B}_\mathbf{r}^t \mathbf{u}^t \cdot \mathbf{u}^t \end{aligned} \tag{3.16}$$

The total energy of the system is formed of the total energy of deformation, obtained integrating Eq. 3.16 over the contact area S^t, plus the energy of the external load

$$\mathcal{E}^t(\mathbf{u}^t; \mathbf{T}^t) = \iint_{S^t} \varepsilon_\mathbf{r}^t \, dS - \mathbf{u}^t \cdot \mathbf{T}^t = \frac{1}{2} \mathbf{K}^t \mathbf{u}^t \cdot \mathbf{u}^t + \mathbf{p}^t \cdot \mathbf{u}^t - \mathbf{u}^t \cdot \mathbf{T}^t \tag{3.17}$$

The vector $\mathbf{p}^t = \iint_{S^t} \mathbf{B}_\mathbf{r}^{t^T} \sigma_\mathbf{r}^\circ \, dS$ is the total *push-back* force exerted by all the springs in the contact region and contains, directly through the time dependent operator $\mathbf{B}_\mathbf{r}^t$ and indirectly through the vector $\sigma_\mathbf{r}^\circ$, information from all the previous time points. Because of the hypothesis of continuous equilibrium between the spring systems and the external load one has $\mathbf{p}^t = \mathbf{F}^{t-1}$.

As in Section 3.2, the equilibrium equation is derived by imposing that the de-

formed configuration is that of minimum energy:

$$\nabla_{\mathbf{u}}\mathcal{E}^t = \mathbf{K}^t\mathbf{u}^t + \mathbf{p}^t - \mathbf{F}^t = 0. \tag{3.18}$$

After the generalised displacement is computed one can compute the stress in each of the springs in the contact region. Like in DEM, the component of the stress along the normal direction is computed as

$$\sigma^t_{\mathbf{r}_\mathbf{n}} = \sigma^t_{\mathbf{r}} \cdot \mathbf{n}^t = \sigma^\circ_{\mathbf{r}} \cdot \mathbf{n}^t + \mathbf{D}^t_{\mathbf{r}}\mathbf{B}^t_{\mathbf{r}}\mathbf{u}^t \cdot \mathbf{n}^t. \tag{3.19}$$

After the evaluation of their pressure status, the springs which are found to be in tension are removed from the computational domain, the contact region is updated and the equations formulated on the new contact domain. The procedure continues until only compressed springs are left.

Once the displacement $\mathbf{u}_t$ is known one can move the body from its original position to obtain the configuration that will be used as reference for the application of $\mathbf{T}^{t+1}$. The stress $\sigma^t_{\mathbf{r}}$ plays in $t+1$ the same role $\sigma^\circ_{\mathbf{r}}$ had in t. If at a certain time t^* the applied load decreases, $\mathcal{M}^{t^*}$ will be displaced back and the springs will reduce their degree of compression.

The algorithm of EDEM is shown in Figure 3.3.3.

3.4 Discussion

As Eq. 3.19 shows, two terms contribute to the determination of the contact pressure: the second one, $\mathbf{D}^t_{\mathbf{r}}\mathbf{B}^t_{\mathbf{r}}\mathbf{u}^t \cdot \mathbf{n}^t$, is what in traditional DEM is regarded as the only term which determines the pressure in $\mathbf{r}$. Instead EDEM, being an incremental formulation, sees it as a modification of the pressure $\sigma^\circ_{\mathbf{r}}$ already exerted by the spring, which is the first term in Eq. 3.19. If the external applied force is such that the resulting displacement has negative scalar product with the normal vector, then DEM would consider the corresponding spring as in tension and would remove it from further calculations, whereas EDEM would see the increment as negative

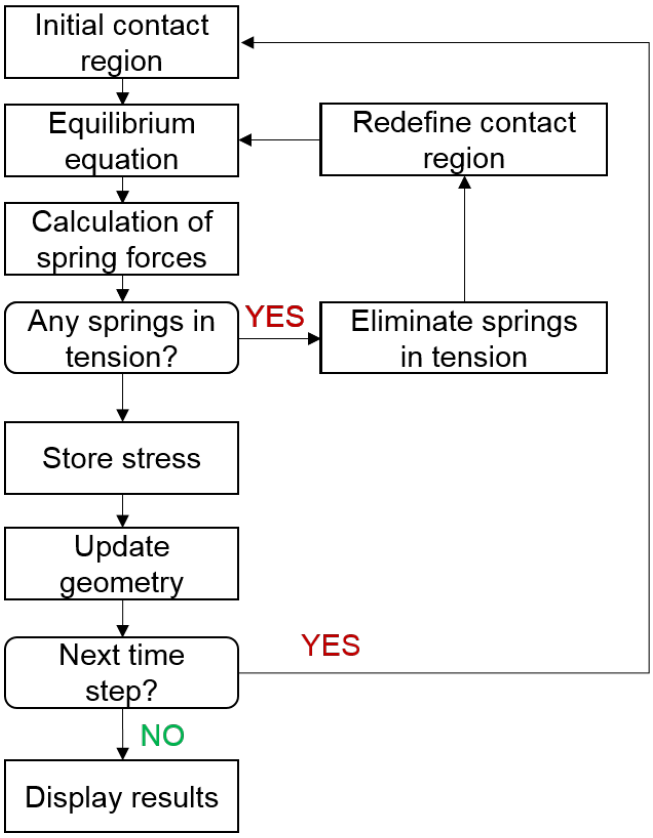

Figure 3.3.3: Algorithm of EDEM.

and, to decide whether the spring is still compressed or not, would compute the sum in Eq. 3.19.

The cooperative action of the pre-existing pressure and its increment allows EDEM to describe the *push-back* effect shown by elastic systems, and at the same time to track the motion of the contacting bodies. As it will be shown in Chapter 4, this has important consequences on the determination of contact patterns. Finally, unlike DEM, EDEM is able to deal with tensile forces if the springs are sufficiently pre-compressed.

It is important to mention that the operators representing the kinematics of the contact, as well as the mechanical response of the material, are to be computed again at each time point. This happens because as the computed displacement is

applied to the system the relative distance of the contacting bodies changes and, as Eq. 3.7 shows, this affects the stiffness of the springs.

It is worth noticing that since time dependency has been introduced, the method can be further extended to include viscoelasticity. This will be the subject of Chapter 6.

3.5 Conclusions

This chapter has presented the main features of the DEM, a computational technique that can be used for the estimation of the joint contact pressure in static scenarios. The modelling technique assumes that it is possible to describe the contact interactions using linear springs, although generalisations to nonlinear springs are possible [241]. As several authors have shown, the main advantage of the method is the short computing time required, together with the high accuracy of the outcomes when compared against results from finite element simulations or experimental studies [1, 122, 231].

The DEM however shows limitations in dealing with time dependent scenarios, and needs to be extended to correctly describe cases of consecutive loading and unloading. We have presented here an extension, termed EDEM, and we have shown that it can handle a larger set of applied external loads than DEM can. This is possible to the introduction of the *push-back* force and the formulation of the contact problem in an incremental fashion. Finally, the EDEM can be extended to model the viscoelastic effect of the articular cartilage.

4

Subject specific modelling of the ankle joint

4.1 Introduction

This chapter will describe in details how the Extended Discrete Element Method (EDEM), introduced in Chapter 3, is implemented and personalised for subject-specific applications. Two applications are presented: first, a static application of DEM on idealised and subject specific geometries; second, a comparison of DEM and EDEM when applied to the prediction of the ankle contact pressure during stance. The experimental data used in this chapter have been collected at the Istituto Giannina Gaslini (Genoa, Italy). The musculoskeletal models used to generate the inputs for the EDEM and DEM simulations have been developed by researchers within the INSIGNEO Institute for *in-silico* medicine (Sheffield, UK).

4.2 Implementation

In this section, the general framework for obtaining the initial contact from ideal and real geometry of the ankle joint and their implementation will be presented.

4.2.1 Personalisation of a model

In the previous chapter we have introduced the theory of the DEM and of its extension, the EDEM . The main underlying hypothesis is that the bones forming the joints can be considered as rigid bodies connected by a layer of springs, which mediate the transfer of loads and model the material behaviour of the articular cartilage. We have mentioned that the contact region is estimated through a twofold procedure based on a first geometrical stage followed by mechanical considerations on the equilibrium and deformation of the springs. We have given the details of the mechanical considerations used to refine the initial estimate. After the application of the external load, the rigid displacement of the contacting bodies and the deformation of the springs are computed: the springs found being in tension are removed from the estimated contact region.

In this section we will describe the procedure for obtaining the initial estimate, and how this contributes to the personalisation of the contact model. Although the algorithm applies identically to both DEM and EDEM, the initial estimate is in general different for the two methods because in EDEM the position of the contacting bodies is updated over time and influences the relative distance of the bodies.

A model is personalised by describing how the pointwise features of the springs, namely their directions and thicknesses, change over the contact domain. They enter the definition of the stiffness (Eq. 3.7) and *displacement-to-stress operator* (Eq. 4.6) and, together with the kinematic information contained in the *particulariser operator*, determine the global stiffness matrix of the system (Eq. 3.12). In

addition to the identification of these features, we need to set rules to discriminate whether a spring is to be considered as representative of a potential contacting point or not. In [49] and [122] two new surfaces were defined, one for each body, extruding every point of the subchondral bone towards its local normal direction: they represent the boundaries of the cartilage layer. The intersection of the extruded surface, and the interposed volume, are regarded as the contact region. The springs placed in the contact region exert a force proportional to the interposed volume.

The approach followed here is based on the definition of one single layer of springs [1]. One of the two bodies is set as reference surface, from which normal vectors are cast and intersected with the target surface. The distance of the bodies along the normal direction is identified with the local length of the spring. In what follows, the details of this procedure for ideal and real geometries will be given.

Let the two bodies $\mathcal{M}$ and $\mathcal{F}$ be defined in the three dimensional Euclidean space, and the basis of the space be $\{\mathbf{e}_1, \mathbf{e}_2, \mathbf{e}_3\}$. As described in Section 3.2 one of them, $\mathcal{M}$, is allowed to move in search of the equilibrium configuration under the externally applied load. This body is also taken as reference for the computation of the local cartilage thickness. We denote the local cartilage thickness as the distance between the two contacting bodies, computed along the vectors normal to the reference body. First, assume that the analytical expression for the external surface of the bodies is know. In this case, they can be described in parametric form [62] as

$$\begin{aligned} \mathbf{f}_{\mathcal{M}} &= x_{\mathcal{M}}(u,v)\mathbf{e}_1 + y_{\mathcal{M}}(u,v)\mathbf{e}_2 + z_{\mathcal{M}}(u,v)\mathbf{e}_3 \\ \mathbf{f}_{\mathcal{F}} &= x_{\mathcal{F}}(u,v)\mathbf{e}_1 + y_{\mathcal{F}}(u,v)\mathbf{e}_2 + z_{\mathcal{F}}(u,v)\mathbf{e}_3 \end{aligned} \tag{4.1}$$

for some parameters u and v. Unit normal vectors to the mobile body are computed as the vector product

$$\mathbf{n}_{\mathcal{F}} = \frac{\mathbf{f}_{\mathcal{M}_u} \times \mathbf{f}_{\mathcal{M}_v}}{\|\mathbf{f}_{\mathcal{M}_u} \times \mathbf{f}_{\mathcal{M}_v}\|}, \tag{4.2}$$

where $\mathbf{f}_{\mathcal{M}_u}$ is a vector on the plane tangent to $\mathcal{M}$ and is defined as

$$\mathbf{f}_{\mathcal{M}_u} = \frac{\partial x_{\mathcal{M}}}{\partial u}(u,v)\mathbf{e}_1 + \frac{\partial y_{\mathcal{M}}}{\partial u}(u,v)\mathbf{e}_2 + \frac{\partial z_{\mathcal{M}}}{\partial u}(u,v)\mathbf{e}_3. \tag{4.3}$$

The same holds, modifying the index, for $\mathbf{f}_{\mathcal{M}_v}$.

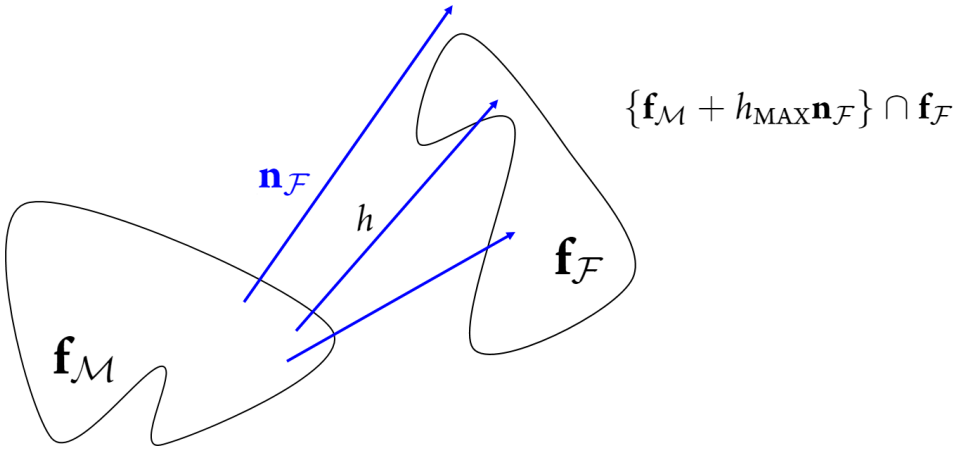

Figure 4.2.1: Estimation of the thickness in the case the analytical equations of the surfaces are known. $\mathbf{f}_{\mathcal{M}}$ represents the fixed body, from which normal the vectors $n_{\mathcal{F}}$ is projected towards $f_{\mathcal{F}}$.

The length of the springs is directly related to the local thickness of the layers of cartilage in the joint. Since in our implementation we condense two layers of cartilage into one layer of springs, the maximum allowed spring length will be double the length of the maximum thickness of the cartilage layer. If the maximum length is denoted by h_{MAX} then $\mathbf{f}_{\mathcal{M}} + h_{\text{MAX}}\mathbf{n}_{\mathcal{F}}$ identifies the surface at the maximum allowed distance from the mobile body. The intersection

$$\{\mathbf{f}_{\mathcal{M}} + h_{\text{MAX}}\mathbf{n}_{\mathcal{F}}\} \cap \mathbf{f}_{\mathcal{F}} \tag{4.4}$$

defines the boundaries of the maximal contact region. It can happen that, because of the geometries and orientation of the bodies, Eq. 4.4 has multiple solutions h for a given normal vector $\mathbf{n}_{\mathcal{F}}$: in this case the solution of minimum length is taken

as the value of cartilage thickness. A sketch of the procedure is depicted in Figure 4.2.1.

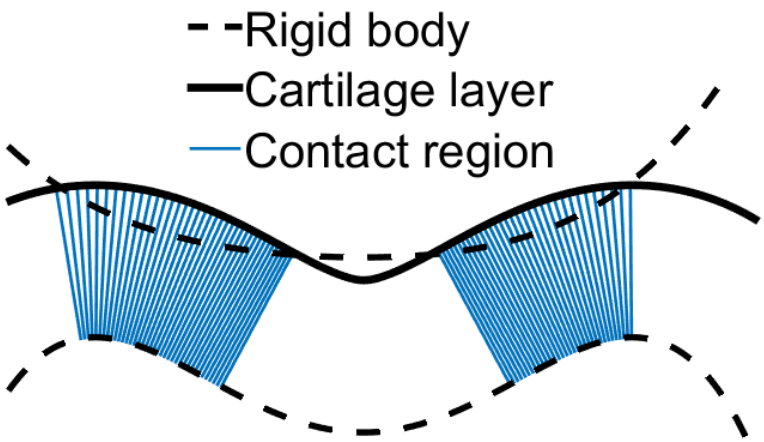

Figure 4.2.2: Contact surface between two articulating bodies. Dashed black line is the surface of the rigid bodies. Solid black line is the cartilage layer. Solid blue line represents the springs whose estimated thickness is below the given threshold, and constitute the maximal contact region.

After the maximal contact region has been defined, the actual length is computed by solving for the values $h(u, v)$ that satisfy the equality

$$\mathbf{f}_{\mathcal{M}}(u, v) + h(u, v)\mathbf{n}_{\mathcal{F}}(u, v) = \mathbf{f}_{\mathcal{F}}(u, v). \tag{4.5}$$

This yields the maximal contact region, also shown in Figure 4.2.2, which is then shrunk during the mechanical stage as explained in Section 3.2 and 3.3.

When dealing with realistic cases, analytical equations describing the bone surfaces are no longer available and numerical techniques have to be used for the computation of the thickness. Yet, the idea of casting normal vectors from a reference surface towards a target one still holds.

The geometries of the bones are generally acquired through imaging techniques such as magnetic resonance imaging (MRI) and computed tomography (CT) [104]. Such medical images contain also soft tissues such as muscles and ligaments and must be segmented to extract the actual bone geometry [86, 163]. Figure 4.2.3 shows the results of the segmentation process from the initial medical images.

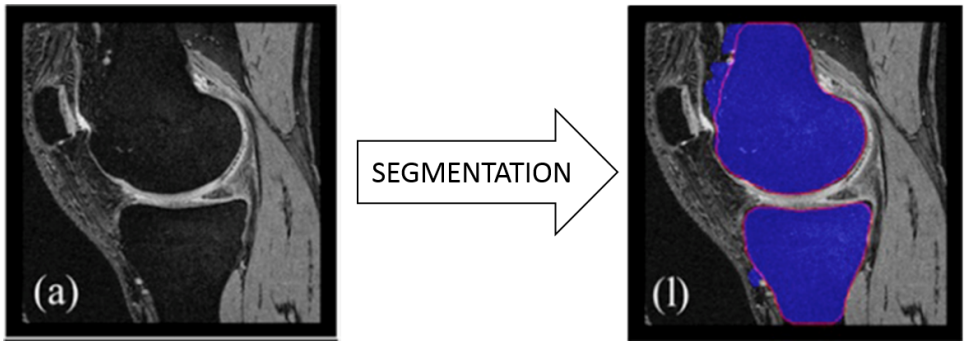

Figure 4.2.3: Segmentation of the bone geometries (right) from medical images (left). Adapted from [82].

After segmentation the geometries are available for meshing, a procedure which provides a discrete approximation of the real geometries. In our implementation both the surfaces are meshed using triangular elements. We estimate the cartilage length using ray casting techniques, in particular the Möller-Trumbore algorithm for ray-triangle intersection [164]. First, the centroid of each triangle of the mobile mesh is computed as the average position of the edges of the triangle. Since the triangle is a planar element it is immediate to compute its outer normal vector through the cross product of two appropriate vectors parallel to two edges. The outer normal, applied to the centroid of the corresponding triangle on the reference body, is then prolonged indefinitely: we will call this object a "ray". The intersection of the ray with all the triangles of the target bodies are then sought. Like in the analytical case, if the shape and the relative position of the target body are such that the intersection is not unique, the intersection with the minimum length is considered to be the length of the spring at that point.

In the numerical implementation we associate two matrices $\mathbf{B}_i$ and $\mathbf{D}_i$ to the

centroid of the i-th triangle of the discretised reference body. Here the subscript i takes the role that $\mathbf{r}$ had in the continuous description. In particular, $\mathbf{B}_i$ contains the coordinate of the centre of rotation of the reference body, which is its centroid and is common to all its points, and the coordinate of the centroid of the i-th triangle. Similarly, the discrete counterpart of Eq. 3.6 is

$$\mathbf{D}_i = k_{d_i}\mathbf{n}_i \otimes \mathbf{n}_i + k_s(\mathbf{I}_{3\times 3} - \mathbf{n}_i \otimes \mathbf{n}_i). \tag{4.6}$$

In Eq. 4.6 $\mathbf{n}_i$ is the outer normal vector to the i-th triangle. Normal and tangential stiffnesses are defined as in Eqs. 3.7 and 3.8.

4.2.2 Dependence of computed thickness on mesh size

The use of geometries from medical images poses the problem of choosing an appropriate mesh size. The mesh size was selected after convergence study, analyzing the variability of certain parameters of interest when the average size of the discretisation is changed [63]. The mesh is considered to be converged when further reduction of the element size has a limited effect on the variation of the parameters. Since in contact problem two different meshes, reference and target, are used, it is necessary to run two different convergence analyses. The element size on the reference body is chosen using the peak contact pressure and the active contact area as metrics of convergence. In this section we will focus on the selection of the element size for the mesh of the target body and on the effects that it has on the estimation of the springs' length, illustrating the problem adopting ideal geometries. We used as reference body a semisphere of adimensional radius 1, obtained after 6 subdivisions of an icosahedron [20]. It resulted in a mesh of 10 388 triangular elements. As target bodies we constructed 6 different meshes by subdividing an icosahedron of adimensional radius 1.5, which were then cut with an equatorial plane to obtain six semispheres. As the subdivision depth increased, the resulting meshes approximated increasingly better an ideal semisphere. Target meshes are shown in Figure4.2.4. The length of the springs was estimated by means of the ray

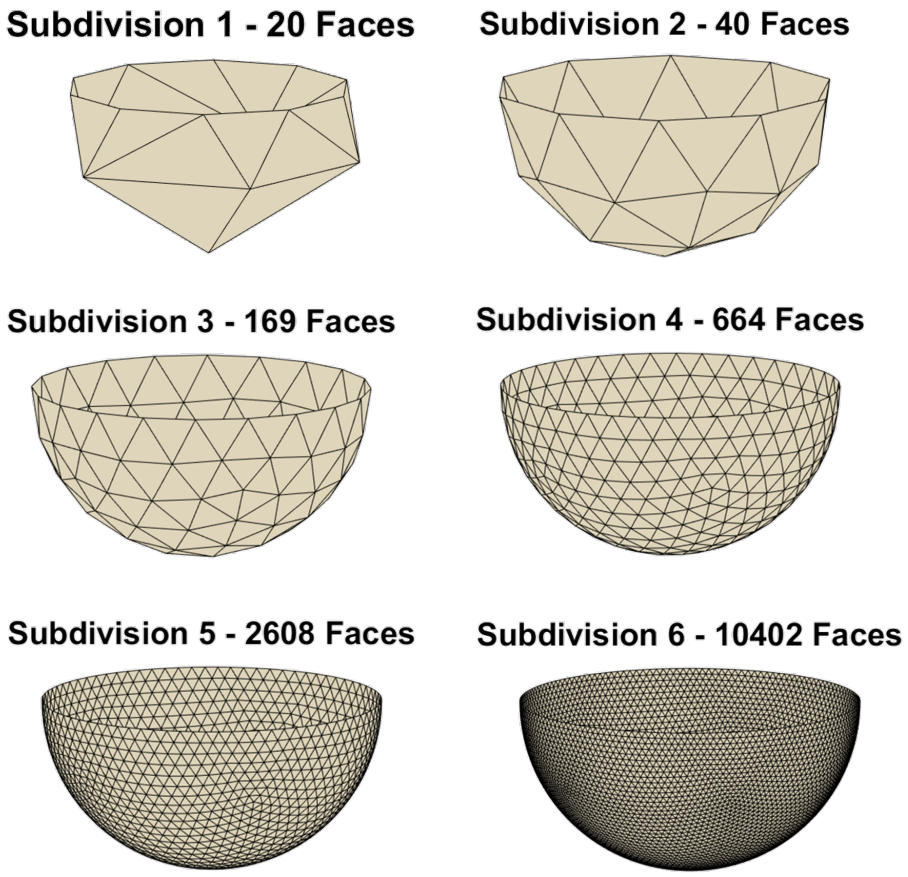

Figure 4.2.4: Ideal target meshes: half spheres obtained through successive subdivisions of the initial icosahedron.

casting algorithm exposed in Section 4.2.1.

Since the two bodies were derived from known ideal geometries, the theoretical distance between the bodies was known as well, being 0.5 for each point of the reference body. Coarsely discretised geometries, however, differed substantially from their ideal counterparts, leading to the computed length far from the theoretical values. Because the distance is uniform the convergence of the mesh could be evaluated using aggregated quantities such as mean and standard deviation of the thickness.

Figure 4.2.5 shows the mean and the standard deviation of the thickness, as a function of the subdivision depth, for the ideal case. Values of mean thickness increased with subdivisions, reaching a converged value of adimensional 0.499. At the same time a decrease of the standard deviation was observed, with final value of 1.5×10^{-5}.

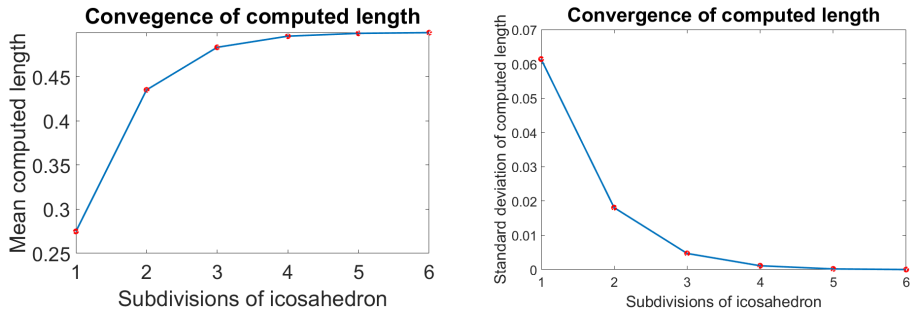

Figure 4.2.5: Convergence study of ideal target meshes. Mean, on the left, and standard deviation of computed length show that the estimated length converges to the theoretical value. Values are adimensional.

Figure 4.2.6 shows the estimated thickness distribution on two different meshes (1 and 3 subdivisions). One can observe that, in both cases, peaks are present in correspondence of the corners of the target domain. Although they are more evident in the coarse case, they are visible also in the refined one. The appearance of such artifacts is inevitable in the estimation of the thickness, but is mitigated by a finer discretisation of the target mesh.

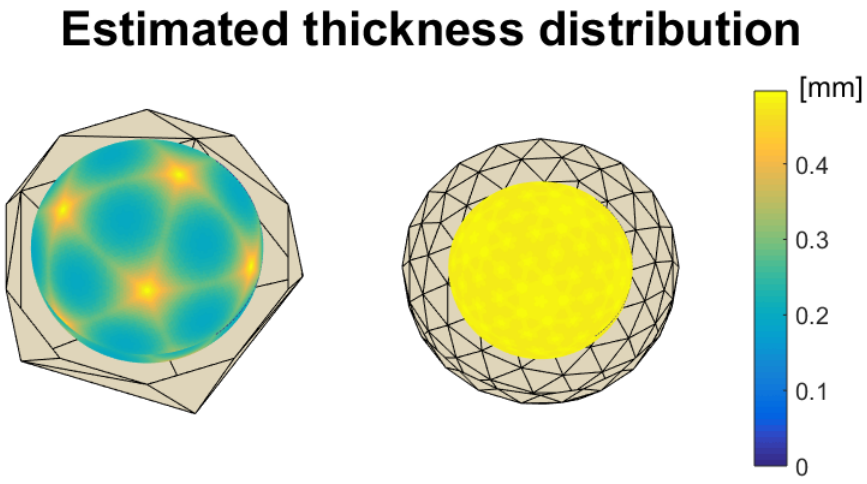

Figure 4.2.6: Estimated thickness on ideal target meshes: 1 and 3 subdivisions.

4.3 Development of DEM and EDEM ankle models

In this section we will present two studies. The first one aims at comparing the differences in prediction from DEM when applied to idealised and real ankle geometries. In the second one, both DEM and EDEM are used to predict the ankle contact pressure distribution during stance, using subject-specific input data from medical images and gait experiments.

4.3.1 Data collection and general pre-processing

Gait data and medical images were collected from one female subject (age: 16 years, weight: 68 kg, height: 160 cm). The data collection took place at the Istituto Giannina Gaslini (Genoa, Italy) within the European Project MD-PAEDIGREE (FP7-ICT Programme, Project ID: 600932). Written informed consent was obtained by the participant and/or her parents. The study was approved by the local medical ethics committees of the participating centres and conducted according to good clinical guidelines and the declaration of Helsinki [180].

The subject performed a static trial and one walking trial at self selected speed.

Ground reaction forces were collected using two force platforms (AMTI OR6-6,1000 Hz). A total of 51 reflective markers, whose locations were chosen according to the Vicon PlugIn Gait (Vicon Motion System Ltd, Oxford, UK) and the modified Oxford Foot Model [220], was attached to the skin of the participant. Their trajectories during the gait were recorded using a stereo-photogrammetric system (Vicon Motion System Ltd, Oxford, UK; 200 Hz). A subset of the markers, 28, was retained during the acquisition of MRI images as their position was used in a later stage to construct the reference frames needed for the musculoskeletal model. MRI of the lower limbs were acquired in supine position with Multi-slice Multi-echo 3D Gradient Echo, with 1 mm slice thickness and 0.5 mm in-plane resolution.

Geometries of talus and tibia were segmented and imported in MeshLab [43], where the articular regions of the two bones were identified. The bodies were then imported in Blender (`https://www.blender.org`), meshed into 7617 and 2974 triangular elements respectively, and made ready for being exported to the software used for the contact modelling, MATLAB (MathWorks, Natick, MA) . The number of mesh elements was chosen after convergence study.

4.3.2 Musculoskeletal modelling

Data collected during the experimental phase have been processed by collaborators within the INSIGNEO Institute for *in-silico* medicine (Sheffield, UK), who finally provided the input data for the contact simulations.

Segmented bone geometries were imported in MeshLab [43] to identify the articular surfaces of hip, knee and ankle. Then, through a custom written MATLAB script, the best least-square fitting surfaces were computed. The ankle was fitted to a cylinder. Bone geometries and best fitting geometrical shapes were imported into NMSBuilder [237] and used for the definition of the axes of the joints to be used in the multibody simulations. The ankle joint was defined as an ideal hinge, whose axis of rotation was parallel to the axis of the cylinder which best fitted the articular surface of the talus. Using MRI images the attachment points of muscles and ligaments were determined and included in the model. Relevant reference

frames were defined according to the recommendations of the International Society of Biomechanics [258].

Ground reaction forces and markers trajectories were used as input for the musculoskeletal simulations in OpenSim [59]. The joint kinematics was reconstructed through a standard inverse kinematics (IK) approach, whilst the estimation of joint contact forces [221] relied on the computation of muscle forces through static optimisation, minimising the sum of the squared activations of all the muscles [53]. Further details on the data collection and the musculoskeletal model are provided in [163].

4.3.3 DEM: application to static loading cases

4.3.3.1 Methods

The meshes of right talus and tibia were imported in MATLAB, together with the location and orientation of the ankle axis of rotation identified in the preprocessing step.

The real geometries of talus and tibia were used as reference for the construction of the ideal meshes. The ideal talus was modelled as a portion of a cylinder, whose radius and axis were identified through a least-square fitting algorithm, and meshed into 2974 triangular elements. The ideal tibia was modelled as two distinct planes, computed through least-square fitting of the tibial plafond and medial malleolus. Because of its piece-wise planar geometry, 4 triangular elements were sufficient for a successful estimation of the cartilage thickness. Figure 4.3.1 shows the real and idealised geometries of talus and tibia, superimposed. Both real and ideal models included four ligaments (anterior and posterior tibiotalar, anterior and posterior talofibular), characterised by a Young's modulus of 255 MPa and represented as bundles of linear springs. The location of their attachment points was identified from the MRI images.

To simulate the two loading scenarios, standing position and toe-off, it was essential to correctly orient the tibia with respect to the talus. To this end two reference frames, one located on the distal part of the tibia and the other one centred

on the talus, were particularly important. The tibial reference frame was able to rotate about one of its axis which was coincident with one axis of the talar reference frame. The angle between these reference frame coherent with the ankle angle computed during the IK stage, and was used to drive the relative orientation of the tibia with respect to the talus [147]. These angles were 0°and 16.31°for standing and toe-off configurations, respectively. The axis and angle of rotation were the same for real and ideal geometries.

Following the correct orientation of the two meshes, a purely compressive spring was placed at the centroid of each triangular element of the talus. The Möller-Trumbore algorithm was used to assign to the springs their initial length. The quality of the MRI scans did not allow to measure the cartilage thickness from the medical images, thus we had to define a threshold based on the data from the literature. It has been set to 3.5 mm, this value being twice the thickness of a typical undeformed layer of cartilage in the ankle joint [70, 161]. The stiffness of the springs was defined as in Eq.3.7. Young's modulus and Poisson's ratio, 10.35 MPa [85] and 0.42 [7] respectively, were considered to be homogeneous over the articular surface of the joint [122].

Half a body weight, 333 N, was applied on the vertical direction to simulate the standing position. A total force of 4190 N, with direction identified from the musculoskeletal model, was applied to simulate the toe-off configuration.

4.3.3.2 Results

In the ideal case the contact region computed in the standing position was regular and well delimited, and occupied 4.68 cm^2 of the total 11.15 cm^2 available talar articular surface (42%). The most loaded region, located on the lateral part of the talus, was subject to 0.6 MPa of maximum pressure. Contact pressure decreased towards the medial side of the joint.

Similar features can be observed in the real model. Active contact area summed to 7.61 cm^2, 48% of the total talar surface. The maximum pressure, 0.76 MPa, was attained on the lateral compartment of the joint, and decreased towards the medial

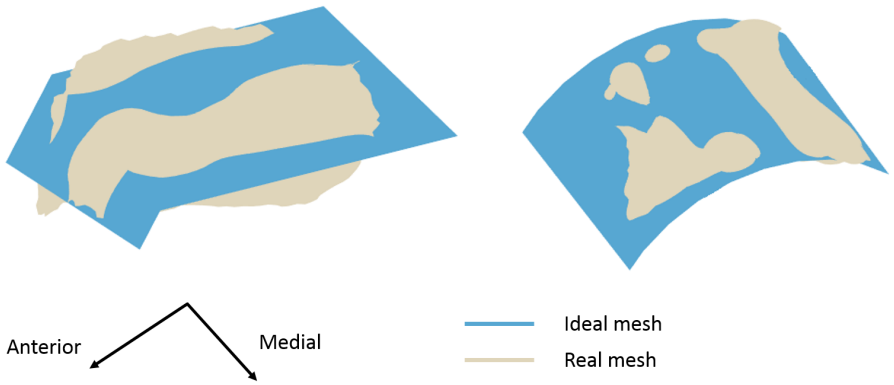

Figure 4.3.1: Superimposition of the ideal (blue) and real (beige) geometries of right talus and tibia.

part. Two relatively large areas which did not make contact were present, the larger on the lateral border of the articular region of the talus and the smaller in a more lateral position. Figure 4.3.2 shows the computed pressure during standing, when the only component of the applied force pointed towards the superior direction.

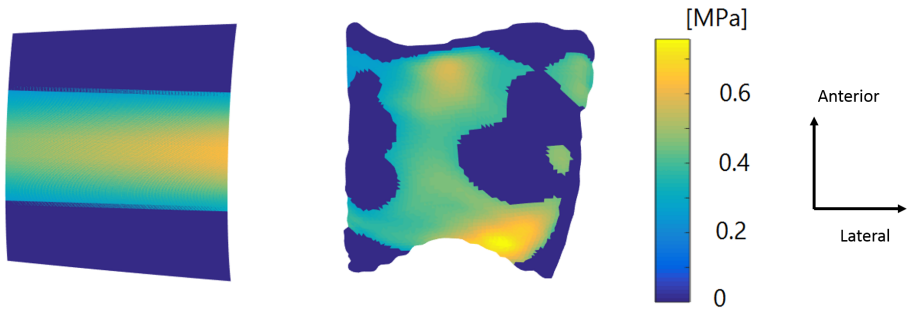

Figure 4.3.2: Pressure distribution during standing, shown on the right talus: ideal (left) and real (right) models of the right ankles.

As shown in Figure 4.3.3, the situation did not differ substantially when simulating the toe-off. The more dorsiflexed position of the ankle implied that the tibia was located more anteriorly than it was during standing, localising the contact region more anteriorly. Interestingly, in the simplified case the active contact area

decreased to 36.7%, whereas an increase to 51.8% was observed on the realistic domain. Resulting peak value of pressure were 7.69 MPa in the ideal case and 8 MPa in the real one, attained on the posterior part of the active region and slightly towards to lateral direction.

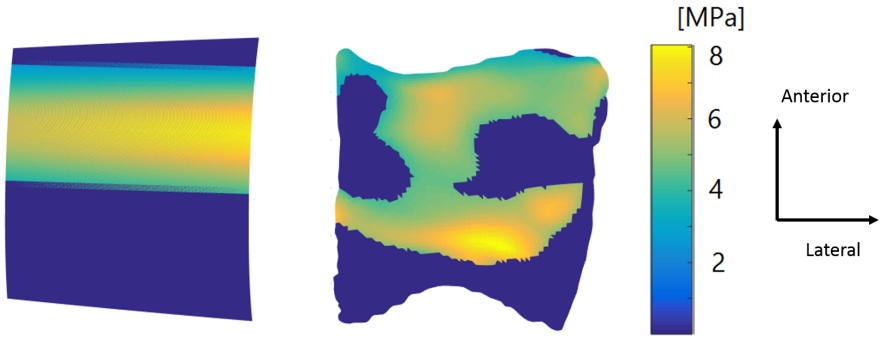

Figure 4.3.3: Pressure distribution at toe-off, shown on the right talus: ideal (left) and real (right) models.

4.3.3.3 Discussion

Although predictions from ideal and real models showed general agreement, some local effects could be caught only by the real one. The springs seen as inactive are such that because their length exceeded the threshold value. Because of the simple geometrical setup, the algorithm converged at the first iteration without producing stretched springs. The reason for the pressure distribution being asymmetric, despite the load having only the vertical component, can be explained with the tilt of the talar cylinder with respect to the applied load. Furthermore, the geometry of the tibia was such that the estimated cartilage thickness had a minimum in the proximity of the lateral section of the joint. According to Eq. 3.7, a minor value of h causes a local increase of the normal stiffness k_d during the computation. Springs with higher stiffness absorbed a higher share of the applied load, causing the pressure distribution to peak.

The same features and behaviour can be observed in the real model. Active contact area summed to 48% of the total articular surface. The maximum pressure, 0.76 MPa, was attained on the lateral compartment of the joint, and decreased towards the medial part because of the orientation of the tibia. Also in this situation the computed thickness showed local minima, responsible for the higher values of stiffness and pressure. Values are higher than in the ideal case because of the less smooth geometry. Two relatively large areas which did not make contact were present, the larger on the lateral border of the articular region of the talus and the smaller in a more lateral position. The tibial plafond of the subject under examination presented two depressions, whose effect was in increasing the computed thickness behind the predetermined threshold and making the corresponding spring considered to be as representative of a non-contacting point. *In vivo* [245] and *in silico* [122] investigations of ankle contact mechanics have reported the existence of such inactive regions.

As shown in Figure 4.3.3, the situation did not differ substantially when simulating the toe-off. Differences in the setup were that in this situation the applied force had also medial and anterior components, and the ankle was in a more dorsiflexed position. The dorsiflexion implied that the tibia was located more anteriorly than it was during standing, localising the contact region more anteriorly. Interestingly, in the simplified case the active contact area decreased to 36.7%, whereas an increase to 51.8% was observed on the realistic domain. This opposite behaviour has its roots, again, in the geometry of the systems: the simplified tibia is a portion of a plane, therefore the estimated thickness depended linearly on the orientation of the tibia. In the real case this dependence was nonlinear because of the complex geometries, with different regions able to make contact according to the imposed joint angle. Nevertheless, in both cases the most loaded region was located in the proximity of the centre of the talus. Resulting peak values of pressure were 7.69 MPa in the ideal case and 8 MPa in the real one.

4.3.4 EDEM and DEM: comparison during stance phase

4.3.4.1 Methods

Medical images and gait data collected and processed as explained in Section 4.3.1, were processed to obtain the input data for the contact model. The ankle joint was modelled as a single degree of freedom hinge with the axis of rotation aligned to the axis of the least-square cylinder fitted to the articular surface of the talus [163]. Tibiotalar angles were estimated using the IK tool in OpenSim [59], while static optimisation [53] and joint reaction analysis [221] provided an estimation of muscle forces and joint reaction forces, respectively. The IK and the joint reaction analysis were performed every 0.01 s, resulting in 65 time points for the subdivision of the stance. The ankle angle and reaction force during the entire stance are displayed in Figure 4.3.4, while values at specific time points are shown in Table 4.3.4.1.

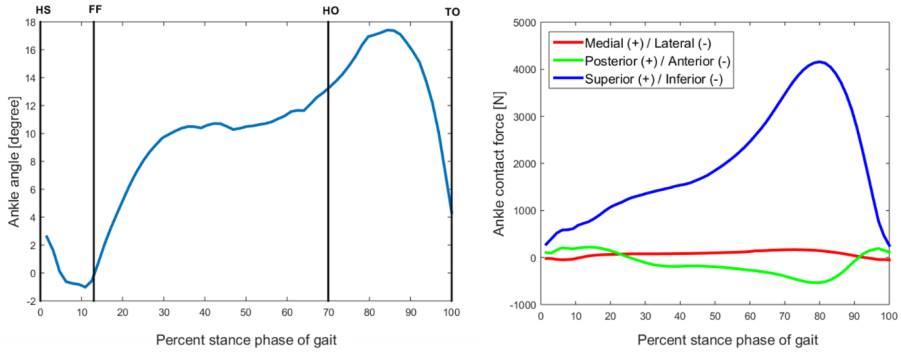

Figure 4.3.4: Kinematics of the ankle joint and applied ankle contact force. The force is applied on the talus. HS indicates the heel strike (0% of stance), FF the foot flat (13% of stance), HO the heel off (70% of stance), TO the toe off (100% of stance).

% of stance	Ankle angle	Medial/Lateral +/-	Posterior/Anterior +/-	Superior/Inferior +/-
12	-0.57°	13.64 N	21.7 N	72.5 N
20	5.37°	65.25 N	143.87 N	1071 N
55	10.7°	106.86 N	-22.14 N	2047
69	12.92°	158.82 N	-35.45 N	3209.7 N
78	16.31°	159.94 N	-52.52 N	4078.26 N
87	17.1°	89.32 N	-33.88 N	3714.94 N
92	15.1°	28.2 N	-29.24 N	2741.62 N

The real geometries presented in the previous sections were used to represent the ankle joint. At each time point, the tibia was rotated about its axis of rotation to align the tibial and talar references frames with the joint angle computed during IK. Each triangular element on the talus was then endowed with a purely compressive spring oriented accordingly to the local normal vector to the discretised surface. One end of the springs was located on the talus, while the location of the second one was estimated using the Möller-Trumbore algorithm [164], which also provided an estimate of the local cartilage thickness. The cartilage thickness threshold was set to 3.5 mm, twice the thickness of a typical undeformed layer of cartilage in the tibiotalar joint [161]. Four ligaments (anterior and posterior tibiotalar, anterior and posterior talofibular), whose attachment points were identified from the MRI, were included as bundles of linear springs. Their Young's modulus was set to 255 MPa [213]. The geometry of the right ankle joint is shown in Figure 4.3.5.

Following the application of the ankle force the talus was allowed to translate in three directions in search for an equilibrium configuration. The rotations of the talus were constrained to zero to keep the ankle axis of rotation parallel to itself during the entire simulation. This behaviour was enforced by minimising the energy of the system, Eq. 3.10 and Eq. 3.17 in case of DEM and EDEM respectively, with the constraint that the rotational components of the generalised displacement are

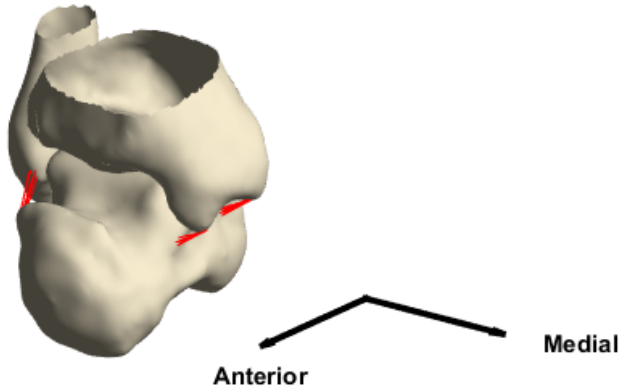

Figure 4.3.5: Geometries of talus and tibia in the real ankle model.

equal to zero.

The contact features of the joint during stance were computed using DEM and EDEM. In case of DEM, after the computation of the solution at time t, the talus was not displaced from its initial position and the configurations of the system at two time points differed only because of the orientation of the tibia. In EDEM, instead, the equilibrium displacement was used to update the position of the talus for the following time step. Only after this had been done the tibia was then rotated. In each case the length of the springs was computed at the beginning of each time step to determine the global stiffness matrix of the system. The schematic pipeline of the musculoskeletal and contact models is shown in Figure 4.3.6.

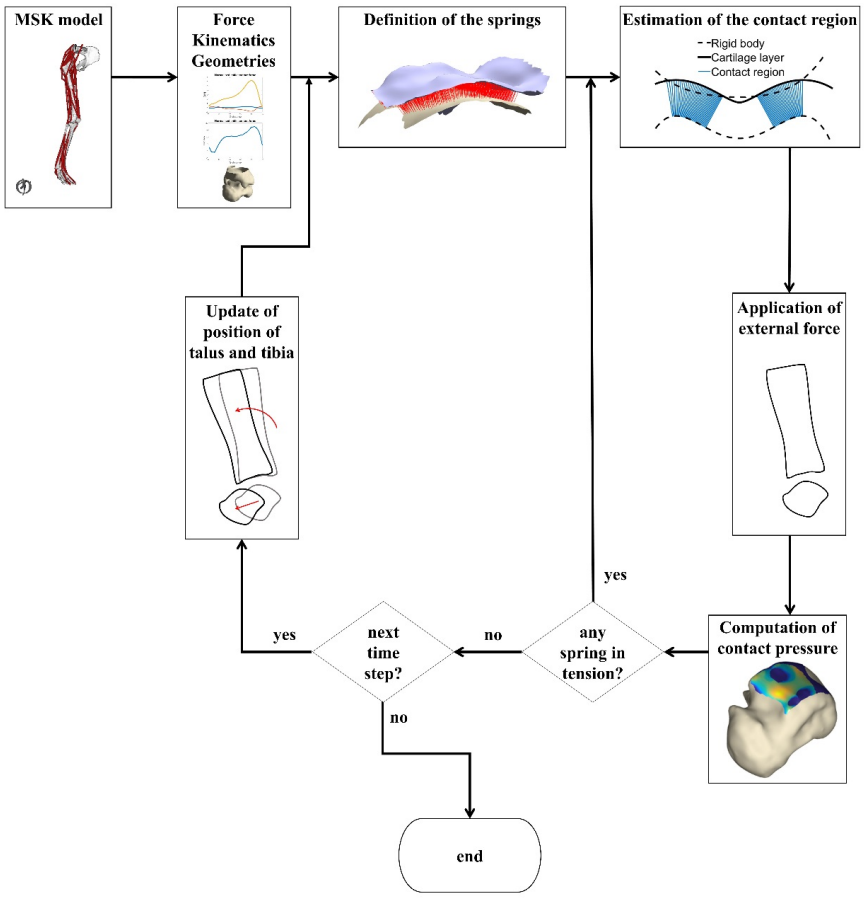

Figure 4.3.6: Schematic pipeline of the interaction between subject specific musculoskeletal model and subject specific ankle contact model.

We assessed the dependency of the peak contact pressure, as computed by EDEM, on two input parameters which were determined from the literature: the thickness of the undeformed layer of cartilage [161], used to define the spring length threshold, and the ligaments' Young's modulus [213]. We did not investigate the effect of the cartilage Young's modulus, as under our modelling assumption the effect on the contact pressure was essentially linear. The spring length threshold and the Young's modulus of the ligaments were varied uniformly within the input space $[2.5, 4.5]$ mm and $[200, 350]$ MPa respectively. The parameter space was discretised into 20×20 points. Sensitivity to the inputs was assessed by evaluating the

gradient of the peak pressure.

4.3.4.2 Results

For what concerns EDEM, it predicted a steady displacement of the talus in the superior direction, towards the tibia. At about 80% of the stance, immediately before toe-off, the talus was located 0.57 mm superiorly with respect to its original position. Displacements in the other direction were substantially smaller, with maximum values smaller than 0.1 mm. After toe-off the talus was then displaced back towards its initial position, driven by the decrease of the applied force. The contact region showed a smooth time evolution: as the gait progressed it moved forwards from the posterior to the anterior part of the joint. At the same time it enlarged and reached its maximum extension, 5.2 mm^2 at the toe-off, sharply shrinking afterwards. The maximum peak contact pressure was attained at 80% of stance on the anterior part of the talus. In this individual, at 9.25° of dorsiflexion the distance between tibia and talus was minimum. High values of contact pressure were shown in the anterior and anterolateral part of the joint as well. These three zones encircled a region, close to the centre of the articular surface of the talus, which was always inactive. Figure 4.3.7 shows the pressure distribution at selected instants of time.

The pattern of contact pressure predicted by EDEM and DEM showed similarities and differences. The average contact area was 4.67 cm^2 for EDEM and 4.18 cm^2, 11% smaller, for DEM (Figure 4.3.8)

The anterior part of the talus was recognised by both methods as the most loaded from both methods. However, as shown in Figure 4.3.9 for the instant of maximum loading this holds for every time points of the simulation, DEM predicted a more evenly distributed field of contact pressure, whereas in EDEM local peaks were present. Maximum values were 7.3 MPa and 6.92 MPa for EDEM and DEM, respectively.

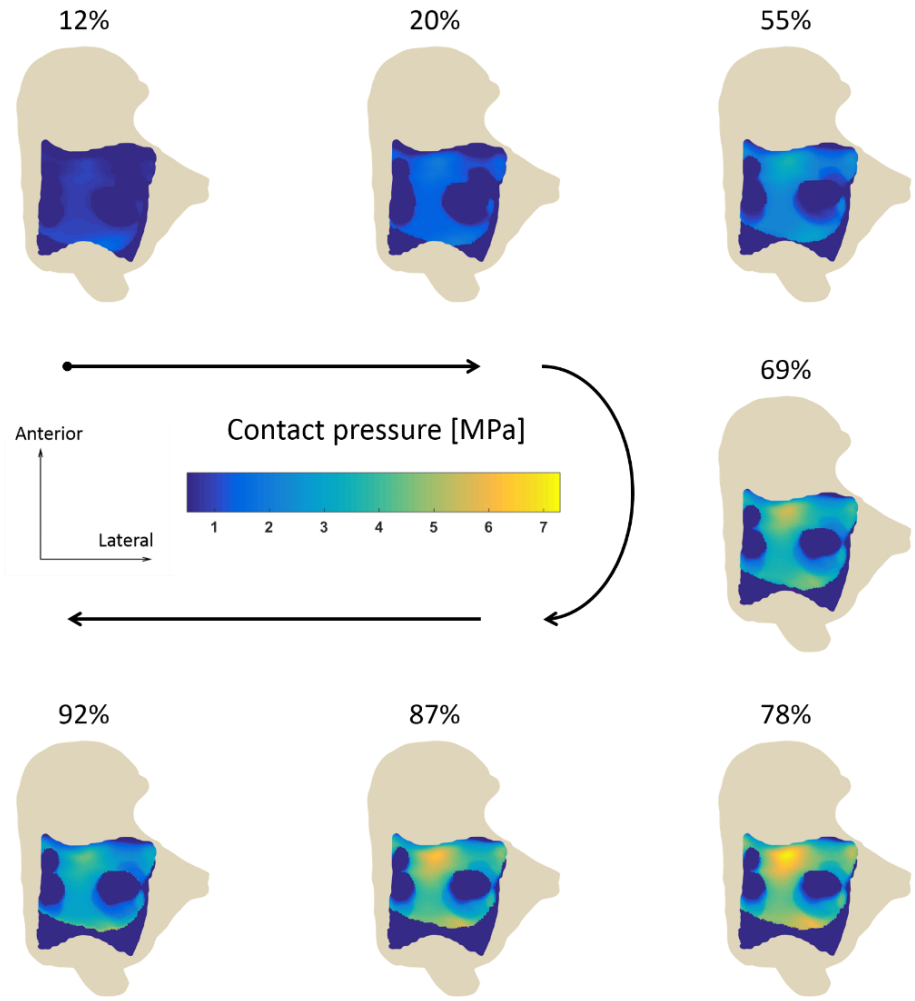

Figure 4.3.7: Pressure distribution on the talus at selected time points of the stance, computed using EDEM. The arrows indicate the progression of stance. The pressure increased as the talus was displaced towards the tibia, reaching its maximum at 78% of the stance phase, and then decreased as the talus was displaced backwards.

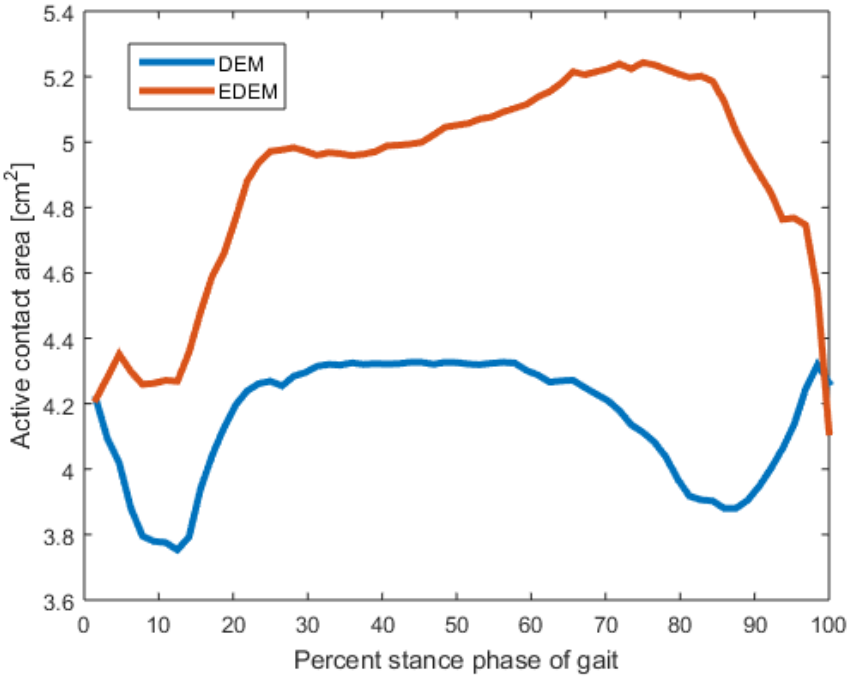

Figure 4.3.8: Active contact area during the stance, comparison between EDEM and DEM.

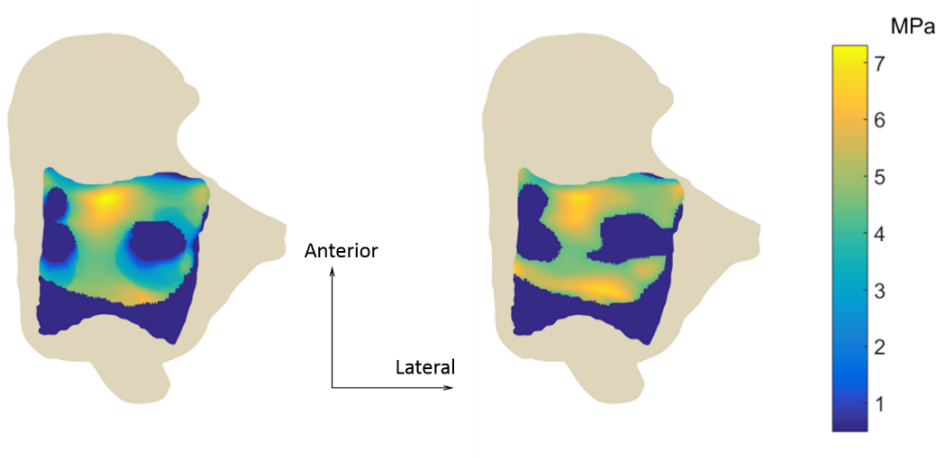

Figure 4.3.9: Pressure distribution at the instant of maximum loading, as computed from EDEM (left) and DEM (right).

The sensitivity analysis showed that the parameter which influenced mostly the contact pressure was the thickness threshold, whilst the ligaments' Young's modulus had a less pronounced effect (Figure 4.3.10). Keeping the threshold constant to h_T =3.5 mm and varying the Young's modulus of the ligaments from 200 MPa to 350 MPa, an increase of 175%, affected the contact pressure of 3% only. Conversely, as Figure 4.3.11 illustrates, the increase of threshold from 2.5 mm to 4.5 mm reduced the pressure by 30%. As shown by Figure 4.3.8, the same effect of the input parameters can be identified on the extension of the contact area and the corresponding pressure distribution. Increasing the length threshold allows the system to recruit more springs, therefore increasing the contact area, whereas modification of the Young's modulus of the ligaments affect the contact area only marginally.

4.3.4.3 Discussion

Global measures reported in the literature, such as peak contact pressure or contact area, tend to be homogeneous and easier to compare than local ones, which

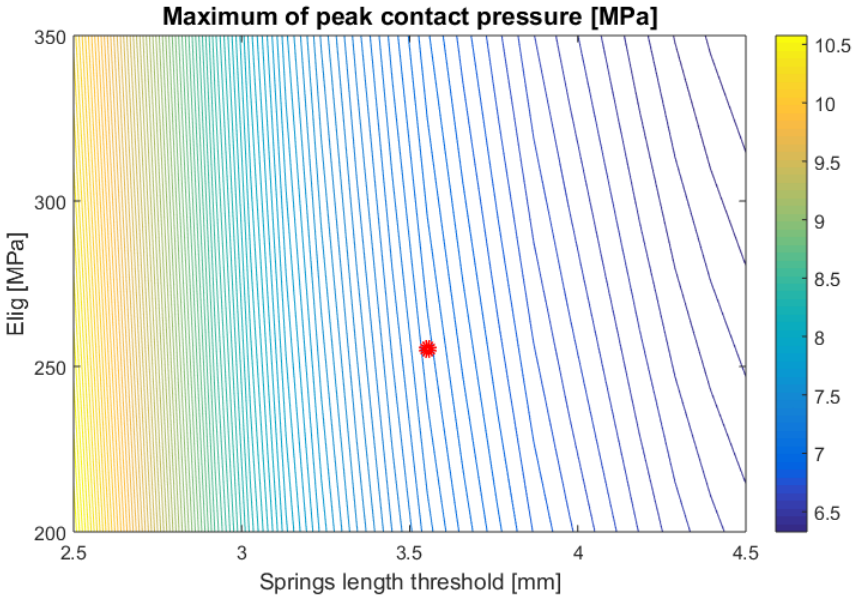

Figure 4.3.10: Dependency of the peak contact pressure on the Young's modulus of the ligaments and on the springs' length threshold.

are comparable only in a qualitative manner. The contact features of cadaveric ankles have been investigated by several authors [35, 64, 149, 222, 230, 242], who performed studies under a large variety of applied load, geometries, experimental setups and joint configuration. Calhoun and colleagues [35] reported an increase of the contact area when the ankle went from plantarflexion to dorsiflexion. Macko and collaborators confirmed this results, measuring values from 3.81 cm^2 to 5.40 cm^2, whilst some others [21] observed opposite behaviours. Following the application of loads ranging from 200 N to 1500 N on eight cadaveric ankles, Kimizuka and colleagues [129] reported contact areas from 1.96 cm^2 to 6.18 cm^2. *In vivo* measurements during stance, using imaging techniques, were performed by Wan et al. [245], who observed values between 2.72 cm^2 and 4 cm^2. The subject investigated in our study presented a gait pattern mostly in dorsiflexion. The contact area increased with the dorsiflexion angle, and had an average value of 4.67 cm^2, in line with experimental results reported in the literature.

According to EDEM, two regions in the central part of the talus were never in-

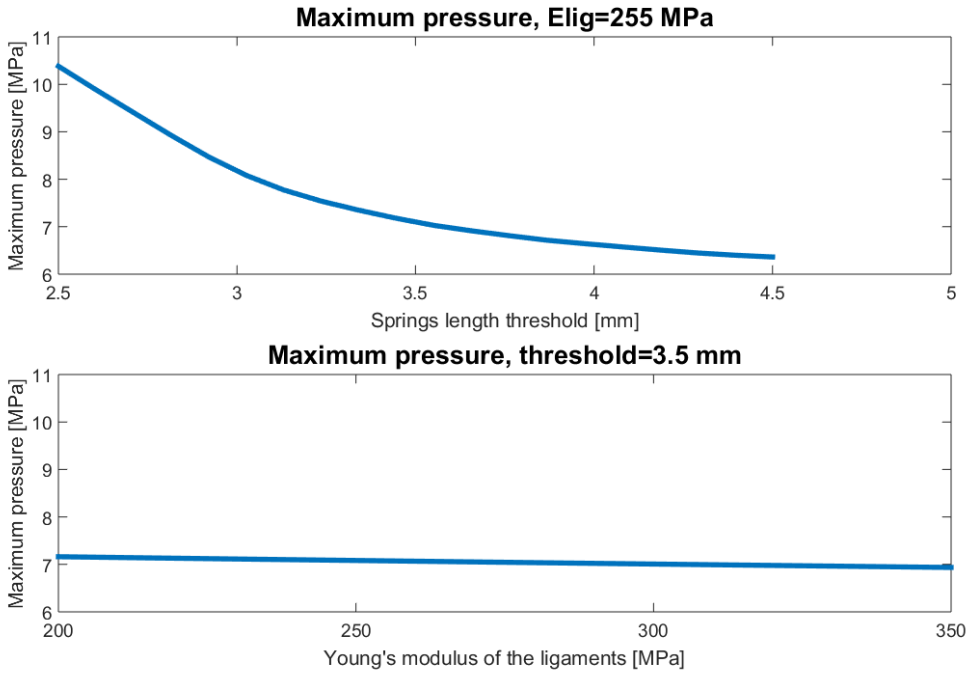

Figure 4.3.11: Line plots of the behaviour of the maximum pressure when only one input parameter is varied. In the top image the Young's modulus of the ligaments is fixed to 255 MPa, in the bottom one the springs' length threshold is kept to 3.5 mm.

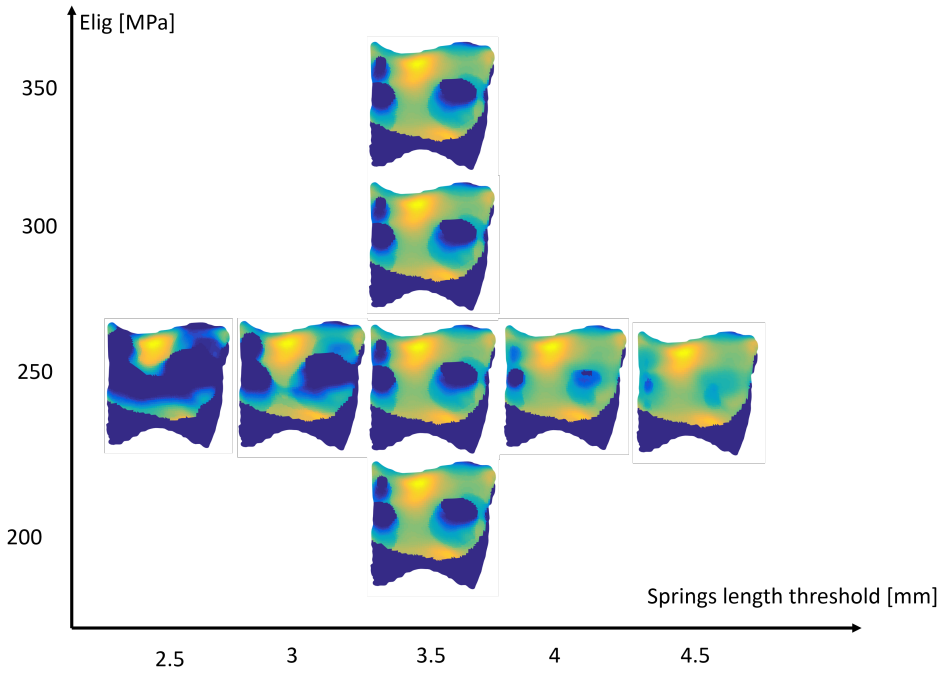

Figure 4.3.12: Dependency of the contact pressure distribution on the Young's modulus of the ligaments and on the springs' length threshold. The range of variation of peak values, from 6 to 10.5 MPa did not allow for the inclusion of the scale.

volved in contact during stance. *In vivo* [245] and computational [122] studies have reported the existence of such regions. Their existence depends strongly on the geometry of the individual under investigation. The subject investigated in our study presented two depressions on the tibial plafond. During the estimation of the cartilage thickness, the springs whose target attachment point was located inside these depression were assigned a value of computed thickness higher than the fixed threshold, which made them inactive for all the duration of the contact process.

Tochigi et al. [230] applied 600 N of axial load on a set of cadaveric ankles, measuring 5 MPa of peak pressure, with the most loaded region in the anterolateral part of the joint. Similar results, with 10 MPa of peak pressure, were obtained by Kimizuka and colleagues [129]. Vrahas et al. [242], instead, observed peak values from 1.9 MPa to 12.4 MPa concentrated in the anteromedial part of their specimens. In a dynamic study on eight cadaveric joints, Suckel et al. [224] reported the maximum pressure to be located on the lateral side in half of the cases, and on the medial in the remaining. Average values were 4 MPa. Results from *in silico* studies are similarly variegated, with peak contact pressure of 3.74 MPa [147], 4 MPa [8], 8 MPa [3] and 14 MPa [7] obtained under a wide variety of applied loads. Given that the results from the literature were obtained under many different conditions only qualitative comparisons are possible. Maximum value of the predicted peak contact pressure, 7.3 MPa, and its location, the anterior part of the talus, are aligned with the values found in the literature.

Despite similarities in the peak values, the two methods predicted different contact regions and pressure distributions. The reason for that is the displacement of the talus, which in EDEM is allowed while in DEM is not. Pushed by the ankle contact force, in EDEM the talus was displaced towards the tibia: this resulted in an estimated cartilage thickness lower for EDEM than it was for DEM. The immediate consequence was that in EDEM more springs could be recruited in the contact area. Despite a larger contact area, EDEM predicted higher peak values and a less uniform pressure distribution. According to Eq. 3.7, strained springs present an higher value of stiffness during the computation. When subject to an external

force they tend to hold a larger part of the load, leaving the remaining springs with a minor share of the applied load to hold. Regions of concentration of strains were also observed by Wan et al. [245]. DEM did not allow for the talus to be displaced, therefore estimating a more uniform thickness and pressure distribution.

As shown by the global sensitivity analysis, EDEM is more sensitive to the spring thickness threshold than to the ligaments' Young's modulus. Increasing the stiffness of the ligaments reduced the contact pressure by a small amount, coherently with observations in the literature that the main contributor to the motion of the ankle is the topology of the articular cartilage [230, 249]. An alteration of the spring threshold changes radically, and non-linearly, the contact pressure because it changed the number of candidate springs to be recruited into the contact region.

This study has some limitations. First of all, despite the inclusion of the strain dependent properties of the cartilage, the material was still treated as elastic. This is a relatively common hypothesis in the development of computational models of the joints [2, 85, 97, 122], often considerate appropriate to the loading and time scales considered [14]. This modelling assumption, although reasonable in most cases, limits the range of loading scenarios that can be simulated. Second, the cartilage thickness was estimated rather than measured from clinical data and, since the MRIs were acquired in supine position, this might lead to an overestimation of the values. Third, the model does possesses time dependent features such as the tracking of the position of tibia and talus and the update of the values of cartilage stiffness, but it is not dynamic and does not include the effects do the inertia. However, in their DEM based model of the patellofemoral joint Akbar and colleagues [2] have shown that quasi-static and dynamic predictions are nearly equivalent in the simulation of daily activities. Further investigations must be conducted on the ankle joint. Fourth, our results might benefit from a more detailed representation of the behaviour of the ligaments of the ankle joints. The sensitivity analysis however shows that the stiffness of the ligaments has a limited effect on the determination of the contact pressure, suggesting that this is not crucial for the simulation of physiological movements. Finally, only one subject has been analysed, not permitting the investigation of the effects that the variability of certain factors (i.e. age, gen-

der, joint status) could have on the final outputs of the model.

Despite the above mentioned limitations, the presented study showed the the EDEM is able to produce results in line with the experimental and computational literature on the behaviour of the ankle joint during physiological activities.

4.4 Discussion

In this chapter we have discussed some aspects related to the implementation and personalisation of ankle joint models based on DEM and EDEM. A simple case has been presented to test that the DEM was implemented correctly. Finally, predictions of DEM and EDEM have been compared on subject specific ankle geometries, and the sensitivity of EDEM output to two input parameters has been evaluated.

5

Comparison of EDEM outputs against experimental data

5.1 Introduction

Osteoarthritis (OA) is a common clinical problem which frequently affects the ankle [188], profoundly influences the quality of life of the people who suffer from it [60, 158, 160], and constitutes a heavy burden on the healthcare systems of many countries in the western world [40, 76, 107]. Although an uniform consensus on its etiology has not been reached yet it is generally acknowledged that altered joint loading characteristics might trigger the onset and development of the disease [52, 73]. The forces generated during the gait are transmitted to the articular cartilage which covers the extremities of the articulating bones. The field of contact pressure which generates within the tissue is responsible for the transmission of the load

and, if outside physiological ranges, can cause the degradation of the cartilage [156, 204].

The pattern of joint contact pressure distribution carries important information on the behaviour of the joint. Its estimation, however, poses several challenges. Except for rare occasions where *in-vivo* measurements are available through instrumented prostheses [106, 132, 252] , researchers and physicians have to rely on estimations obtained either from computational models of the joint or from *in-vitro* experiments performed using cadaveric specimens . Computational models have been used and validated at the hip [6], knee [143] and ankle [8] joints, mostly in static scenarios.

Although computer simulations are extremely versatile because allow for the investigation of situations which could be difficult to obtain *in-vivo*, there is a general lack of experimental data to assess their predictions. Data can be gathered by using pressure sensitive sheets which are inserted inside cadaveric joint specimens by experienced surgeons. Several authors have used this technique [8, 17, 21, 35, 206, 222, 225] in a variety of scenarios, investigating healthy joints [129, 253] or the effect of ligament resection [32] and fractures malunion [229, 242]. Common limitations of this approach are the use of an external loading device which applies a single external force to the specimen, and measurements are often performed in static situations. Dynamic simulations of the movement of the foot complex are possible using cadaveric gait simulators (CGS) [68, 94, 111, 127, 130, 140, 171, 179, 187]. These devices can differ for the design and the number of degrees of freedom they can control, but all share the possibility of applying gait kinematics and muscle forces to cadaveric foot specimens. The simulation of the kinematics is achieved by means of linear and rotational motors, while muscle forces are applied through hydraulic actuators which pull the muscle tendon units to produce the desired force. CGSs are usually controlled real-time in feedback loops and allow to measure gait parameters such as the individual bone kinematics, ligaments strain or contact pressure distribution which would otherwise be inaccessible.

In this study we use the pressure data collected by Natsakis and colleagues at KU Leuven (Leuven, Belgium) using a CGS they have developed in recent years [171],

to assess the performance of the computational model we have developed in this thesis. Natsakis and colleagues performed the data collection from the living subject, the acquisition of the scans of the cadaveric specimen and the experiments described in Section 5.2.1, and provided us with the geometries, forces and kinematics used for the contact study described in Section 5.2.2.

5.2 Material and methods

This section is divided into two parts: the first provides the details of the experimental study, performed at KU Leuven, and the second presents the details of the computational simulations. The pipeline of the study is depicted in Figure 5.2.1.

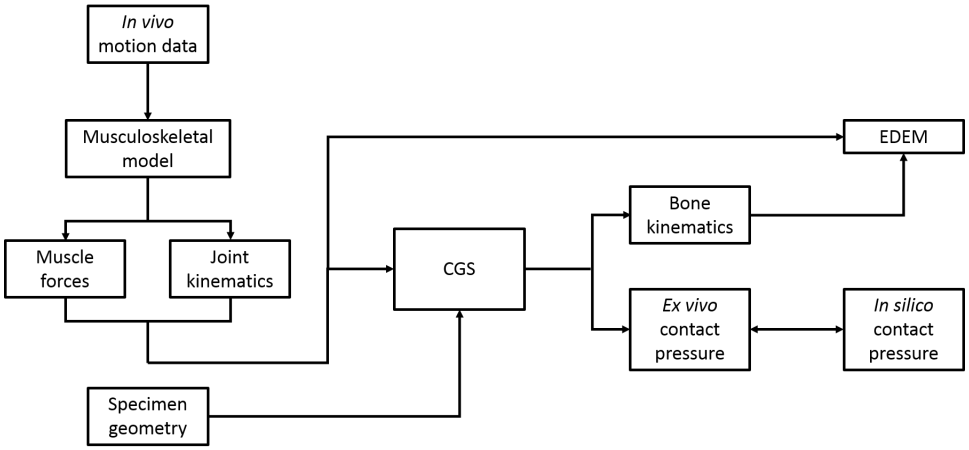

Figure 5.2.1: Workflow of the validation study.

5.2.1 In vitro gait simulations

The input variables for the CGS, namely the joint kinematics, ground reaction force and muscle force, were obtained after processing of *in-vivo* data collected from a 47.9 kg female individual who performed a walking trial at self selected speed. Standard inverse kinematics and static optimisation [53] were performed

on a generic OpenSim model [59] to estimate the ankle kinematics and the muscle forces. Prior to simulations the model was scaled to match the anthropometric measures of the subject.

Three components are essential in the analysis of the human motion: the kinematics, the ground reaction force and the muscle forces. The CGS permits the application of these three to a specimen of the human foot. A cadaveric specimen of the left foot, amputated mid-tibially, was placed in the CGS developed by Natsakis et al.[174]. The specimen was attached, at its most superior point, to a carriage hinged to a moving rail. The carriage was able to slide horizontally and constrain the motion of the specimen in the vertical direction. Because of the hinge connection to the rail, the carriage could also rotate simulating the flexion-extension movement of the knee. The centre of rotation was approximately correspondent to the knee. A representation of the cadaveric gait simulator is shown in Figure 5.2.2.

The sole of the foot was in contact with a moving platform, actuated by pneumatic actuators and able to translate vertically, which simulated the vertical kinematics of the foot-tibia complex and the application of the vertical ground reaction force. The amplitude of the displacement of the platform and, indirectly, the magnitude of the vertical ground reaction force, were controlled by modulating the input pressure of the actuators. A feedback loop guaranteed that the force measured by pressure sensors and load cells matched the ground reaction force obtained through analytical modelling [172]. Figure 5.2.3 shows the free body diagram of the foot specimen when in contact with the moving platform.

The horizontal kinematics was imposed by translating the carriage over the rail using an electric servo motor (Bosch Rexroth AG, type MSK061C, Bosch Group, Germany). The imposed tibial kinematics was derived by means of a specimen-specific kinematic model which used as inputs the measures of tibia and foot to produce the horizontal translation of the knee and the tibiotalar angle [171].

Muscle activation, the driving force behind human motion, was simulated through six pneumatic actuators (Festo, AF & Co. KG, Sankt Ingbert, Germany). Com-

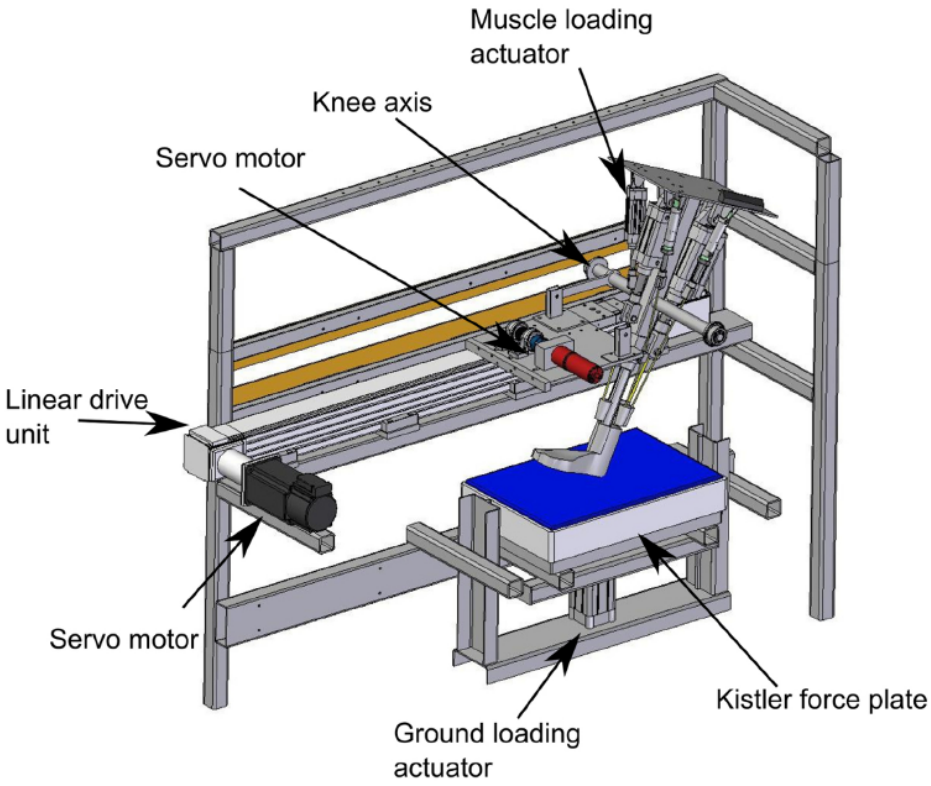

Figure 5.2.2: The cadaveric gait simulator and its components. Figure from [172].

puted muscle forces were then downscaled by a factor of 2 to be used as input by the actuators. The scaling was performed in order not to damage the sample, and it is a common operation when performing *in-vitro* gait simulations[15, 224]. In addition to the scaling, the muscle forces were modified to obtain a spectrum of muscle activations able to generate different kinematics. A total of 5 trials were simulated. The actuators were clamped to the muscle tendons, which were grouped in six groups of tendons with similar functions [173] as shown in Table 5.2.1.

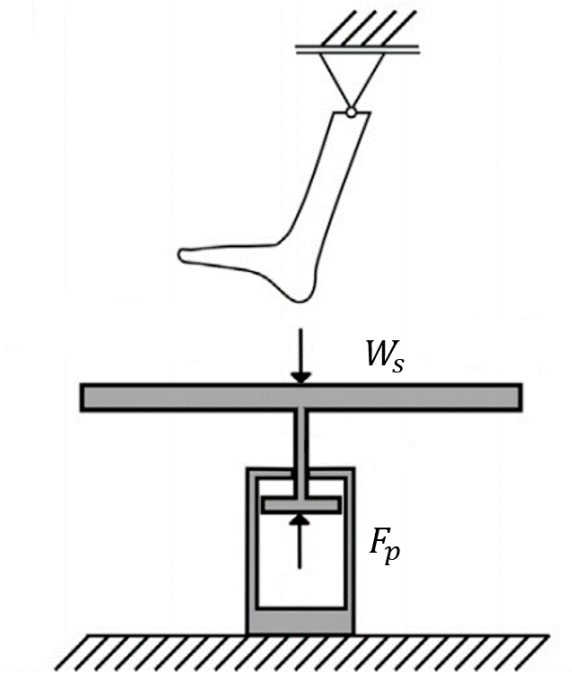

Figure 5.2.3: The force $\mathbf{F}_p$ expressed by the platform matches the force $\mathbf{W}_s$, defined by the weight of the platform, of the foot specimen and a scaling functon. Adapted from [172].

Group number	Group name	Muscles
1	Peroneal muscles	Peroneus longus
		Peroneus brevis
2	Tibialis anterior	Tibialis anterior
		Extensor digitorum
		Extensor hallucis
3	Tibialis posterior	Tibialis posterior
4	Flexor hallucis longus	Flexor hallucis longus
5	Flexor digitorum longus	Flexor digitorum longus
6	Triceps surae	Gastrocnemius
		Soleus

The typical magnitude of the force expressed by the muscle groups during a the

stance phase of the gait cycle, as computed from static optimisation and after the linear scaling, is shown in Figure 5.2.4.

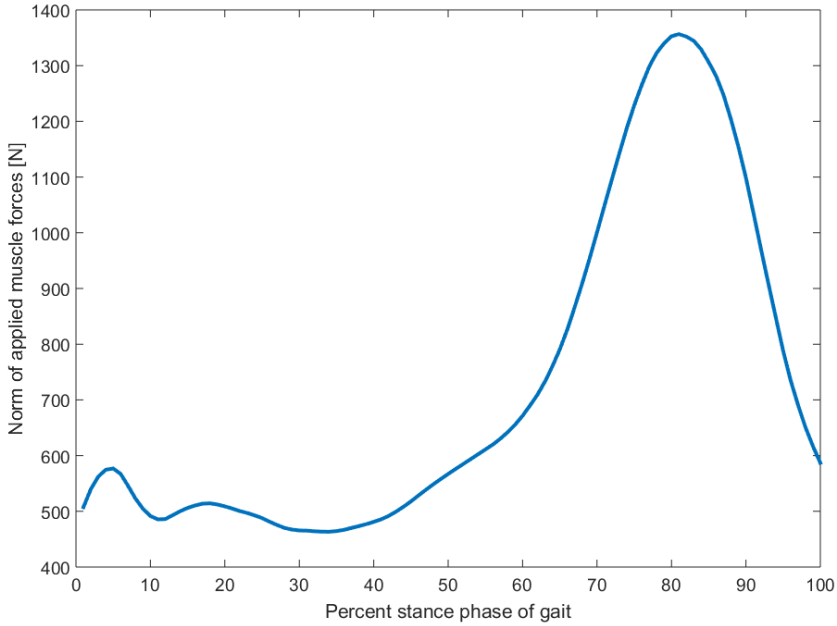

Figure 5.2.4: Norm of applied muscle force.

The specimen was fitted with five intracortical bone pins (diameter: 4 mm, length: 50 mm, ICOS, New Deal, France), attached to tibia, talus, calcaneus, navicular and cuboid. An anterior vertical incision was performed through the skin, inferior extensor retinaculum and joint capsule to allow the insertion of a pressure sensitive Tekscan #5033 sensor (Tekscan Inc, Boston, MA). The sensor covered the articular part of the tibia, and was attached through a screw placed on a non-sensitive area. These operations were performed by an experienced foot surgeon.

Computed tomography (CT) scans of the specimen were then acquired to identify the bone geometry and the precise location of the pressure sensor and the bone pins. The three dimensional kinematics of tibia and talus during the simulated gait was measured using a Krypton optoelectronic motion capture system

(K 600, Metris, Belgium; 100 Hz). Four active markers were attached to the tip of each bone pin, making possible to define orthogonal reference frames for the determination of the three dimensional kinematics of the bones during the simulated activity. At the same time, the pressure sensor recorded the contact pressure between talus and tibia. Figure 5.2.5 shows the geometries of tibia and talus as obtained from the CT scans.

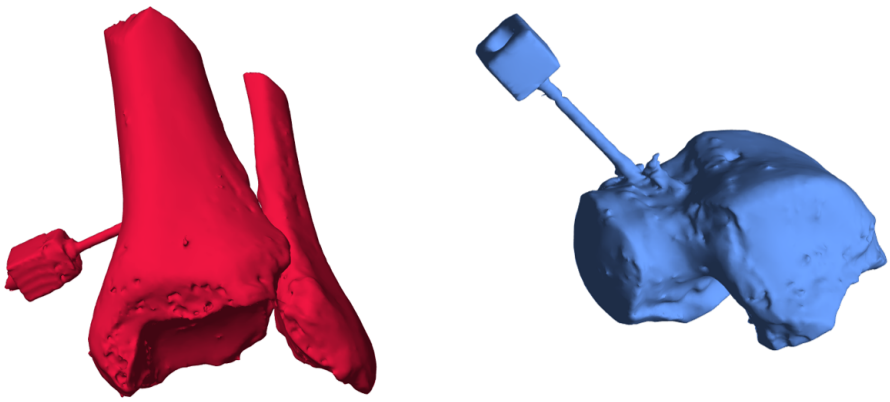

Figure 5.2.5: Anterior view of the full geometries of talus and tibia.

5.2.2 Contact modelling

The contact modelling part of the study was performed at the INSIGNEO Institute for *in-silico* medicine (Sheffield, UK) . The geometries obtained from the CT scan were converted into stereo lithography interface format (STL), resulting in meshes of 46 154 and 63 390 triangular elements for talus and tibia, respectively. Contact simulations were run on a subset of the full meshes, namely the articular part of the tibia (3268 triangles) and the subset of the full talar mesh where the pressure sensor was located. The mesh was originally composed of 2325 triangular elements but, since the number was not adequate for the contact simulation, we performed 3 iterations of Laplacian smoothing [75] in Blender and remeshed the domain into

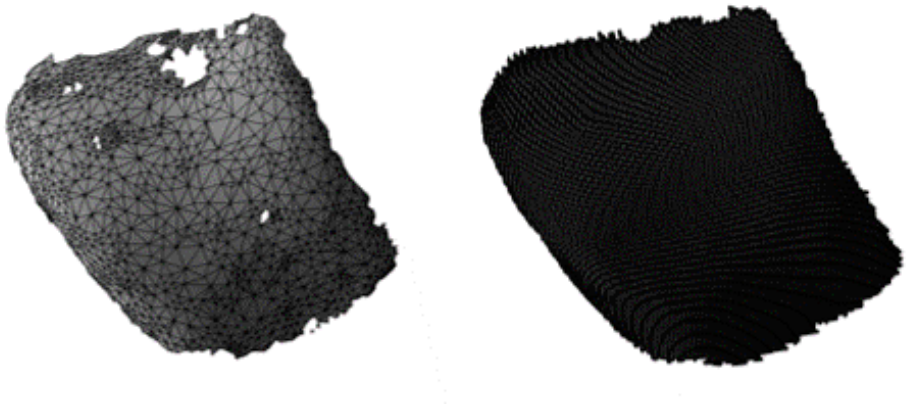

Figure 5.2.6: Superior view of the computational domains before and after refinement. Left: original mesh, 2325 triangles. Right: final mesh, 27631 triangles.

27 631 elements. Figure 5.2.6 shows the meshes before and after the refinement.

Bone geometries of tibia and talus were imported into MATLAB (MathWorks, Natick, MA) for the contact simulation. Anatomical landmarks were identified on the bony surfaces of talus and tibia to allow the definition of two references frames $\mathcal{R}_{Tal}^{STL}$ and $\mathcal{R}_{Tib}^{STL}$ which were used to express the relative motion of the talus with respect to the tibia during the contact simulation. The first landmark of the tibia was located on the medial malleolus, the second on the lateral malleolus and the third at the centre of the fibula. The origin was in the middle between the two malleoli. The first landmark on the talus was the centre of the talus head, the second was the most posterior point of the bone and the third its most lateral point. Because of the structure of the data, preliminary operations were required to impose to the meshes the measured kinematics. When they were imported in MATLAB, in a configuration which we call the "STL configuration", the two meshes were representative of the bones in their physiological position: their reference frames were not aligned and their origins were not coincident, and they were not located at the origin of the global MATLAB reference frame. A different linear transformation was then applied to each of the reference frames in order to make them coincident with the global one, bringing the two bodies in a configuration which we call

"HOME configuration": these transformations $\mathbf{T}_{Tal}^{STL\to H}$ and $\mathbf{T}_{Tib}^{STL\to H}$ bring $\mathcal{R}_{Tal}$ and $\mathcal{R}_{Tib}$ into $\mathcal{R}_{Tal}^{H}$ and $\mathcal{R}_{Tib}^{H}$ respectively. The nature of the transformations was such that the two systems were now coincident, causing the two meshes to intersect in several regions. The kinematics at time t was expressed with respect to this configuration using a transformation $\mathbf{T}_{Tal}^{H\to t}$, composed of a translational and a rotational part, which acted on the talus moving $\mathcal{R}_{Tal}^{H}$ to the desired "KINEMATICS configuration" $\mathcal{R}_{Tal}^{t}$. The tibia was kept in its HOME configuration for the whole simulation. Figure 5.2.7 illustrates the STL, HOME and KINEMATICS configurations by showing the different positions of the reference frames.

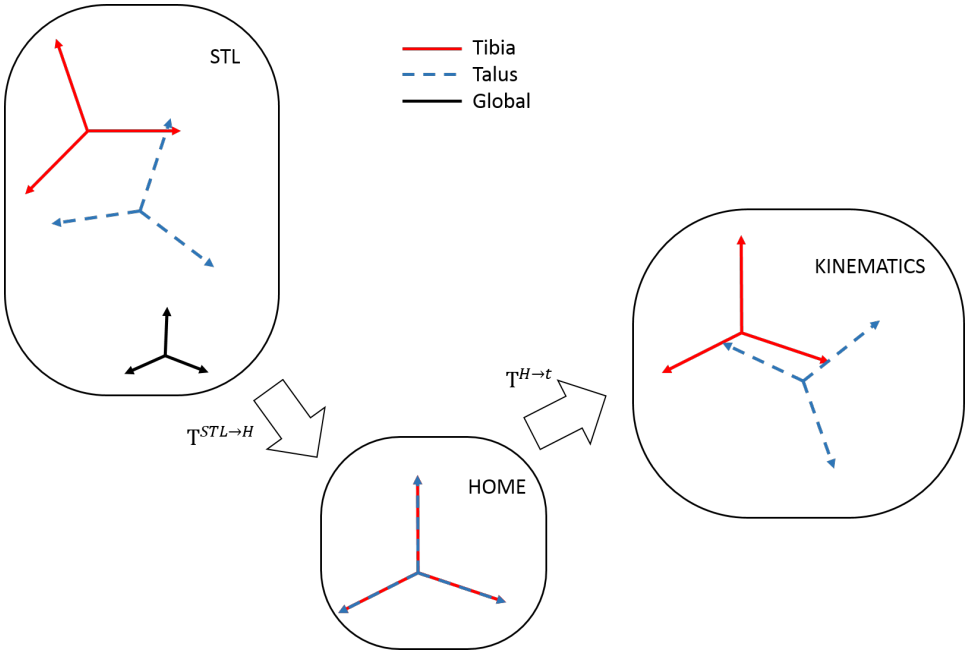

Figure 5.2.7: Original kinematics of the system. The motion of the talus with respect to the tibia is expressed as a transformation from the HOME configuration. Note that the tibia is not moved in this process.

It happened, however, that for some time points the reconstructed kinematics caused intersection of the meshes, especially in the antero-lateral compartment of the ankle joint. To avoid this we decided to disregard the translational part of the kinematics and define new kinematic transformations. From the STL configura-

tions both the meshes were displaced using $\mathbf{T}_{Tib}^{STL\to H}$: after this step they were in the same relative position as they were in the STL configuration, but the reference frame of the tibia was coincindent with the global. We then computed the transformation between the current talus position and the desired one, which was $\mathcal{R}_{Tal}^{t}$, and removed the translational part to guarantee that no penetrations happened generating the final transformation $\tilde{\mathbf{T}}^{H\to t}$. A sketch of the new kinematics is shown in Figure 5.2.8.

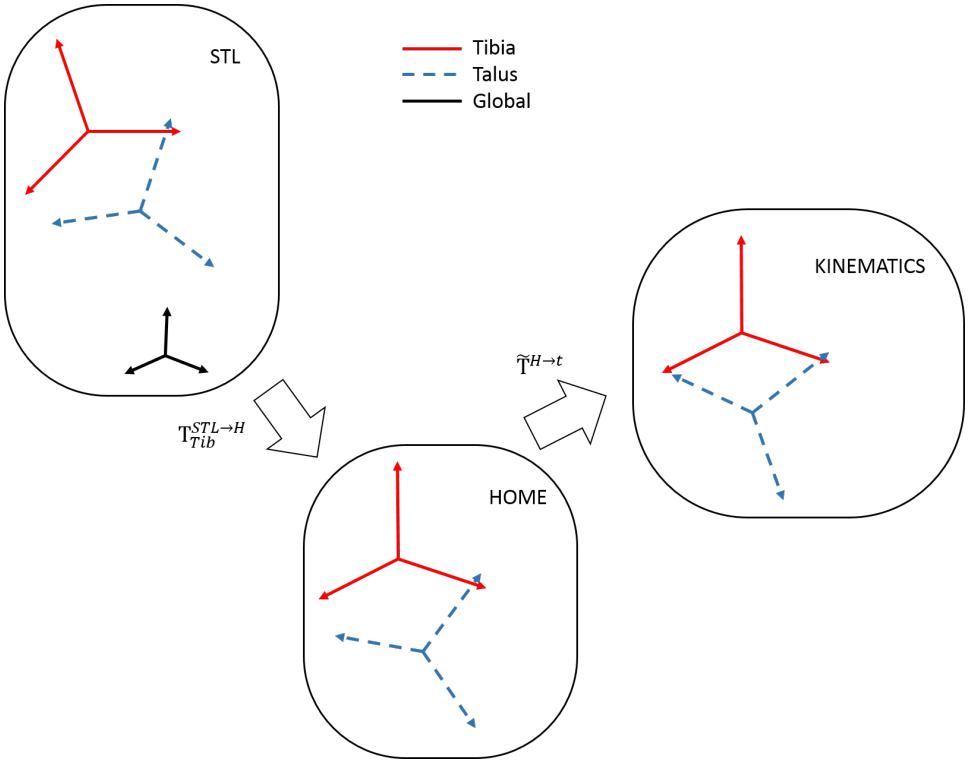

Figure 5.2.8: Modified kinematics of the system. The motion of the talus with respect to the tibia is expressed as a transformation from the HOME configuration. The movement of the talus is purely rotational.

With the rotational kinematics of the gait being defined, the next step was the definition of the applied force. Using an anatomic atlas we identified the attachment points of the muscles used in the OpenSim simulation and defined in MAT-

LAB their lines of action . At each time point, after the contact region was computed as in Chapter 4, the muscle lines of action were also updated to reflect the physiological orientation. Contact simulations were performed using the EDEM algorithm explained in Chapter 3. At each time step, after the talus was first oriented through the imposition of the rotational kinematics, the position of the talus was refined by applying the displacement computed at the previous time point. Young's modulus, Poisson's ratio and maximum cartilage thickness are taken as 10.35 MPa [85], 0.42 [7] and 3.5 mm [161] respectively.

5.3 Results

Experimental measures of the contact pressure varied with time, depending on the phase of stance, but were consistent across the trials. After a small plateau in correspondence of the heel strike, 0.59 ± 0.036 MPa, the peak values raised steadily until the end of the simulated stance with final values of 0.69 ± 0.02 MPa. The computational model tended to overestimate the contact pressure, with similarities and difference to the experimental one. The overall trend resembles that of the applied muscle forces: after a local peak in correspondence of the heel strike the pressure raised constantly until the maximum reached at the toe off, and then decreased until the end of the stance. As top of Figure 5.3.1 shows, the variability in the peak pressure from both experimental measures and computational model is limited with respect to the attained values. Figure 5.3.1 bottom, however, shows that the two fields of pressure are separated by one order of magnitude.

The experimental pressure measures show multi-centric patterns of contact during simulated stance, consistent across trials. The main centre, loaded during the entire stance, is located on the lateral part of the talus. The second is located anteriorly with respect to the first one, and is mostly active during the midstance. The third centre appears on the medial part of the joint: depending on the trial the contact pressure can be higher or lower, but essentially it is in contact during most of stance. The computational model predicts this multi-centric patterns: it is able

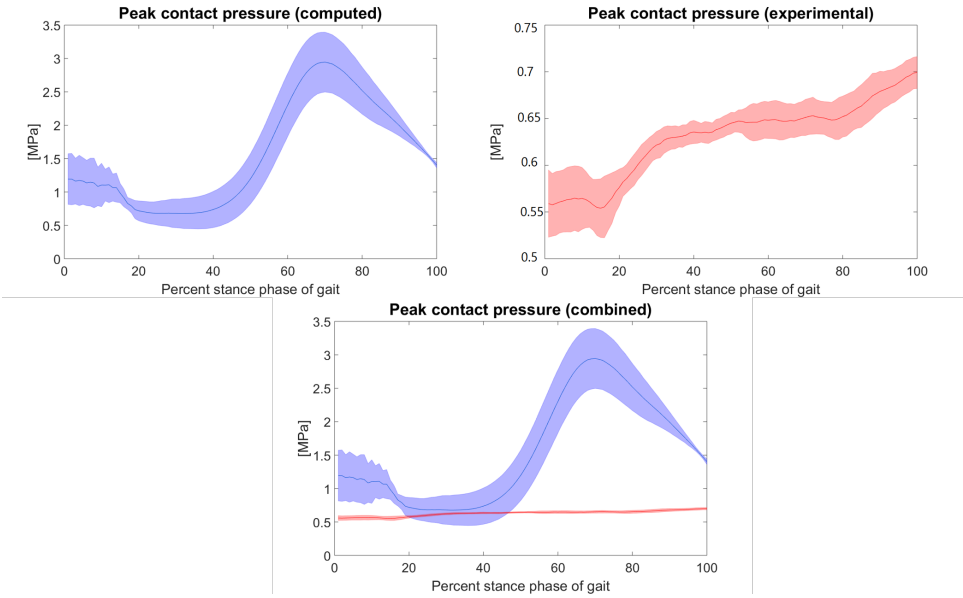

Figure 5.3.1: Plots of peak pressure from experimental and computational. Two different scales are used in the top plots, the same scale is used in the bottom one.

to identify that the first centre is the most loaded region, and most of the activity of the third centre, but it is not capable of predicting the second one. The pressure distribution at selected instant of time from one trial is shown in Figure 5.3.2. The differences in range between computational and experimental values did not allow for the use of the same scale in Figure 5.3.2.

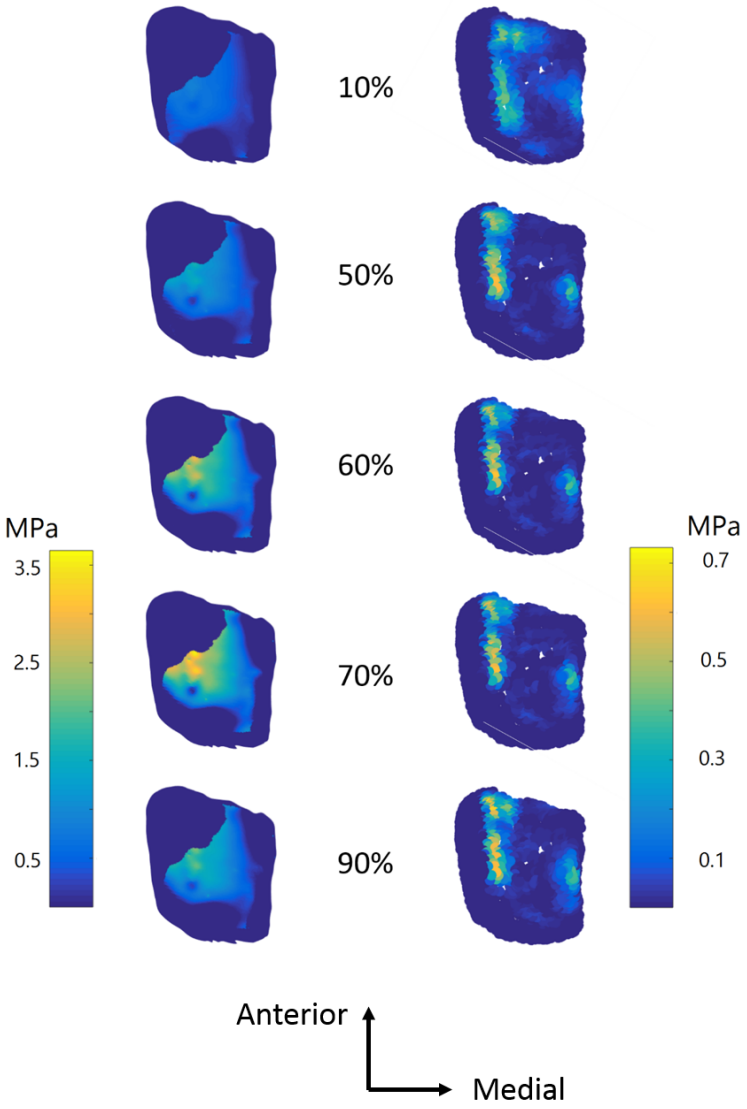

Figure 5.3.2: Pressure distribution at selected instants of time: results from EDEM are on left, experimental measures are on the right.

The experimentally measured contact region occupies most of the articular surface of the talus, with the three centres clearly active during midstance. According to the computational model the joint is initially loaded in its central part, with the maximum being located towards the lateral side and a branch towards the medial

part which can be identified as the third centre. As time progresses, both experimental measures and computational predictions show a greater involvement of the anterior part of the joint.

5.4 Discussion

The current study has presented results on the intra-articular contact pressure distribution in cadaveric ankle joints during simulated gait activities. The specimen was placed in a cadaveric gait simulator actuated using as input kinematics and muscle forces within physiological ranges, despite the need to downscale by 50% the muscle forces in order to preserve the structural integrity of the specimen.

Curves of peak contact pressure are consistent along trials, and share similarities over time. Two main differences are present: EDEM results predict the contact pressure to decrease after the heel strike, driven by the decrease in muscle forces. Experimental measures however show a continuous growing trend. Various modelling assumption can play a role in this. Although in the experiment the pressure sensitive film was located at the interface between talus and tibia, the specimen was formed of an entire foot and a portion of the tibia. Several joint can be identified in the foot and they all contribute to holding the applied load [57, 246]. These joints were not present in the computational model, where the only load bearing joint was the tibiotalar joint. Furthermore, passive structures such as ligament and bones absorb part of the applied load, the former stretching and the latter deforming during gait activities. Finally, the moving platform placed underneath the cadaveric specimen provided an active force on the foot. We speculate that the combination of these factors resulted in an effective force applied to the tibiotalar joint which was different in shape and smaller in magnitude from the one we actually used in the computational model. Dynamic investigations of joint contact pressure in dissected cadaveric ankles, a condition which more closely resembles the one we simulated here, have shown peak pressure with behaviour similar to the one we predicted here [224]. Further investigation and refinement of the model will be needed to address this point.

The computational model was able to predict the activation of areas in good agreement with the measured ones. Validated FE studies have reported the lateral sector of the ankle joint to be the most loaded during gait activities [8], and various authors [129, 224, 230] have confirmed it through *in-vitro* gait simulations. The computational model correctly identifies this region as the most loaded, and the predicted peak values fall within the physiological ranges. The same can be said for the loading in the medial part of the joint [224, 242]. Despite reports in the literature exist on the loading of the anterior part of the joint [129, 230, 242], which is also observed in the experimental study, the computational model did not predict the activation of the anterior part of the joint, especially in its lateral compartment. The main reason for this is the procedure followed for the estimation of the contact domain, which is based on the computation of the distance between tibia and talus. The geometries of the articulating bones are such that in that particular region the estimated cartilage thickness falls often behind the threshold value, set at 3.5 mm. The procedure we adopted to modify the kinematics and discard the translational part of the input has certainly played a role in the estimation of the thickness, but it was required to avoid undesired intersections.

To conclude, this chapter has compared the outcomes of the EDEM against experimentally collected pressure data from cadaveric specimen. EDEM has proven able to predict patterns of pressure in reasonable agreement with the experimental data, and to identify the contact of certain areas during the stance. It is however to remark that the match is far from being perfect and further work, on both experimental and computational sides, is needed to improve the predictions.

6

Viscoelastic model of the ankle joint

6.1 Introduction

The remarkable material properties of the articular cartilage are due to its complex inner structure, which comprises water, collagen fibrils and proteoglycan macromolecules [168]. The viscoelastic properties of articular cartilage can be divided into two main categories, called flow-independent and flow-dependent viscoelasticity. The first mechanism is caused by the intrinsic viscoelastic behaviour of the collagen fibres [102], while the second appears because of the frictional drag encountered by the water when it flows in and out the collagen matrix [13, 168].

The most evident viscoelastic properties the cartilage exhibits are the creep and stress-relaxation. The application of a constant load on the cartilage causes its deformation to increases with time until an equilibrium value is reached. Stress-relaxation is the dual behaviour of creep, and is concerned with the gradual reduc-

tion of the stress in the material when subject to a constant deformation [77]. The velocity of such decrease is characterised by the relaxation time of the material.

Experimental studies have determined that the articular cartilage exhibits viscoelastic behaviour in a variety of different scenarios, ranging from uniaxial tension [256], compression [11], either confined or unconfined, shear [102] and indentation [121]. Also it has been shown that the cartilage exhibits a spectrum of relaxation times [100]. Also, its stiffness has been identified as frequency dependent [186, 227]

Over the years, several constitutive models have been proposed [33, 101, 166], and the resulting computational model were able to describe indentation [190], confined [226] and unconfined [145] compression.

To the author's knowledge, however, this large variety of constitutive relationship has not been used in the development of computational joint contact models which include the viscoelastic properties of the articular cartilage. The aim of this chapter is to further contribute to the theory of the Extended discrete element method (EDEM) by presenting a reformulation capable of describing the viscoelastic behaviour of the cartilage, and to test its performance in a subject-specific model of the ankle joint subject to simple loads.

6.1.1 1D VISCOELASTICITY

Springs model purely elastic behaviour, while dashpots model purely viscous behaviour. Intermediate behaviours can be described by combinations of these two elementary constituents.

The Kelvin-Voigt rheological model of viscoelasticity is comprised of a spring, characterised by a stiffness value k, put in parallel to a dashpot of damping constant η. The elastic force σ_e generated by the spring is proportional to its deformation ε as

$$\sigma_e = k\varepsilon, \tag{6.1}$$

while the viscous damper exerts a force σ_v proportional to its velocity of deforma-

tion $\dot{\varepsilon}$:

$$\sigma_v = \eta\dot{\varepsilon}. \tag{6.2}$$

Throughout this chapter we will denote with a superscript dot the derivative with respect to time, i.e. $\dot{\varepsilon} = \frac{d\varepsilon}{dt}$. Let the viscoelastic element be constrained at one extremity, and loaded with an applied force σ at the other one, as shown in Figure 6.1.1.

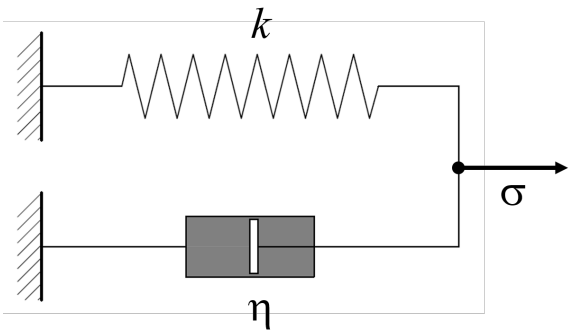

Figure 6.1.1: The Kelvin-Voigt model for viscoelasticity. The springs is characterised by the elastic constant k, the dashpot by the damping parameter η. The applied external force is σ.

The elastic and viscous elements both contributes to the equilibrium, which means

$$\sigma = \sigma_e + \sigma_v. \tag{6.3}$$

Using Eq. 6.1 and 6.2 the equilibrium condition can be rewritten as

$$\eta\dot{\varepsilon} + k\varepsilon = \sigma \tag{6.4}$$

or in its canonical form

$$\dot{\varepsilon} + \frac{1}{\tau}\varepsilon = \frac{\sigma}{\eta}, \tag{6.5}$$

where we introduce the relaxation time $\tau = \frac{\eta}{k}$, a parameter which describes how "fast" the system is. The solution to Eq. 6.5 can be found analytically by means of the integrating factor method [112], which allows the introduction of exact differential making the solution easier. To this end, introduce the integrating factor for Eq. 6.5 as

$$M(t) = e^{\int_{t_0}^{t} \frac{1}{\tau} ds} \tag{6.6}$$

and multiply by it both sides of the equation to obtain

$$e^{\int_{t_0}^{t} \frac{1}{\tau} ds}(\dot{\varepsilon} + \frac{1}{\tau}\varepsilon) = e^{\int_{t_0}^{t} \frac{1}{\tau} ds}\frac{\sigma}{\eta}. \tag{6.7}$$

The use of the integrating factor makes the left hand side an exact differential:

$$\frac{d}{dt}(e^{\int_{t_0}^{t} \frac{1}{\tau} ds}\varepsilon) = e^{\int_{t_0}^{t} \frac{1}{\tau} ds}(\dot{\varepsilon} + \frac{1}{\tau}\varepsilon). \tag{6.8}$$

By integrating right and left hands one obtains

$$e^{\int_{t_0}^{t} \frac{1}{\tau} ds}\varepsilon = \int_{t_0}^{t} e^{\int_{t_0}^{s} \frac{1}{\tau} dw}\frac{\sigma}{\tau}\, ds + C \tag{6.9}$$

and finally the solution

$$\varepsilon = e^{-\int_{t_0}^{t} \frac{1}{\tau} ds}\int_{t_0}^{t} e^{\int_{t_0}^{s} \frac{1}{\tau} dw}\frac{\sigma}{\tau}\, ds + Ce^{-\int_{t_0}^{t} \frac{1}{\tau} ds}. \tag{6.10}$$

The initial conditions of Eq. 6.5 determine the value of the constant of integration C. Despite the existence of an analytical solution, depending on the nature of the applied load σ, Eq. 6.5 and Eq. 6.10 can require a numerical treatment: throughout this chapter we will make use of 2^{nd} order Runge-Kutta method [34].

In what follows, some features of the solution of Eq. 6.5 for different loads and values of the relaxation time will be discuss qualitatively. The origin of the reference frame is set in the point where the free extremity of the system is located at $t = t_0$.

The first row of Fig. 6.1.2 shows the response of a Kelvin-Voigt material when

subject to a step force. After an initial rest phase, at $t = t_1$ the force activates the system and causes the free extremity to move. The promptness of the response depends on the relaxation time: the dark blue system shows the fastest response and is able to reach an equilibrium position before the loads goes to zero at $t = t_2$, whereas slower systems are still being displaced towards their equilibrium configuration. Higher values of $|t_2 - t_1|$ would allow also the slower systems to reach the equilibrium. For $t > t_2$ the systems move back towards their original position, each of them according to their relaxation time. The same core features are shown also when the system is subject to other types of loadings.

As discussed in Chapter 3, the elastic solution follows instantaneously the applied load. Such behaviour is not observed in viscoelastic systems which exhibit a delay in their response. However, as Eq. 6.5 shows, elastic and viscoelastic systems have the same solution at equilibrium, which is when $\dot{\varepsilon} = 0$.

6.2 Viscoelasticity and Extended Discrete Element Method

This section, which is the core of this chapter, will presents a novel reformulation of EDEM able to include the viscoelastic behaviour of cartilage within the modelling framework. First, the equilibrium equation for viscoelastic DEM will be derived, and then modified into the EDEM equation to allow for tracking of the motion of the contacting bodies. The notation and terminology will be the same as in Section 3.2.

Introduce a Cartesian frame $\{O; \mathbf{e}_1, \mathbf{e}_2, \mathbf{e}_3\}$ and two bodies $\mathcal{F}$ and $\mathcal{M}$, the former stationary in space and the latter able to move. Let them be in contact over a region $S \subset \mathcal{M}$, whose generic point is denoted as $\mathbf{r}$, and denote the position vector of the centroid of $\mathcal{M}$ with $\mathbf{r}_G$. For each point on S we introduce a viscoelastic load bearing element, parallel to the normal vector $\mathbf{n}_\mathbf{r}$, constituted by a spring and a dashpot in parallel. The *particulariser* operator $\mathbf{B}_\mathbf{r}$ is defined as in Section 3.2. Equilibrium considerations dictate to define two different operators for the computation of the stress. The first one, $\mathbf{D}_\mathbf{r}$, computes the part of stress induced by the

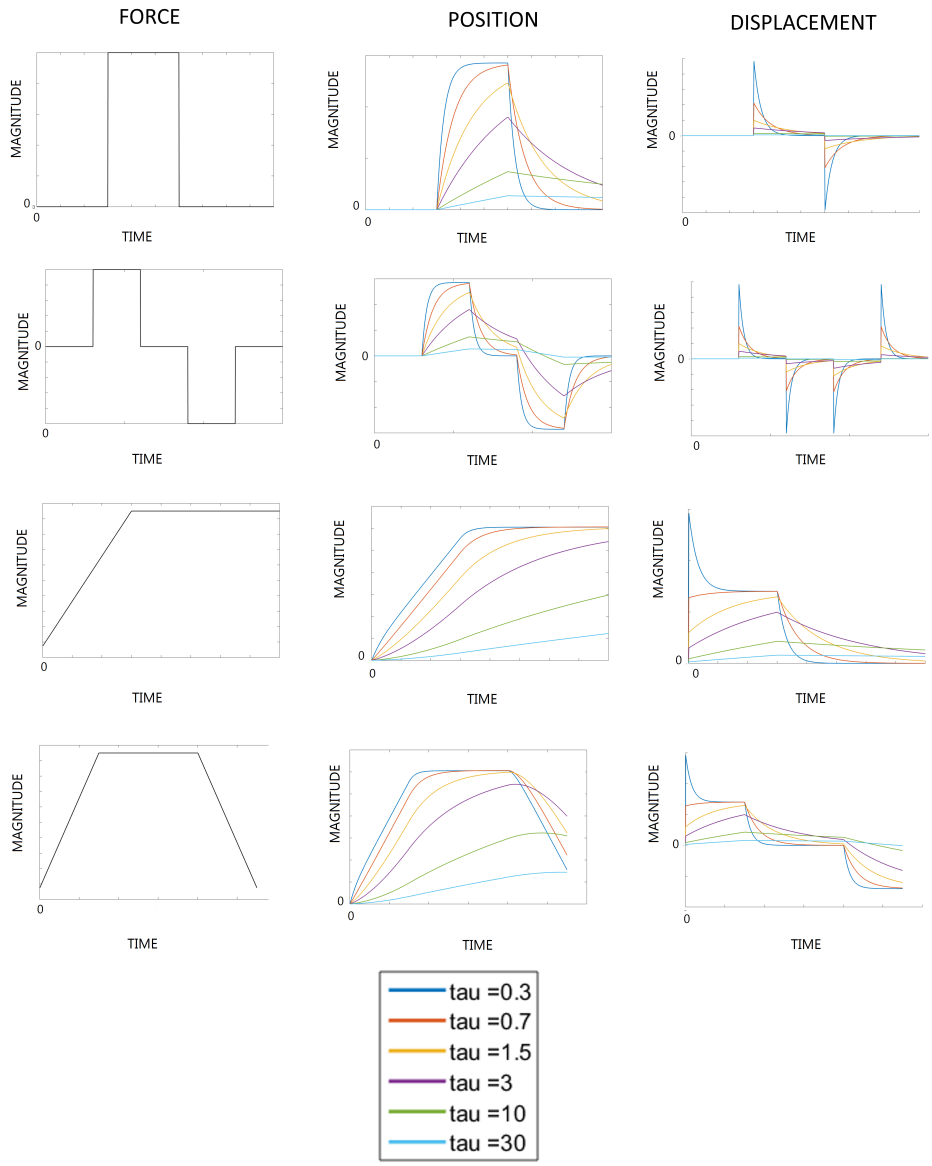

Figure 6.1.2: Behaviour of Kelvin-Voigt viscoelastic materials under different loads.

displacement of the spring and is defined as

$$\mathbf{D}_\mathbf{r} = k_d \mathbf{n}_\mathbf{r} \otimes \mathbf{n}_\mathbf{r} + k_s(\mathbf{I}_{3\times 3} - \mathbf{n}_\mathbf{r} \otimes \mathbf{n}_\mathbf{r}), \tag{6.11}$$

where k_d, k_s are the normal and tangent stiffness respectively, and $\mathbf{n}_\mathbf{r} \otimes \mathbf{n}_\mathbf{r}$ is the projector in the direction of $\mathbf{n}_\mathbf{r}$. As in three-dimensional elasticity [217], the part of stress induced by the velocity of the dashpot has the same structure:

$$\mathbf{V}_\mathbf{r} = \eta_d \mathbf{n}_\mathbf{r} \otimes \mathbf{n}_\mathbf{r} + \eta_s(\mathbf{I}_{3\times 3} - \mathbf{n}_\mathbf{r} \otimes \mathbf{n}_\mathbf{r}), \tag{6.12}$$

where η_d and η_s, the normal and tangent damping, and are related to the stiffness by the relaxation time τ as

$$\begin{aligned} \eta_d &= \tau k_d \\ \eta_s &= \tau k_s. \end{aligned} \tag{6.13}$$

The total stress in the viscoelastic element is then computed using the generalised displacement $\mathbf{u}$ of $\mathcal{M}$ as follows:

$$\sigma_\mathbf{r} = \sigma_\mathbf{r}^e + \sigma_\mathbf{r}^v = \mathbf{D}_\mathbf{r}\mathbf{B}_\mathbf{r}\mathbf{u} + \mathbf{V}_\mathbf{r}\mathbf{B}_\mathbf{r}\dot{\mathbf{u}}. \tag{6.14}$$

Proceeding as in Section 3.2 the total energy of the system under an applied load $\mathbf{T}$ can be computed as

$$\begin{aligned} \mathcal{E}(\mathbf{u}, \dot{\mathbf{u}}; \mathbf{T}) &= \frac{1}{2} \iint_S \mathbf{B}_\mathbf{r}^\mathrm{T} \mathbf{D}_\mathbf{r} \mathbf{B}_\mathbf{r} \, dS \mathbf{u} \cdot \mathbf{u} + \iint_S \mathbf{B}_\mathbf{r}^\mathrm{T} \mathbf{V}_\mathbf{r} \mathbf{B}_\mathbf{r} \, dS \dot{\mathbf{u}} \cdot \mathbf{u} - \mathbf{u} \cdot \mathbf{T} \\ &= \frac{1}{2} \mathbf{K}\mathbf{u} \cdot \mathbf{u} + \mathbf{H}\dot{\mathbf{u}} \cdot \mathbf{u} - \mathbf{u} \cdot \mathbf{T}. \end{aligned} \tag{6.15}$$

The matrices

$$\begin{aligned} \mathbf{K} &= \iint_S \mathbf{B}_\mathbf{r}^\mathrm{T} \mathbf{D}_\mathbf{r} \mathbf{B}_\mathbf{r} \, dS \\ \mathbf{H} &= \iint_S \mathbf{B}_\mathbf{r}^\mathrm{T} \mathbf{V}_\mathbf{r} \mathbf{B}_\mathbf{r} \, dS \end{aligned} \tag{6.16}$$

are the elastic and viscous stiffness of the system, respectively. The elastic matrix is responsible for storing energy into the system, whereas the viscous is responsible for the dissipation of the energy. Minimisation of the total energy leads to the global equilibrium equation

$$\mathbf{H}\dot{\mathbf{u}} + \mathbf{K}\mathbf{u} = \mathbf{T}. \tag{6.17}$$

This formulation must be extended to allow for tracking the motion of the contact bodies: as in Section 3.3 this is done by including the *push-back* force in the constitutive relationship of the viscoelastic elements. After integration over the contact area an minimisation of the energy this yields to the incremental viscoelastic equation for EDEM

$$\mathbf{H}\dot{\mathbf{u}} + \mathbf{K}\mathbf{u} = \mathbf{T} - \mathbf{p}. \tag{6.18}$$

Eq. 6.18 is solved at each time point t using the 2^{nd} order Runge-Kutta algorithm, which produces the displacement and the velocity of the rigid body $\mathcal{M}$, needed for the computation of the stress. As in elastic EDEM, stretched elements are removed from the computational domain and the solution sought until all the elements are in a non tensile state.

6.3 Application to 3D problems

In this section the presented reformulation of EDEM for viscoelastic problems is implemented with the aim of investigating the contact pressure in a viscoelastic ankle model. Rather than the development of a realistic viscoelastic ankle model,

the scope of this study is the assessment of the performances of the viscoelastic model in a 3D scenario.

6.3.1 Methods

The same dataset of Chapter 4 was used for the development of the viscoelastic model. MRI images of the lower limbs of a juvenile subject (16 years, 68 Kg, 160 cm) were collected at the Istituto Giannina Gaslini (Genoa, Italy) and segmented to identify the bone geometries. The articular surface of talus and tibia was identified from the segmented geometries, which were then meshed. A total of 2974 Kelvin-Voigt contact elements was posed on the articular surface of the talus. Ligaments were not included in the model.

We simulated a simple loading scenario, consisting in a 5 s ramp increasing from 200 N to 1800 N, followed by 10 s of constant load and then a 5 s descending ramp from 1800 N to 200 N. In this simulation the ankle was kept in a neutral position and the relative orientation of talus and tibia was not modified. The applied force acted on the talus and pushed in the superior and posteromedial directions.

To test the behaviour of the viscoelastic model we selected three different values of relaxation time, one obtained from the literature and two increasingly larger: $\tau_1 = 1.4$ s [67], $\tau_2 = 7$ s, $\tau_3 = 14$ s.

6.3.2 Results

Results from the simulation of the ramp scenario are shown in Figure 6.3.1 as norm of the distance of the talus from its original position and norm of the incremental displacement. During the first phase the talus is displaced towards the tibia. The actual magnitude of the displacement of the talus depends on the magnitude of the damping parameter, which is directly proportional to the relaxation time. It is evident that for $\tau = 1.4$ the system is responsive enough to reach a plateau at the end of the constant loading phase, whereas larger time constants caused a slower response. As the lower image of Figure 6.3.1 shows, the computed displacement

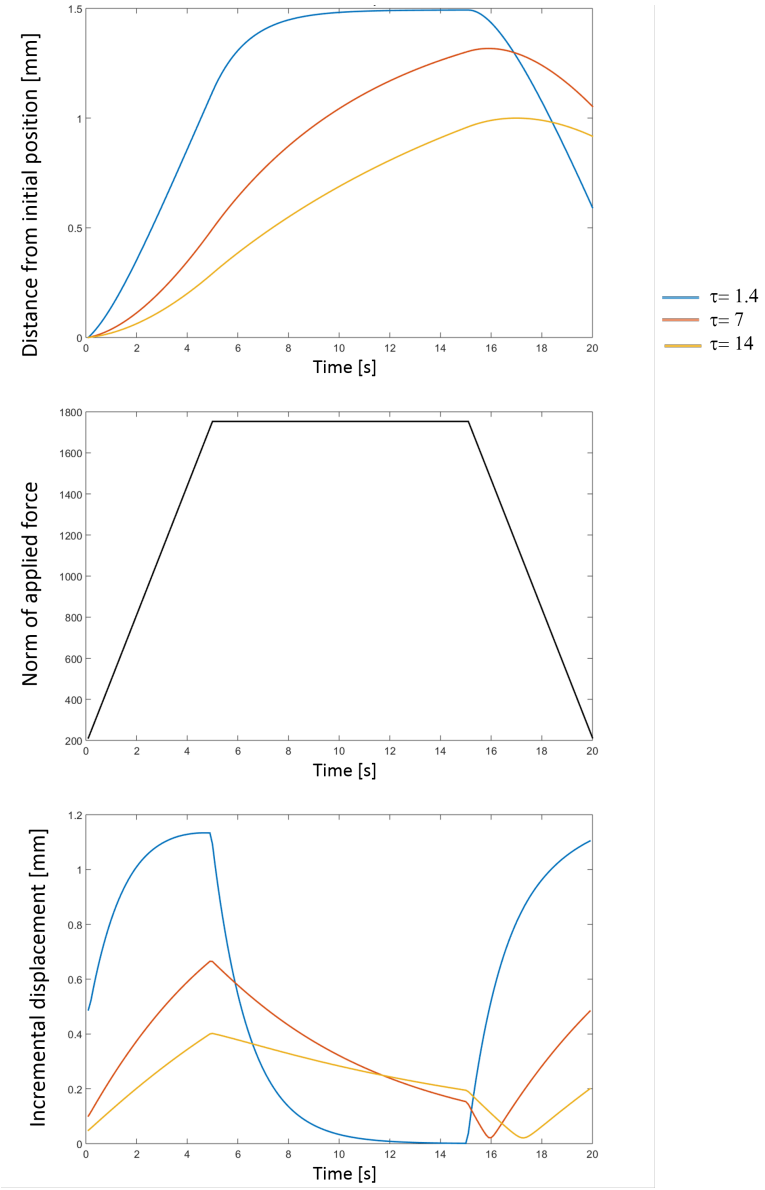

Figure 6.3.1: Response of the viscoelastic ankle model to ramp loading.

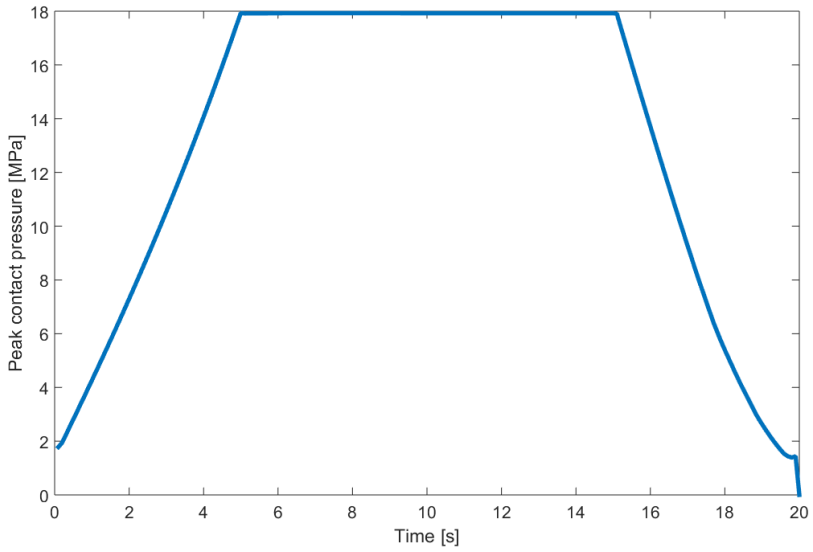

Figure 6.3.2: Peak contact pressure as predicted by the viscoelastic model. The relaxation time is set to 1.4 s, but the same behaviour is obtained for different relaxation times.

is the time derivative of the position.

Despite the presence of the viscoelastic elements the plot of the peak contact pressure shows exactly the same behaviour of the applied force, with a maximum value of 18 MPa (Figure 6.3.2).

As Figure 6.3.3 the most loaded region of the joint is its posterior part and, since the relative orientation of tibia and talus is not modified during the loading process, this holds for the entire simulation.

6.4 Discussion

In this chapter we have shown how viscoelastic phenomena can be included within the framework of EDEM, and we have presented an ankle model where the articular cartilage was modelled using Kelvin-Voigt viscoelastic element. The model, not

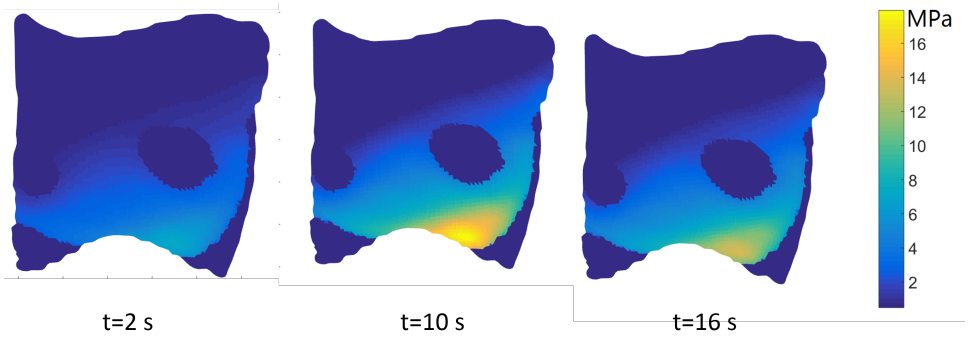

Figure 6.3.3: Contact pressure distribution at 2, 10 and 16 s. The relaxation time is set to 1.4 s, but the same pressure distribution is obtained for different relaxation times.

including ligaments, was tested with a ramp force to evaluate the performance of the viscoelastic solver. In terms of displacement, the solution shows the creep behaviour characteristic of viscoelastic materials: the application of the force caused to talus to be displaced towards the tibia, but the Kelvin-Voigt elements introduced a delay in the response of the system. As anticipated from the theory, the introduced delay grew larger with the increasing of the relaxation time, which is a measure of the slowness of the system. For the smallest relaxation time, τ =1.4 s, the system was able to reach an equilibrium configuration before the decrease of the applied force drove it backwards towards its original position, whereas for higher relaxation time the strength of the viscous part of the response did not allow the talus to reach an equilibrium configuration. Computed displacement is the time derivative of the position. Figure 6.3.1 bottom shows an apparent lack of derivability of the displacement for instants of time following the decrease of the applied force. This is however not true, as the graph shows the norm of the displacement vector, whose components are negative when the force is decreasing.

Despite the clear viscoelastic effects shown by displacement and position, the behaviour of the peak contact pressure is the same as it would be predicted by purely elastic theories. This can be explained by recurring to the definition of stress in viscoelastic EDEM. The pressure on a point $\mathbf{r}$ is the projection along the normal direction $\mathbf{n_r}$ of the stress $\sigma_\mathbf{r}$, which is composed of an elastic part proportional to

the displacement, a viscous part proportional to the velocity and the *push-back* force. The *push-back* force and the sum of these two last components, weighted according to the elastic stiffness and viscous damping, is equal to the externally applied force. This explains why viscoelastic effects are not visible in the pressure distribution. Peak values of pressure are higher than those predicted by simulation of standing in Chapter 4 because of the higher magnitude of the applied load and the absence of ligaments.

The presented description, although being able to catch the basic viscoelastic behaviour of the articular cartilage, is based on a simplified constitutive relationship. More general constitutive relationships based on higher order derivatives of both stress and strain [233] or convolution integrals [202] can describe a wider range of phenomena but require more parameters to be determined experimentally. The developed viscoelastic cartilage model shows potential for being incorporated within multibody systems for the aim of multiscale body-organ integration and, therefore, it is to be kept at a reasonable level of complexity. It is however to consider that the gait is a relatively short activity during which the cartilage does not have time to fully express the complexity of its behaviour. Further studies will determine the optimal constitutive relationship which guarantees a compromise between the accuracy of the response and the computational demands.

Despite its resistance, the articular cartilage is particularly sensitive to high frequency loads, such as those generated during impacts, which can induce damages to its structure and carry its degeneration [**?**]. As [10] has shown, 1D linearly viscoelastic models (i.e. Kelvin-Voigt, Maxwell and standard solid) can easily be adopted to treat impulsive forces. The viscoelastic contact model proposed in this chapter makes no exception, provided that the method is further extended the include the non-negligible inertial effects.

The addition of inertial terms to the equilibrium equation of EDEM would favour the integration of the contact model within multibody dynamics systems. The use of viscoelastic contact models in conjunction with musculoskeletal models would lead to predictions of the relative motion of the bones which differ from the one computed using purely elastic contact models and, since the relative position of

the articulating bones is crucial for the determination of the joint centre and muscle lever arms, this would ultimately affect the determination of the muscle forces and the total joint load [109, 141].

To conclude, in this chapter we have shown that it is possible to integrate the viscoelastic behaviour of the articular cartilage within the framework of EDEM. The proposed methodology was able to describe the creep behaviour of the articular cartilage and shows promising potential for integration with multibody systems.

7

Conclusions and future work

The multiscale modelling approach has gained popularity among researchers of the musculoskeletal system in view of its capability to describe musculoskeletal system across different spatial and temporal levels. The full integration of all the scales of the musculoskeletal shows promising potential for applications to clinical problems such as the prediction of the risk of fracture and the progress of osteoarthritis. However, developing such a multiscale model of the musculoskeletal system poses computational challenges due to its requirements of intensive computing resources.

The aim of the work was the development of computationally efficient methodologies for the computational estimation of the contact pressure in the human joints, as integrated part of multiscale musculoskeletal system modelling and simulation. To this end, the primary objective of this dissertation was to develop a computationally efficient modelling framework for generic contact mechanics, apply it

for ankle contact modelling driven by highly accurate, subject-specific kinematics of human motion, and validated its framework with experimental data. These objectives were achieved by carrying out several studies through Chapters 3- 6.

The static theory of the Discrete element method (DEM) for the modelling of contact mechanics has been presented in Chapter 3 and, after the exposition of its limitations, the Extended discrete element method (EDEM) for the treatment of joint contact problem involving time-dependent phenomena, in particular, the joint contact behaviour during motion of human, has been introduced. The two methods have been implemented and their outputs compared in Chapter 4, where they were used to simulate joint contact during stance on subject specific geometries. Input data from subject-specific musculoskeletal models were integrated within the EDEM model to guarantee, at each time point, that the rotational kinematics of the contact model was coherent with the *in-vivo* kinematics of the subject. Results have shown that the static methods tended to underestimate the joint contact region, whereas EDEM predicted the activities of larger parts of the joints. Predictions from EDEM were evaluated in good agreement with the existing literature on ankle joint contact. The sensitivity analysis on EDEM inputs has shown that the parameter which greatly influences the output is the estimated cartilage length.

In Chapter 5 the cadaveric foot gait simulator used for the collection of kinematic and pressure data during simulated stance was presented. An EDEM model has been developed which used the measured kinematics to drive the angular configuration of the contact model. The EDEM model was used to predict the contact pressure during stance, and its predictions compared with the collected data. Despite some discrepancies in the prediction of peak values, the model was able to identify the activation of the same regions measured as active by the pressure sensor. However, it failed in identifying the activation of the antero-lateral compartment of the joints.

Chapter 6 has shown that EDEM can be further extended to include viscoelastic constitutive relationships. Simulations of simplified loading scenarios proved that the extension is capable of describing the characteristic creep behaviour shown by

articular cartilage, and to predict how the mechanical response of the tissue varies with variation of the relaxation time.

7.1 Contributions

The main contributions of this work are outlined here.

A methodology for the fast treatment of time dependent joint contact problems has been developed. The details of the theory behind the extension have been extensively discussed. To the authors knowledge few time dependent contact models exist in the literature, none of them applied to the ankle joint, and details on their formulation are usually not provided.

An optimised code for subject specific modelling of the human joint has been developed and tested, and will soon be released on GitHub (`https://github.org`), together with documentation, user manual and examples, to foster collaborations with researcher within the joint modelling community.

The use of dynamic data with the purpose of validation of computational contact models is new in the literature regarding contact mechanics and this study has shown that, despite minor discrepancies, the EDEM is able to predict the contact pressure distribution in cadaveric joints during simulated gait.

7.2 Limitations

The proposed methodology certainly lacks several features. The most important are listed below.

At each time point of the simulation the maximal contact region is estimated *ex-novo* using the location of the contact bodies, and then shrunk to its final value. An additive contact detection algorithm which allows the recruitment of contact springs within the simulation of a given time point would better reflect the nature of the contact between real bodies, and strengthen the dependence of the contact area on the applied load.

The articular cartilage has been modelled as an elastic material, whose constitutive relationship was based on Hooke's law and, implicitly, the assumption of small deformation of the contact springs. Although appropriate for the simulation of most of the daily activities, such hypothesis can be relaxed to allow for large deformations of the cartilage layer by using a nonlinear constitutive relationship.

Similar considerations can be made on the viscoelastic modelling. We adopted a simple Kelvin-Voigt model, able to depict the creep behaviour of the cartilage, but less effective in describing more complex properties of the cartilage such as the fluid-matrix interaction.

The analysis of the contact patterns during the gait cycle has been performed on a single subject in Chapter 4 and on a single specimen in Chapter 5. The use of a small cohort such as this does not permit a thorough investigation of the sensitivity of the model to certain input parameters such as the bones geometry or the cartilage thickness, which could vary widely according to the age, gender, degree of joint degeneration and other characteristics of the subject. Extending the study to larger datasets would give the possibility to test the model and assess its sensitivity to a variety of input data.

7.3 Future directions

One possible theoretical framework behind the use of general nonlinear constitutive relationship in springs based contact models has been presented in [241], and logarithmic constitutive relationships have appeared in [22, 93]. Future developments will include the use of nonlinear spring models. Ateshian and colleagues has shown that an exponential stress-strain relationship is appropriate to describe the behaviour of compressed cartilage subject to large deformations [13]. Exponential functions, however, are not suitable for numerical implementation: to this end a Taylor expansion can be performed, leading to a polynomial equilibrium equation which can be solved via the Newton-Raphson method. The iterative criterion to decide whether a spring is to be kept or removed from the computational domain does not require to be modified. Nonlinear spring models de-

scribe the behaviour of articular cartilage more accurately than linear model, but require the determination of a larger number of parameters. When not available in the literature, the parameters of the nonlinear model can be determined by means of optimisation techniques and parameters fitting of stress-strain curves obtained from compression tests of the articular cartilage. With respect to viscoelasticity, generic Boltzmann elements are able to cover a wider spectrum of viscoelastic effect than pure Maxwell or Kelvin-Voigt elements can. This modelling choice, however, could introduce further problems in the determination of the parameters. Fractional derivatives viscoelasticity [151], although still under development, is characterised by a limited number of parameters but nonetheless can model a wide variety of viscoelastic effects and represents a promising direction of investigation.

As mentioned earlier, the actual contact area is estimated through successive shrinking of the maximal estimate. Future extensions of this research will modify the contact detection algorithm by including an additive refinement within the computations at each time step. Related to this aspect, the maximal contact are is currently determined using a single layer of contact springs, whereas in the joints two layer of cartilage are engaged in contact. Future studies will investigate the level of similarities in the EDEM predictions of contact patterns when these two different modelling strategies are adopted.

The sensitivity study in Chapter 4 has shown that EDEM outputs are sensitive to the springs' length threshold which, after the estimation of the cartilage thickness, contributes to the definition of the active contact area. The cartilage thickness is estimated through projection of the normal vectors to the surface of the talus mesh towards the tibia mesh, and can therefore be influenced by the quality of the medical images and of the segmentation. Poorly segmented images are likely to produce irregular meshes, whose scattered normal vectors lead to a degraded the quality of the solution. Similarly, the quality of the segmentation affects also the determination of the joint axes which are fundamental for the determination of forces and kinematics during musculoskeletal simulations [95] which provide the inputs for the contact model. Future works will extend the sensitivity studies performed in this thesis, assessing how the quality of the segmentation of medical images can

induce errors which propagate throughout the pipeline, ultimately influencing the determination of the joint contact pressure.

The use of input data from a large population of individuals differentiated for genders, age, weight and other parameters would open the possibility to perform correlation studies. The objective of such studies is to investigate the correlation between outputs of the model and features of the dataset (i.e. correlation between weight and maximum contact pressure, age and extension of the contact area, maximum pressure and medical assessment of the status of the joint). This would then help to identify markers useful for preliminary diagnosis of osteoarthritis, or at the very least for an improved classification based on risk classes.

As the finite element (FE) method is currently considered the gold standard for the computational prediction of joint contact, the development of a FE model for comparison purposes would add further strength to the results computed using the EDEM methodology.

The low computational time required by EDEM makes it ideal for integration within multibody systems for the simultaneous prediction of joint kinematics, joint pressure and muscle forces. This would open perspectives with respect to the multiscale modelling of the musculoskeletal system in terms of body-organ levels coupling, making the coupling bidirectional and giving the possibility to investigate the effect that bone motion has on the determination of joint kinematics.

References

[1] CL Abraham, SA Maas, JA Weiss, BJ Ellis, CL Peters, and AE Anderson. A new discrete element analysis method for predicting hip joint contact stresses. *Journal of Biomechanics*, 46(6):1121–1127, 2013.

[2] M Akbar, F Farahmand, A Jafari, and MS Foumani. A detailed and validated three dimensional dynamic model of the patellofemoral joint. *Journal of Biomechanical Engineering*, 134(4):041005, 2012.

[3] T Alonso-Rasgado, D Jimenez-Cruz, and M Karski. 3-d computer modelling of malunited posterior malleolar fractures: effect of fragment size and offset on ankle stability, contact pressure and pattern. *Journal of Foot and Ankle Research*, 10(1):13, 2017.

[4] DG Altman. *Practical statistics for medical research*. CRC press, 1990.

[5] KN An, S Himeno, H Tsumura, T Kawai, and EYS Chao. Pressure distribution on articular surfaces: application to joint stability evaluation. *Journal of Biomechanics*, 23(10):1013–1020, 1990.

[6] AE Anderson, BJ Ellis, SA Maas, CL Peters, and JA Weiss. Validation of finite element predictions of cartilage contact pressure in the human hip joint. *Journal of Biomechanical Engineering*, 130(5):051008, 2008.

[7] DD Anderson, JK Goldsworthy, K Shivanna, NM Grosland, DR Pedersen, TP Thomas, Y Tochigi, JL Marsh, and TD Brown. Intra-articular contact stress distributions at the ankle throughout stance phase–patient-specific finite element analysis as a metric of degeneration propensity. *Biomechanics and Modeling in Mechanobiology*, 5(2-3):82, 2006.

[8] DD Anderson, Jane K Goldsworthy, W Li, MJ Rudert, Y Tochigi, and TD Brown. Physical validation of a patient-specific contact finite element model of the ankle. *Journal of Biomechanics*, 40(8):1662–1669, 2007.

[9] DD Anderson, KS Iyer, NA Segal, JA Lynch, and TD Brown. Implementation of discrete element analysis for subject-specific, population-wide investigations of habitual contact stress exposure. *Journal of applied biomechanics*, 26(2):215–223, 2010.

[10] II Argatov. Mathematical modeling of linear viscoelastic impact: Application to drop impact testing of articular cartilage. *Tribology International*, 63: 213–225, 2013.

[11] CG Armstrong and VC Mow. Variations in the intrinsic mechanical properties of human articular cartilage with age, degeneration, and water content. *The Journal of Bone and Joint Surgery. American volume*, 64(1):88–94, 1982.

[12] MH Arokoski, M Haara, HJ Helminen, and JP Arokoski. Physical function in men with and without hip osteoarthritis1. *Archives of Physical Medicine and Rehabilitation*, 85(4):574–581, 2004.

[13] GA Ateshian, WH Warden, JJ Kim, RP Grelsamer, and VC Mow. Finite deformation biphasic material properties of bovine articular cartilage from confined compression experiments. *Journal of Biomechanics*, 30(11-12): 1157–1164, 1997.

[14] GA Ateshian, BJ Ellis, and JA Weiss. Equivalence between short-time biphasic and incompressible elastic material responses. *Journal of Biomechanical Engineering*, 129(3):405–412, 2007.

[15] PM Aubin, EC Whittaker, and WR Ledoux. Foot bone kinematics at half and three quarters body weight: a robotic cadaveric simulation of stance phase. In *Advanced Robotics (ICAR), 2011 15th International Conference on*, pages 653–658. IEEE, 2011.

[16] JC Ausiello and RS Stafford. Trends in medication use for osteoarthritis treatment. *The Journal of Rheumatology*, 29(5):999–1005, 2002.

[17] KN Bachus, AL DeMarco, KT Judd, DS Horwitz, and DS Brodke. Measuring contact area, force, and pressure for bioengineering applications: using fuji film and tekscan systems. *Medical Engineering & Physics*, 28(5):483–488, 2006.

[18] KE Barbour, CG Helmick, M Boring, and TJ Brady. Vital signs: Prevalence of doctor-diagnosed arthritis and arthritis-attributable activity limitation-united states, 2013-2015. *MMWR. Morbidity and Mortality Weekly Report*, 66(9):246–253, 2017.

[19] CH Barnett and JR Napier. The axis of rotation at the ankle joint in man. its influence upon the form of the talus and the mobility of the fibula. *Journal of Anatomy*, 86(Pt 1):1, 1952.

[20] JR Baumgardner and PO Frederickson. Icosahedral discretization of the two-sphere. *SIAM Journal on Numerical Analysis*, 22(6):1107–1115, 1985.

[21] AJ Beaudoin, SM Fiore, WR Krause, and RS Adelaar. Effect of isolated talocalcaneal fusion on contact in the ankle and talonavicular joints. *Foot & Ankle*, 12(1):19–25, 1991.

[22] Y Bei and BJ Fregly. Multibody dynamic simulation of knee contact mechanics. *Medical Engineering & Physics*, 26(9):777–789, 2004.

[23] G Bergmann, G Deuretzbacher, M Heller, F Graichen, A Rohlmann, J Strauss, and GN Duda. Hip contact forces and gait patterns from routine activities. *Journal of Biomechanics*, 34(7):859–871, 2001.

[24] P Bhattacharya and M Viceconti. Multiscale modeling methods in biomechanics. *Wiley Interdisciplinary Reviews: Systems Biology and Medicine*, 9 (3):e1375, 2017.

[25] L Blankevoort, JH Kuiper, R Huiskes, and HJ Grootenboer. Articular contact in a three-dimensional model of the knee. *Journal of Biomechanics*, 24 (11):1019–1031, 1991.

[26] D Braess. *Finite elements: Theory, fast solvers, and applications in solid mechanics*. Cambridge University Press, 2007.

[27] RA Brand. Joint contact stress: a reasonable surrogate for biological processes? *The Iowa Orthopaedic Journal*, 25:82, 2005.

[28] KK Brock, SJ Hollister, LA Dawson, and JM Balter. Creating a four-dimensional model of the liver using finite element analysis. *Medical Physics*, 29(7):1403–1405, 2002.

[29] CL Brockett and GJ Chapman. Biomechanics of the ankle. *Orthopaedics and Trauma*, 30(3):232–238, 2016.

[30] CP Brown, TC Nguyen, HR Moody, RW Crawford, and A Oloyede. Assessment of common hyperelastic constitutive equations for describing normal and osteoarthritic articular cartilage. *Proceedings of the Institution*

of Mechanical Engineers, Part H: Journal of Engineering in Medicine, 223(6): 643–652, 2009.

[31] TD Brown and AM DiGioia. A contact-coupled finite element analysis of the natural adult hip. *Journal of Biomechanics*, 17(6):437–448, 1984.

[32] J Bruns and B Rosenbach. Pressure distribution at the ankle joint. *Clinical Biomechanics*, 5(3):153–161, 1990.

[33] PM Bursać, TW Obitz, SR Eisenberg, and D Stamenović. Confined and unconfined stress relaxation of cartilage: appropriateness of a transversely isotropic analysis. *Journal of Biomechanics*, 32(10):1125–1130, 1999.

[34] JC Butcher. The numerical analysis of ordinary differential equations: Runge-kutta and general linear methods. 1987.

[35] JH Calhoun, F Li, BR Ledbetter, and SF Viegas. A comprehensive study of pressure distribution in the ankle joint with inversion and eversion. *Foot & Ankle International*, 15(3):125–133, 1994.

[36] V Carbone, R Fluit, P Pellikaan, MM Van Der Krogt, D Janssen, M Damsgaard, L Vigneron, T Feilkas, HFJM Koopman, and N Verdonschot. Tlem 2.0–a comprehensive musculoskeletal geometry dataset for subject-specific modeling of lower extremity. *Journal of Biomechanics*, 48(5):734–741, 2015.

[37] RE Carey, L Zheng, AK Aiyangar, CD Harner, and X Zhang. Subject-specific finite element modeling of the tibiofemoral joint based on ct, magnetic resonance imaging and dynamic stereo-radiography data in vivo. *Journal of Biomechanical Engineering*, 136(4):041004, 2014.

[38] MC Carson, ME Harrington, N Thompson, JJ O'Connor, and TN Theologis. Kinematic analysis of a multi-segment foot model for research and clinical applications: a repeatability analysis. *Journal of Biomechanics*, 34 (10):1299–1307, 2001.

[39] RF Chandler, CE Clauser, JT McConville, HM Reynolds, and John W Young. Investigation of inertial properties of the human body. Technical report, AIR FORCE AEROSPACE MEDICAL RESEARCH LAB WRIGHT-PATTERSON AFB OH, 1975.

[40] AGCM Chen, C Gupte, K Akhtar, P Smith, and J Cobb. The global economic cost of osteoarthritis: how the uk compares. *Arthritis*, 2012, 2012.

[41] A Chitsazan, G Rouhi, M Abbasi, S Pezeshki, and SAH Tavakoli. Assessment of stress distribution in ankle joint: simultaneous application of experimental and finite element methods. *International Journal of Experimental and Computational Biomechanics*, 3(1):45–61, 2015.

[42] PG Ciarlet. *Three-dimensional elasticity*, volume 20. Elsevier, 1988.

[43] P Cignoni, M Callieri, M Corsini, M Dellepiane, F Ganovelli, and G Ranzuglia. Meshlab: an open-source mesh processing tool. In *Eurographics Italian Chapter Conference*, volume 2008, pages 129–136, 2008.

[44] EA Clancy, EL Morin, and R Merletti. Sampling, noise-reduction and amplitude estimation issues in surface electromyography. *Journal of Electromyography and Kinesiology*, 12(1):1–16, 2002.

[45] SC Cobb, LL Tis, JT Johnson, MD Geil, FA McCarty, et al. The effect of low-mobile foot posture on multi-segment medial foot model gait kinematics. *Gait & Posture*, 30(3):334–339, 2009.

[46] BJ Cole and MM Malek. *Articular cartilage lesions: a practical guide to assessment and treatment*. Springer Science & Business Media, 2013.

[47] JJ Collins. The redundant nature of locomotor optimization laws. *Journal of Biomechanics*, 28(3):251–267, 1995.

[48] PG Conaghan, J Dickson, and RL Grant. Guidelines: care and management of osteoarthritis in adults: summary of nice guidance. *BMJ: British Medical Journal*, 336(7642):502, 2008.

[49] M Conconi and V Parenti Castelli. A sound and efficient measure of joint congruence. *Proceedings of the Institution of Mechanical Engineers, Part H: Journal of Engineering in Medicine*, 228(9):935–941, 2014.

[50] AF Cordero, HJFM Koopman, and FCT Van Der Helm. Use of pressure insoles to calculate the complete ground reaction forces. *Journal of Biomechanics*, 37(9):1427–1432, 2004.

[51] J Costa, J Peixoto, P Moreira, AP Souto, P Flores, and HM Lankarani. Influence of the hip joint modeling approaches on the kinematics of human gait. *Journal of Tribology*, 138(3):031201, 2016.

[52] A Courties, O Gualillo, F Berenbaum, and J Sellam. Metabolic stress-induced joint inflammation and osteoarthritis. *Osteoarthritis and Cartilage*, 23(11):1955–1965, 2015.

[53] RD Crowninshield and RA Brand. A physiologically based criterion of muscle force prediction in locomotion. *Journal of Biomechanics*, 14(11): 793–801, 1981.

[54] RD Crowninshield, RA Brand, and RC Johnston. The effects of walking velocity and age on hip kinematics and kinetics. *Clinical Orthopaedics and Related Research*, (132):140–144, 1978.

[55] SR Cummings, JL Kelsey, MC Nevitt, and KJ O'Dowd. Epidemiology of osteoporosis and osteoporotic fractures. *Epidemiologic Reviews*, 7(1):178–208, 1985.

[56] RB Davis III, S Ounpuu, D Tyburski, and JR Gage. A gait analysis data collection and reduction technique. *Human Movement Science*, 10(5):575–587, 1991.

[57] JS Davitt, TC Beals, and KN Bachus. The effects of medial and lateral displacement calcaneal osteotomies on ankle and subtalar joint pressure distribution. *Foot & Ankle International*, 22(11):885–889, 2001.

[58] SL Delp, JP Loan, MG Hoy, FE Zajac, EL Topp, and JM Rosen. An interactive graphics-based model of the lower extremity to study orthopaedic surgical procedures. *IEEE Transactions on Biomedical Engineering*, 37(8): 757–767, 1990.

[59] SL Delp, FC Anderson, AS Arnold, P Loan, A Habib, CT John, E Guendelman, and DG Thelen. Opensim: open-source software to create and analyze dynamic simulations of movement. *IEEE Transactions on Biomedical Engineering*, 54(11):1940–1950, 2007.

[60] SJ Dixon, RS Hinman, MW Creaby, G Kemp, and KM Crossley. Knee joint stiffness during walking in knee osteoarthritis. *Arthritis Care & Research: Official Journal of the American College of Rheumatology*, 62(1):38–44, 2010.

[61] DD D'Lima, S Patil, N Steklov, JE Slamin, and CW Colwell Jr. Tibial forces measured in vivo after total knee arthroplasty. *The Journal of Arthroplasty*, 21(2):255–262, 2006.

[62] MP Do Carmo. *Differential Geometry of Curves and Surfaces: Revised and Updated Second Edition*. Courier Dover Publications, 2016.

[63] TLH Donahue, ML Hull, MM Rashid, and CR Jacobs. A finite element model of the human knee joint for the study of tibio-femoral contact. *Journal of Biomechanical Engineering*, 124(3):273–280, 2002.

[64] HL Driscoll, JC Christensen, and AF Tencer. Contact characteristics of the ankle joint. part 1. the normal joint. *Journal of the American Podiatric Medical Association*, 84(10):491–498, 1994.

[65] R Dumas, R Aissaoui, D Mitton, W Skalli, and JA de Guise. Personalized body segment parameters from biplanar low-dose radiography. *IEEE Transactions on Biomedical Engineering*, 52(10):1756–1763, 2005.

[66] R Dumas, L Cheze, and JP Verriest. Adjustments to mcconville et al. and young et al. body segment inertial parameters. *Journal of Biomechanics*, 40 (3):543–553, 2007.

[67] L Edelsten, JE Jeffrey, LV Burgin, and RM Aspden. Viscoelastic deformation of articular cartilage during impact loading. *Soft Matter*, 6(20):5206–5212, 2010.

[68] WB Edwards, ED Ward, and TR Derrick. Foot joint pressures during dynamic gait simulation. *Journal of Foot and Ankle Research*, 1(1):O21, 2008.

[69] AJS Egea, M Valera, JMP Quiroga, I Proubasta, J Noailly, and D Lacroix. Impact of hip anatomical variations on the cartilage stress: a finite element analysis towards the biomechanical exploration of the factors that may explain primary hip arthritis in morphologically normal subjects. *Clinical Biomechanics*, 29(4):444–450, 2014.

[70] GY El-Khoury, KJ Alliman, HJ Lundberg, MJ Rudert, TD Brown, and CL Saltzman. Cartilage thickness in cadaveric ankles: measurement with double-contrast multi–detector row ct arthrography versus mr imaging. *Radiology*, 233(3):768–773, 2004.

[71] JJ Elias, DR Wilson, R Adamson, and AJ Cosgarea. Evaluation of a computational model used to predict the patellofemoral contact pressure distribution. *Journal of Biomechanics*, 37(3):295–302, 2004.

[72] KE Ensrud. Epidemiology of fracture risk with advancing age. *Journals of Gerontology Series A: Biomedical Sciences and Medical Sciences*, 68(10): 1236–1242, 2013.

[73] DT Felson, RC Lawrence, PA Dieppe, R Hirsch, CG Helmick, JM Jordan, RS Kington, NE Lane, MC Nevitt, Y Zhang, et al. Osteoarthritis: new insights. part 1: the disease and its risk factors. *Annals of Internal Medicine*, 133(8):635–646, 2000.

[74] M Ferrant, A Nabavi, B Macq, FA Jolesz, R Kikinis, and SK Warfield. Registration of 3-d intraoperative mr images of the brain using a finite-element biomechanical model. *IEEE Transactions on Medical Imaging*, 20(12): 1384–1397, 2001.

[75] DA Field. Laplacian smoothing and delaunay triangulations. *Communications in applied numerical methods*, 4(6):709–712, 1988.

[76] National Collaborating Centre for Chronic Conditions (Great Britain) and National Institute for Clinical Excellence (Great Britain). Osteoarthritis: national clinical guidelines for care and management in adults. Royal College of Physicians, 2008.

[77] AJS Fox, A Bedi, and SA Rodeo. The basic science of articular cartilage: structure, composition, and function. *Sports Health*, 1(6):461–468, 2009.

[78] R Franci, V Parenti Castelli, C Belvedere, and A Leardini. A new one-dof fully parallel mechanism for modelling passive motion at the human tibiotalar joint. *Journal of Biomechanics*, 42(10):1403–1408, 2009.

[79] BJ Fregly, TF Besier, DG Lloyd, SL Delp, SA Banks, MG Pandy, and DD D'lima. Grand challenge competition to predict in vivo knee loads. *Journal of Orthopaedic Research*, 30(4):503–513, 2012.

[80] YC Fung, P Tong, and X Chen. *Classical and computational solid mechanics*, volume 2. World Scientific Publishing Company, 2017.

[81] RZ Gan, B Feng, and Q Sun. Three-dimensional finite element modeling of human ear for sound transmission. *Annals of Biomedical Engineering*, 32 (6):847–859, 2004.

[82] AP Gandhamal, SN Talbar, SS Gajre, AM Hani, and D Kumar. Automatic and unsupervised femur and tibia segmentation using magnetic resonance images. *Osteoarthritis and Cartilage*, 25:S258, 2017.

[83] SB Gay and RJ Woodcock. *Radiology recall*, volume 15. Lippincott Williams & Wilkins, 1999.

[84] E Genda, N Konishi, Y Hasegawa, and T Miura. A computer simulation study of normal and abnormal hip joint contact pressure. *Archives of Orthopaedic and Trauma Surgery*, 114(4):202–206, 1995.

[85] E Genda, N Iwasaki, G Li, BA MacWilliams, PJ Barrance, and EYS Chao. Normal hip joint contact pressure distribution in single-leg standing - effect of gender and anatomic parameters. *Journal of Biomechanics*, 34(7):895–905, 2001.

[86] B Gilles, L Moccozet, and N Magnenat-Thalmann. Anatomical modelling of the musculoskeletal system from mri. In *International Conference on Medical Image Computing and Computer-Assisted Intervention*, pages 289–296. Springer, 2006.

[87] U Glitsch and W Baumann. The three-dimensional determination of internal loads in the lower extremity. *Journal of Biomechanics*, 30(11-12):1123–1131, 1997.

[88] MS Gockenbach. *Understanding and implementing the finite element method*, volume 97. Siam, 2006.

[89] MB Goldring and SR Goldring. Articular cartilage and subchondral bone in the pathogenesis of osteoarthritis. *Annals of the New York Academy of Sciences*, 1192(1):230–237, 2010.

[90] AS Greenwald and JJ O'Connor. The transmission of load through the human hip joint. *Journal of Biomechanics*, 4(6):507–528, 1971.

[91] KB Gu and LP Li. A human knee joint model considering fluid pressure and fiber orientation in cartilages and menisci. *Medical Engineering and Physics*, 33(4):497–503, 2011.

[92] ME Gurtin. The linear theory of elasticity. In *Linear Theories of Elasticity and Thermoelasticity*, pages 1–295. Springer, 1973.

[93] JA Gustafson. *Development and Validation of a Kinematically-Driven Computational Model of the Patellofemoral Joint*. PhD thesis, University of Pittsburgh, 2017.

[94] AJ Hamel, NA Sharkey, FL Buczek, and J Michelson. Relative motions of the tibia, talus, and calcaneus during the stance phase of gait: a cadaver study. *Gait & Posture*, 20(2):147–153, 2004.

[95] I Hannah, E Montefiori, L Modenese, J Prinold, M Viceconti, and C Mazza. Sensitivity of a juvenile subject-specific musculoskeletal model of the ankle joint to the variability of operator-dependent input. *Proceedings of the Institution of Mechanical Engineers, Part H: Journal of Engineering in Medicine*, 231(5):415–422, 2017.

[96] N Haraguchi, RS Armiger, MS Myerson, JT Campbell, and EYS Chao. Prediction of three-dimensional contact stress and ligament tension in the ankle during stance determined from computational modeling. *Foot & Ankle International*, 30(2):177–185, 2009.

[97] MD Harris, AE Anderson, CR Henak, BJ Ellis, CL Peters, and JA Weiss. Finite element prediction of cartilage contact stresses in normal human hips. *Journal of Orthopaedic Research*, 30(7):1133–1139, 2012.

[98] RT Hart, VV Hennebel, N Thongpreda, WC Van Buskirk, and RC Anderson. Modeling the biomechanics of the mandible: a three-dimensional finite element study. *Journal of Biomechanics*, 25(3):261–286, 1992.

[99] A Hayes, Y Tochigi, and CL Saltzman. Ankle morphometry on 3d-ct images. *The Iowa Orthopaedic Journal*, 26:1, 2006.

[100] WC Hayes and LF Mockros. Viscoelastic properties of human articular cartilage. *Journal of Applied Physiology*, 31(4):562–568, 1971.

[101] WC Hayes, LM Keer, G Herrmann, and LF Mockros. A mathematical analysis for indentation tests of articular cartilage. *Journal of Biomechanics*, 5(5): 541–551, 1972.

[102] WCl Hayes and AJ Bodine. Flow-independent viscoelastic properties of articular cartilage matrix. *Journal of Biomechanics*, 11(8-9):407–419, 1978.

[103] MO Heller, G Bergmann, G Deuretzbacher, L Dürselen, M Pohl, L Claes, NP Haas, and GN Duda. Musculo-skeletal loading conditions at the hip during walking and stair climbing. *Journal of Biomechanics*, 34(7):883–893, 2001.

[104] CR Henak, AE Anderson, and JA Weiss. Subject-specific analysis of joint contact mechanics: application to the study of osteoarthritis and surgical planning. *Journal of Biomechanical Engineering*, 135(2):021003, 2013.

[105] E Hernlund, A Svedbom, M Ivergård, J Compston, C Cooper, J Stenmark, EV McCloskey, B Jönsson, and JA Kanis. Osteoporosis in the european union: medical management, epidemiology and economic burden. *Archives of Osteoporosis*, 8(1-2):136, 2013.

[106] WA Hodge, RS Fijan, KL Carlson, RG Burgess, WH Harris, and RW Mann. Contact pressures in the human hip joint measured in vivo. *Proceedings of the National Academy of Sciences*, 83(9):2879–2883, 1986.

[107] JM Hootman, CG Helmick, KE Barbour, KA Theis, and MA Boring. Updated projected prevalence of self-reported doctor-diagnosed arthritis and arthritis-attributable activity limitation among us adults, 2015–2040. *Arthritis & Rheumatology*, 68(7):1582–1587, 2016.

[108] TJ Horgan and MD Gilchrist. The creation of three-dimensional finite element models for simulating head impact biomechanics. *International Journal of Crashworthiness*, 8(4):353–366, 2003.

[109] MDK Horsman, HFJM Koopman, FCT van der Helm, LP Prosé, and HEJ Veeger. Morphological muscle and joint parameters for musculoskeletal modelling of the lower extremity. *Clinical Biomechanics*, 22(2):239–247, 2007.

[110] KJ Hunt, Y Goeb, AW Behn, B Criswell, and L Chou. Ankle joint contact loads and displacement with progressive syndesmotic injury. *Foot & Ankle International*, 36(9):1095–1103, 2015.

[111] C Hurschler, J Emmerich, and N Wülker. In vitro simulation of stance phase gait part i: Model verification. *Foot & Ankle International*, 24(8): 614–622, 2003.

[112] NH Ibragimov. Integrating factors, adjoint equations and lagrangians. *Journal of Mathematical Analysis and Applications*, 318(2):742–757, 2006.

[113] A Iglič, VK Iglic, V Antolic, F Srakar, and U Stanic. Effect of the periacetabular osteotomy on the stress on the human hip joint articular surface. *IEEE Transactions on Rehabilitation Engineering*, 1(4):207–212, 1993.

[114] A Iglič, F Srakar, and V Antolic. Influence of the pelvic shape on the biomechanical status of the hip. *Clinical Biomechanics*, 8(4):223–224, 1993.

[115] A Iglič, V Kralj-Iglič, M Daniel, and A Maček-Lebar. Computer determination of contact stress distribution and size of weight bearing area in the human hip joint. *Computer Methods in Biomechanics & Biomedical Engineering*, 5(2):185–192, 2002.

[116] M Ipavec, RA Brand, DR Pedersen, B Mavčič, V Kralj-Iglič, and A Iglič. Mathematical modelling of stress in the hip during gait. *Journal of Biomechanics*, 32(11):1229–1235, 1999.

[117] Daniel A Jacobs and Daniel P Ferris. Estimation of ground reaction forces and ankle moment with multiple, low-cost sensors. *Journal of Neuroengineering and Rehabilitation*, 12(1):90, 2015.

[118] F Johannesdottir, KES Poole, J Reeve, K Siggeirsdottir, T Aspelund, B Mogensen, BY Jonsson, S Sigurdsson, TB Harris, VG Gudnason, et al. Distribution of cortical bone in the femoral neck and hip fracture: a prospective case-control analysis of 143 incident hip fractures; the ages-reykjavik study. *Bone*, 48(6):1268–1276, 2011.

[119] MP Kadaba, HK Ramakrishnan, and ME Wootten. Measurement of lower extremity kinematics during level walking. *Journal of Orthopaedic Research*, 8(3):383–392, 1990.

[120] AS Kelikian and SK Sarrafian. *Sarrafian's anatomy of the foot and ankle: descriptive, topographic, functional*. Lippincott Williams & Wilkins, 2011.

[121] GE Kempson, MAR Freeman, and SAV Swanson. The determination of a creep modulus for articular cartilage from indentation tests on the human femoral head. *Journal of Biomechanics*, 4(4):239–250, 1971.

[122] AM Kern and DD Anderson. Expedited patient-specific assessment of contact stress exposure in the ankle joint following definitive articular fracture reduction. *Journal of Biomechanics*, 48(12):3427–3432, 2015.

[123] JH Keyak and SA Rossi. Prediction of femoral fracture load using finite element models: an examination of stress-and strain-based failure theories. *Journal of Biomechanics*, 33(2):209–214, 2000.

[124] A Kharb, V Saini, YK Jain, and S Dhiman. A review of gait cycle and its parameters. *IJCEM International Journal of Computational Engineering & Management*, 13:78–83, 2011.

[125] A Kiapour, AM Kiapour, V Kaul, CE Quatman, SC Wordeman, TE Hewett, CK Demetropoulos, and VK Goel. Finite element model of the knee for investigation of injury mechanisms: development and validation. *Journal of Biomechanical Engineering*, 136(1):011002, 2014.

[126] SM Kidder, FS Abuzzahab, GF Harris, and JE Johnson. A system for the analysis of foot and ankle kinematics during gait. *IEEE Transactions on Rehabilitation Engineering*, 4(1):25–32, 1996.

[127] KJ Kim, E Uchiyama, HB Kitaoka, and KN An. An in vitro study of individual ankle muscle actions on the center of pressure. *Gait & Posture*, 17 (2):125–131, 2003.

[128] S Kim. Changes in surgical loads and economic burden of hip and knee replacements in the us: 1997–2004. *Arthritis Care & Research*, 59(4):481–488, 2008.

[129] M Kimizuka, H Kurosawa, and T Fukubayashi. Load-bearing pattern of the ankle joint. *Archives of Orthopaedic and Traumatic Surgery*, 96(1):45–49, 1980.

[130] YM Kirane, JD Michelson, and NA Sharkey. Evidence of isometric function of the flexor hallucis longus muscle in normal gait. *Journal of Biomechanics*, 41(9):1919–1928, 2008.

[131] RD Komistek, JB Stiehl, DA Dennis, RD Paxson, and RW Soutas-Little. Mathematical model of the lower extremity joint reaction forces using kane's method of dynamics. *Journal of Biomechanics*, 31(2):185–189, 1997.

[132] DE Krebs, L Elbaum, PO Riley, WA Hodge, and RW Mann. Exercise and gait effects on in vivo hip contact pressures. *Physical Therapy*, 71(4):301–309, 1991.

[133] H Kura, HB Kitaoka, ZP Luo, and KN An. Measurement of surface contact area of the ankle joint. *Clinical Biomechanics*, 13(4):365–370, 1998.

[134] SD Kwak, L Blankevoort, and GA Ateshian. A mathematical formulation for 3d quasi-static multibody models of diarthrodial joints. *Computer Methods in Biomechanics and Biomedical Engineering*, 3(1):41–64, 2000.

[135] OR Kwon, KT Kang, J Son, DS Suh, C Baek, and YG Koh. Importance of joint line preservation in unicompartmental knee arthroplasty: finite element analysis. *Journal of Orthopaedic Research*, 35(2):347–352, 2017.

[136] WM Lai, JS Hou, and VC Mow. A triphasic theory for the swelling and deformation behaviors of articular cartilage. *Journal of Biomechanical Engineering*, 113(3):245–258, 1991.

[137] TA Laursen. *Computational contact and impact mechanics: fundamentals of modeling interfacial phenomena in nonlinear finite element analysis*. Springer Science & Business Media, 2013.

[138] J Leal, AM Gray, D Prieto-Alhambra, NK Arden, C Cooper, MK Javaid, A Judge, REFReSH study group, et al. Impact of hip fracture on hospital care costs: a population-based study. *Osteoporosis International*, 27(2): 549–558, 2016.

[139] A Leardini, MG Benedetti, F Catani, L Simoncini, and S Giannini. An anatomically based protocol for the description of foot segment kinematics during gait. *Clinical Biomechanics*, 14(8):528–536, 1999.

[140] DG Lee and BL Davis. Assessment of the effects of diabetes on midfoot joint pressures using a robotic gait simulator. *Foot & Ankle International*, 30 (8):767–772, 2009.

[141] G Lenaerts, W Bartels, F Gelaude, M Mulier, A Spaepen, G Van der Perre, and I Jonkers. Subject-specific hip geometry and hip joint centre location affects calculated contact forces at the hip during gait. *Journal of Biomechanics*, 42(9):1246–1251, 2009.

[142] G Li, M Sakamoto, and EYS Chao. A comparison of different methods in predicting static pressure distribution in articulating joints. *Journal of Biomechanics*, 30(6):635–638, 1997.

[143] G Li, J Gil, A Kanamori, and SLY Woo. A validated three-dimensional computational model of a human knee joint. *Journal of Biomechanical Engineering*, 121(6):657–662, 1999.

[144] J Li, X Hua, Z Jin, J Fisher, and RK Wilcox. Biphasic investigation of contact mechanics in natural human hips during activities. *Proceedings of the Institution of Mechanical Engineers, Part H: Journal of Engineering in Medicine*, 228 (6):556–563, 2014.

[145] LP Li, J Soulhat, MD Buschmann, and A Shirazi-Adl. Nonlinear analysis of cartilage in unconfined ramp compression using a fibril reinforced poroelastic model. *Clinical Biomechanics*, 14(9):673–682, 1999.

[146] LP Li, MD Buschmann, and A Shirazi-Adl. Fibril stiffening accounts for strain-dependent stiffness of articular cartilage in unconfined compression. *Transactions of the Orthopaedic Research Society*, 26:425, 2001.

[147] W Li, DD Anderson, JK Goldsworthy, JL Marsh, and TD Brown. Patient-specific finite element analysis of chronic contact stress exposure after intraarticular fracture of the tibial plafond. *Journal of Orthopaedic Research*, 26(8):1039–1045, 2008.

[148] W Liu, S Siegler, H Hillstrom, and K Whitney. Three-dimensional, six-degrees-of-freedom kinematics of the human hindfoot during the stance phase of level walking. *Human Movement Science*, 16(2-3):283–298, 1997.

[149] VW Macko, LS Matthews, P Zwirkoski, and SA Goldstein. The joint-contact area of the ankle. the contribution of the posterior malleolus. *The Journal of Bone and Joint Surgery. American volume*, 73(3):347–351, 1991.

[150] BA MacWilliams, M Cowley, and DE Nicholson. Foot kinematics and kinetics during adolescent gait. *Gait & Posture*, 17(3):214–224, 2003.

[151] RL Magin and TJ Royston. Fractional-order elastic models of cartilage: A multi-scale approach. *Communications in nonlinear science and numerical simulation*, 15(3):657–664, 2010.

[152] TM Malaquias, C Silveira, W Aerts, F De Groote, G Dereymaeker, J Vander Sloten, and I Jonkers. Extended foot-ankle musculoskeletal models for application in movement analysis. *Computer Methods in Biomechanics and Biomedical Engineering*, 20(2):153–159, 2017.

[153] LP Maletsky, J Sun, and NA Morton. Accuracy of an optical active-marker system to track the relative motion of rigid bodies. *Journal of Biomechanics*, 40(3):682–685, 2007.

[154] S Martelli, F Taddei, A Cappello, S van Sint Jan, A Leardini, and M Viceconti. Effect of sub-optimal neuromotor control on the hip joint load during level walking. *Journal of Biomechanics*, 44(9):1716–1721, 2011.

[155] S Martelli, G Valente, M Viceconti, and F Taddei. Sensitivity of a subject-specific musculoskeletal model to the uncertainties on the joint axes location. *Computer methods in biomechanics and biomedical engineering*, 18(14): 1555–1563, 2015.

[156] JM Marzo and J Gurske-DePerio. Effects of medial meniscus posterior horn avulsion and repair on tibiofemoral contact area and peak contact pressure with clinical implications. *The American Journal of Sports Medicine*, 37(1):124–129, 2009.

[157] TE McAlindon, RR Bannuru, MC Sullivan, NK Arden, F Berenbaum, SM Bierma-Zeinstra, GA Hawker, Y Henrotin, DJ Hunter, H Kawaguchi, et al. Oarsi guidelines for the non-surgical management of knee osteoarthritis. *Osteoarthritis and Cartilage*, 22(3):363–388, 2014.

[158] SP Messier. Osteoarthritis of the knee and associated factors of age and obesity: effects on gait. *Medicine and Science in Sports and Exercise*, 26(12): 1446–1452, 1994.

[159] JM Michael, A Golshani, S Gargac, and T Goswami. Biomechanics of the ankle joint and clinical outcomes of total ankle replacement. *Journal of the Mechanical Behavior of Biomedical Materials*, 1(4):276–294, 2008.

[160] RE Miller, RJ Miller, and AM Malfait. Osteoarthritis joint pain: the cytokine connection. *Cytokine*, 70(2):185–193, 2014.

[161] SA Millington, M Grabner, R Wozelka, DD Anderson, SR Hurwitz, and JR Crandall. Quantification of ankle articular cartilage topography and thickness using a high resolution stereophotography system. *Osteoarthritis and Cartilage*, 15(2):205–211, 2007.

[162] L Modenese, ATM Phillips, and AMJ Bull. An open source lower limb model: hip joint validation. *Journal of Biomechanics*, 44(12):2185–2193, 2011.

[163] L Modenese, E Montefiori, A Wang, S Wesarg, M Viceconti, and C Mazzà. Investigation of the dependence of joint contact forces on musculotendon parameters using a codified workflow for image-based modelling. *Journal of Biomechanics*, 2018.

[164] T Möller and B Trumbore. Fast, minimum storage ray/triangle intersection. In *ACM SIGGRAPH 2005 Courses*, page 7. ACM, 2005.

[165] VC Mow and R Huiskes. *Basic orthopaedic biomechanics & mechano-biology*. Lippincott Williams & Wilkins, 2005.

[166] VC Mow and JM Mansour. The nonlinear interaction between cartilage deformation and interstitial fluid flow. *Journal of Biomechanics*, 10(1):31–39, 1977.

[167] VC Mow and M Rosenwasser. Articular cartilage: biomechanics. *Injury and Repair of the Musculoskeletal Soft Tissues*, 1:427–463, 1988.

[168] VC Mow, MH Holmes, and WM Lai. Fluid transport and mechanical properties of articular cartilage: a review. *Journal of Biomechanics*, 17(5):377–394, 1984.

[169] VC Mow, GA Ateshian, and A Ratcliffe. Anatomic form and biomechanical properties of articular cartilage of the knee joint. *Biology and Biomechanics of the Traumatized Synovial Joint: The Knee as a Model. 2nd ed. Rosemont, IL: American Academy of Orthopaedic Surgeons*, pages 55–81, 1992.

[170] KA Myers, M Wang, RM Marks, and GF Harris. Validation of a multisegment foot and ankle kinematic model for pediatric gait. *IEEE Transactions on neural systems and rehabilitation engineering*, 12(1):122–130, 2004.

[171] T Natsakis, K Peeters, F Burg, G Dereymaeker, J Vander Sloten, and I Jonkers. Specimen-specific tibial kinematics model for in vitro gait simulations. *Proceedings of the Institution of Mechanical Engineers, Part H: Journal of Engineering in Medicine*, 227(4):454–463, 2013.

[172] T Natsakis, J Burg, G Dereymaeker, I Jonkers, and J Vander Sloten. Inertial control as novel technique for in vitro gait simulations. *Journal of Biomechanics*, 48(2):392–395, 2015.

[173] T Natsakis, J Burg, G Dereymaeker, J Vander Sloten, and I Jonkers. Extrinsic muscle forces affect ankle loading before and after total ankle arthroplasty. *Clinical Orthopaedics and Related Research*, 473(9):3028–3037, 2015.

[174] T Natsakis, J Burg, G Dereymaeker, I Jonkers, and J Vander Sloten. Foot–ankle simulators: A tool to advance biomechanical understanding of a complex anatomical structure. *Proceedings of the Institution of Mechanical Engineers, Part H: Journal of Engineering in Medicine*, 230(5):440–449, 2016.

[175] RR Neptune. Optimization algorithm performance in determining optimal controls in human movement analyses. *Journal of Biomechanical Engineering*, 121(2):249–252, 1999.

[176] C Nester, RK Jones, A Liu, D Howard, A Lundberg, A Arndt, P Lundgren, A Stacoff, and P Wolf. Foot kinematics during walking measured using bone and surface mounted markers. *Journal of Biomechanics*, 40(15):3412–3423, 2007.

[177] I Newton. Philosophiæ naturalis principia mathematica, 1687; tr h, 1726.

[178] BM Nigg and W Herzog. *Biomechanics of the musculo-skeletal system*, volume 192. Wiley New York, 1999.

[179] LD Noble, RW Colbrunn, DG Lee, AJ Van Den Bogert, and BL Davis. Design and validation of a general purpose robotic testing system for musculoskeletal applications. *Journal of Biomechanical Engineering*, 132(2): 025001, 2010.

[180] General Assembly of the World Medical Association et al. World medical association declaration of helsinki: ethical principles for medical research involving human subjects. *The Journal of the American College of Dentists*, 81(3):14, 2014.

[181] N Okita, SA Meyers, JH Challis, and NA Sharkey. An objective evaluation of a segmented foot model. *Gait & Posture*, 30(1):27–34, 2009.

[182] AMH Paik, J Stebbins, A Kothari, and AB Zavatsky. Effect of marker placement on oxford foot model hindfoot segment axes. In *Journal of Foot and Ankle Research*, volume 7, page A62. BioMed Central, 2014.

[183] S Park, DE Krebs, and RW Mann. Hip muscle co-contraction: evidence from concurrent in vivo pressure measurement and force estimation. *Gait & Posture*, 10(3):211–222, 1999.

[184] JP Paul. Paper 8: forces transmitted by joints in the human body. In *Proceedings of the Institution of Mechanical Engineers, Conference Proceedings*, volume 181, pages 8–15. SAGE Publications Sage UK: London, England, 1966.

[185] SS Pawaskar, E Ingham, J Fisher, and Z Jin. Fluid load support and contact mechanics of hemiarthroplasty in the natural hip joint. *Medical Engineering and Physics*, 33(1):96–105, 2011.

[186] B Pearson and DM Espino. Effect of hydration on the frequency-dependent viscoelastic properties of articular cartilage. *Proceedings of the Institution of Mechanical Engineers, Part H: Journal of Engineering in Medicine*, 227(11): 1246–1252, 2013.

[187] K Peeters, T Natsakis, J Burg, P Spaepen, I Jonkers, G Dereymaeker, and J Vander Sloten. An in vitro approach to the evaluation of foot-ankle kinematics: performance evaluation of a custom-built gait simulator. *Proceedings of the Institution of Mechanical Engineers, Part H: Journal of Engineering in Medicine*, 227(9):955–967, 2013.

[188] JG Peyron. The epidemiology of osteoarthritis. *Osteoarthritis. Diagnosis and treatment.*, pages 9–27, 1984.

[189] DM Pierce, T Ricken, and GA Holzapfel. A hyperelastic biphasic fibre-reinforced model of articular cartilage considering distributed collagen fibre orientations: continuum basis, computational aspects and applications. *Computer Methods in Biomechanics and Biomedical Engineering*, 16 (12):1344–1361, 2013.

[190] DM Pierce, MJ Unterberger, W Trobin, T Ricken, and GA Holzapfel. A microstructurally based continuum model of cartilage viscoelasticity and permeability incorporating measured statistical fiber orientations. *Biomechanics and Modeling in Mechanobiology*, 15(1):229–244, 2016.

[191] P Pisani, MD Renna, F Conversano, E Casciaro, M Di Paola, E Quarta, M Muratore, and S Casciaro. Major osteoporotic fragility fractures: Risk

factor updates and societal impact. *World Journal of Orthopedics*, 7(3):171, 2016.

[192] P Pottecher, K Engelke, L Duchemin, O Museyko, T Moser, D Mitton, E Vicaut, J Adams, W Skalli, JD Laredo, et al. Prediction of hip failure load: in vitro study of 80 femurs using three imaging methods and finite element models—the european fracture study (effect). *Radiology*, 280(3): 837–847, 2016.

[193] JAI Prinold, C Mazzà, R Di Marco, I Hannah, C Malattia, S Magni-Manzoni, M Petrarca, AB Ronchetti, LT De Horatio, EHP van Dijkhuizen, et al. A patient-specific foot model for the estimate of ankle joint forces in patients with juvenile idiopathic arthritis. *Annals of Biomedical Engineering*, 44(1):247–257, 2016.

[194] P Procter and JP Paul. Ankle joint biomechanics. *Journal of Biomechanics*, 15(9):627–634, 1982.

[195] M Qasim, G Farinella, Ju Zhang, X Li, L Yang, R Eastell, and M Viceconti. Patient-specific finite element estimated femur strength as a predictor of the risk of hip fracture: the effect of methodological determinants. *Osteoporosis International*, 27(9):2815–2822, 2016.

[196] A Quarteroni. *Modellistica numerica per problemi differenziali*, volume 97. Springer, 2016.

[197] DK Ramsey and PF Wretenberg. Biomechanics of the knee: methodological considerations in the in vivo kinematic analysis of the tibiofemoral and patellofemoral joint. *Clinical Biomechanics*, 14(9):595–611, 1999.

[198] PL Ramsey and W Hamilton. Changes in tibiotalar area of contact caused by lateral talar shift. *The Journal of Bone and Joint Surgery. American volume*, 58(3):356–357, 1976.

[199] DJ Rapperport, DR Carter, and DJ Schurman. Contact finite element stress analysis of the hip joint. *Journal of Orthopaedic Research*, 3(4):435–446, 1985.

[200] U Rattanaprasert, R Smith, M Sullivan, and W Gilleard. Three-dimensional kinematics of the forefoot, rearfoot, and leg without the function of tibialis posterior in comparison with normals during stance phase of walking. *Clinical Biomechanics*, 14(1):14–23, 1999.

[201] H Röhrle, R Scholten, C Sigolotto, W Sollbach, and H Kellner. Joint forces in the human pelvis-leg skeleton during walking. *Journal of Biomechanics*, 17(6):409–424, 1984.

[202] D Roylance. Engineering viscoelasticity. *Department of Materials Science and Engineering–Massachusetts Institute of Technology, Cambridge MA*, 2139: 1–37, 2001.

[203] LZ Rubenstein. Falls in older people: epidemiology, risk factors and strategies for prevention. *Age and Ageing*, 35(suppl_2):ii37–ii41, 2006.

[204] ME Russell, KH Shivanna, NM Grosland, and DR Pedersen. Cartilage contact pressure elevations in dysplastic hips: a chronic overload model. *Journal of Orthopaedic Surgery and Research*, 1(1):6, 2006.

[205] CL Saltzman, ML Salamon, GM Blanchard, T Huff, A Hayes, JA Buckwalter, and A Amendola. Epidemiology of ankle arthritis: report of a consecutive series of 639 patients from a tertiary orthopaedic center. *The Iowa Orthopaedic Journal*, 25:44, 2005.

[206] A Sands, C White, M Blankstein, I Zderic, D Wahl, M Ernst, M Windolf, JE Hagen, RG Richards, K Stoffel, et al. Assessment of ankle and hindfoot stability and joint pressures using a human cadaveric model of a large lateral talar process excision: A biomechanical study. *Medicine*, 94(11), 2015.

[207] A Schmitz and D Piovesan. Development of an open-source, discrete element knee model. *IEEE Transactions on Biomedical Engineering*, 63(10): 2056–2067, 2016.

[208] S Schutte, SPW van den Bedem, F van Keulen, FCT van der Helm, and HJ Simonsz. A finite-element analysis model of orbital biomechanics. *Vision Research*, 46(11):1724–1731, 2006.

[209] SH Scott and DA Winter. Biomechanical model of the human foot: kinematics and kinetics during the stance phase of walking. *Journal of Biomechanics*, 26(9):1091–1104, 1993.

[210] A Seireg and RJ Arvikar. A mathematical model for evaluation of forces in lower extremeties of the musculo-skeletal system. *Journal of Biomechanics*, 6(3):313–322, 1973.

[211] A Seireg and RJ Arvikar. The prediction of muscular load sharing and joint forces in the lower extremities during walking. *Journal of Biomechanics*, 8 (2):89–102, 1975.

[212] FT Sheehan, AR Seisler, and KL Siegel. In vivo talocrural and subtalar kinematics: a non-invasive 3d dynamic mri study. *Foot & Ankle International*, 28(3):323–335, 2007.

[213] S Siegler, J Block, and CD Schneck. The mechanical characteristics of the collateral ligaments of the human ankle joint. *Foot & Ankle*, 8(5):234–242, 1988.

[214] S Siegler, JK Udupa, SI Ringleb, CW Imhauser, BE Hirsch, D Odhner, PK Saha, E Okereke, and N Roach. Mechanics of the ankle and subtalar joints revealed through a 3d quasi-static stress mri technique. *Journal of Biomechanics*, 38(3):567–578, 2005.

[215] J Simon, D Metaxiotis, A Siebel, HG Bock, and L Döderlein. A model of the human foot with seven segments. *Gait Posture*, 12:63–4, 2000.

[216] WR Smith, PF Stahel, BH Ziran, and JO Anglen. Locking plates: tips and tricks. *The Journal of Bone and Joint Surgery. American volume*, 89(10):2297–2307, 2007.

[217] M Sofonea and A Matei. *Mathematical models in contact mechanics*, volume 398. Cambridge University Press, 2012.

[218] BW Stansfield, AC Nicol, JP Paul, IG Kelly, F Graichen, and G Bergmann. Direct comparison of calculated hip joint contact forces with those measured using instrumented implants. an evaluation of a three-dimensional mathematical model of the lower limb. *Journal of Biomechanics*, 36(7):929–936, 2003.

[219] RN Stauffer, EYS Chao, and RC Brewster. Force and motion analysis of the normal, diseased, and prosthetic ankle joint. *Clinical Orthopaedics and Related Research*, (127):189–196, 1977.

[220] J Stebbins, M Harrington, N Thompson, A Zavatsky, and T Theologis. Repeatability of a model for measuring multi-segment foot kinematics in children. *Gait & Posture*, 23(4):401–410, 2006.

[221] KM Steele, MS DeMers, MH Schwartz, and SL Delp. Compressive tibiofemoral force during crouch gait. *Gait & Posture*, 35(4):556–560, 2012.

[222] SJ Steffensmeier, KS Berbaum, and TD Brown. Effects of medial and lateral displacement calcaneal osteotomies on tibiotalar joint contact stresses. *Journal of Orthopaedic Research*, 14(6):980–985, 1996.

[223] S Steger, M Kirschner, and S Wesarg. Articulated atlas for segmentation of the skeleton from head & neck ct datasets. In *Biomedical Imaging (ISBI), 2012 9th IEEE International Symposium on*, pages 1256–1259. IEEE, 2012.

[224] A Suckel, O Muller, N Wachter, and T Kluba. In vitro measurement of intraarticular pressure in the ankle joint. *Knee Surgery, Sports Traumatology, Arthroscopy*, 18(5):664–668, 2010.

[225] EM Suero, Y Sabbagh, R Westphal, N Hawi, M Citak, FM Wahl, C Krettek, and E Liodakis. Effect of medial opening wedge high tibial osteotomy on intraarticular knee and ankle contact pressures. *Journal of Orthopaedic Research*, 33(4):598–604, 2015.

[226] JK Suh and S Bai. Finite element formulation of biphasic poroviscoelastic model for articular cartilage. *Journal of Biomechanical Engineering*, 120(2): 195–201, 1998.

[227] DK Temple, AA Cederlund, BM Lawless, RM Aspden, and DM Espino. Viscoelastic properties of human and bovine articular cartilage: a comparison of frequency-dependent trends. *BMC Musculoskeletal Disorders*, 17(1): 419, 2016.

[228] D Testi, M Viceconti, F Baruffaldi, and A Cappello. Risk of fracture in elderly patients: a new predictive index based on bone mineral density and finite element analysis. *Computer Methods and Programs in Biomedicine*, 60 (1):23–33, 1999.

[229] DB Thordarson, S Motamed, T Hedman, E Ebramzadeh, and S Bakshian. The effect of fibular malreduction on contact pressures in an ankle fracture malunion model. *The Journal of Bone and Joint Surgery. American volume*, 79 (12):1809–1815, 1997.

[230] Y Tochigi, MJ Rudert, CL Saltzman, A Amendola, and TD Brown. Contribution of articular surface geometry to ankle stabilization. *The Journal of Bone and Joint Surgery. American volume*, 88(12):2704–2713, 2006.

[231] KC Townsend, HD Thomas-Aitken, MJ Rudert, AM Kern, MC Willey, DD Anderson, and JE Goetz. Discrete element analysis is a valid method for computing joint contact stress in the hip before and after acetabular fracture. *Journal of Biomechanics*, 67:9–17, 2018.

[232] TY Tsai, JS Li, S Wang, D Scarborough, and YM Kwon. In-vivo 6 degrees-of-freedom kinematics of metal-on-polyethylene total hip arthroplasty during gait. *Journal of Biomechanics*, 47(7):1572–1576, 2014.

[233] NW Tschoegl. *The phenomenological theory of linear viscoelastic behavior: an introduction*. Springer Science & Business Media, 2012.

[234] IJ Udofia, A Yew, and ZM Jin. Contact mechanics analysis of metal-on-metal hip resurfacing prostheses. *Proceedings of the Institution of Mechanical Engineers, Part H: Journal of Engineering in Medicine*, 218(5):293–305, 2004.

[235] V Valderrabano, M Horisberger, I Russell, H Dougall, and B Hintermann. Etiology of ankle osteoarthritis. *Clinical Orthopaedics and Related Research*, 467(7):1800, 2009.

[236] G Valente, L Pitto, D Testi, A Seth, SL Delp, R Stagni, M Viceconti, and F Taddei. Are subject-specific musculoskeletal models robust to the uncertainties in parameter identification? *PLoS One*, 9(11):e112625, 2014.

[237] G Valente, G Crimi, N Vanella, E Schileo, and F Taddei. nmsbuilder: Freeware to create subject-specific musculoskeletal models for opensim. *Computer Methods and Programs in Biomedicine*, 152:85–92, 2017.

[238] M Viceconti. *Multiscale modeling of the skeletal system*. Cambridge University Press, 2012.

[239] M Viceconti, M Davinelli, F Taddei, and A Cappello. Automatic generation of accurate subject-specific bone finite element models to be used in clinical studies. *Journal of Biomechanics*, 37(10):1597–1605, 2004.

[240] M Viceconti, F Taddei, SVS Jan, A Leardini, L Cristofolini, S Stea, F Baruffaldi, and M Baleani. Multiscale modelling of the skeleton for the prediction of the risk of fracture. *Clinical Biomechanics*, 23(7):845–852, 2008.

[241] KY Volokh, EYS Chao, and M Armand. On foundations of discrete element analysis of contact in diarthrodial joints. *Molecular & Cellular Biomechanics: MCB*, 4(2):67, 2007.

[242] M Vrahas, F Fu, and B Veenis. Intraarticular contact stresses with simulated ankle malunions. *Journal of Orthopaedic Trauma*, 8(2):159–166, 1994.

[243] M Wagner, A Frenk, and R Frigg. New concepts for bone fracture treatment and the locking compression plate. *Surgical Technology International*, 12: 271–277, 2004.

[244] L Wan, RJ De Asla, HE Rubash, and G Li. Determination of in-vivo articular cartilage contact areas of human talocrural joint under weight bearing conditions. *Osteoarthritis and Cartilage*, 14(12):1294–1301, 2006.

[245] L Wan, RJ de Asla, HE Rubash, and G Li. In vivo cartilage contact deformation of human ankle joints under full body weight. *Journal of Orthopaedic Research*, 26(8):1081–1089, 2008.

[246] CL Wang, CK Cheng, CW Chen, CM Lu, YS Hang, and TK Liu. Contact areas and pressure distributions in the subtalar joint. *Journal of Biomechanics*, 28(3):269–279, 1995.

[247] G Wang, W Huang, Q Song, and J Liang. Three-dimensional finite analysis of acetabular contact pressure and contact area during normal walking. *Asian Journal of Surgery*, 40(6):463–469, 2017.

[248] R Warwick, PL Williams, and H Gray. *Gray's anatomy*. Longman, 1973.

[249] K Watanabe, HB Kitaoka, LJ Berglund, KD Zhao, KR Kaufman, and KN An. The role of ankle ligaments and articular geometry in stabilizing the ankle. *Clinical Biomechanics*, 27(2):189–195, 2012.

[250] H Weinans, DR Sumner, R Igloria, and RN Natarajan. Sensitivity of periprosthetic stress-shielding to load and the bone density–modulus relationship in subject-specific finite element models. *Journal of Biomechanics*, 33(7):809–817, 2000.

[251] MW Whittle. Gait analysis: an introduction. 2007. *Heidi Harrison*, pages 47–100.

[252] HJ Wilke, P Neef, M Caimi, T Hoogland, and LE Claes. New in vivo measurements of pressures in the intervertebral disc in daily life. *Spine*, 24(8): 755–762, 1999.

[253] G Windisch, B Odehnal, R Reimann, F Anderhuber, and H Stachel. Contact areas of the tibiotalar joint. *Journal of Orthopaedic Research*, 25(11): 1481–1487, 2007.

[254] DA Winter. *Biomechanics and motor control of human movement*. John Wiley & Sons, 2009.

[255] DA Winter, AE Patla, M Ishac, and WH Gage. Motor mechanisms of balance during quiet standing. *Journal of Electromyography and Kinesiology*, 13 (1):49–56, 2003.

[256] SLY Woo, WH Akeson, and GF Jemmott. Measurements of nonhomogeneous, directional mechanical properties of articular cartilage in tension. *Journal of Biomechanics*, 9(12):785–791, 1976.

[257] P Wriggers and TA Laursen. *Computational contact mechanics*, volume 2. Springer, 2006.

[258] G Wu, S Siegler, P Allard, C Kirtley, A Leardini, D Rosenbaum, M Whittle, DD D'Lima, L Cristofolini, H Witte, et al. Isb recommendation on definitions of joint coordinate system of various joints for the reporting of human joint motion—part i: ankle, hip, and spine. *Journal of Biomechanics*, 35(4): 543–548, 2002.

[259] H Yoshida, A Faust, J Wilckens, M Kitagawa, J Fetto, and EYS Chao. Three-dimensional dynamic hip contact area and pressure distribution during activities of daily living. *Journal of Biomechanics*, 39(11):1996–2004, 2006.

[260] H Zwipp and T Randt. Ankle joint biomechanics. *Foot and Ankle Surgery*, 1(1):21–27, 1994.

A MATLAB code

This appendix contains a simplified version of some of the developed MATLAB code used for the simulations in Chapter 5.

A.1 Main

```
tic
clear
close all
clc
%% Load the kinematics, pressure and transformation
    matrices for the STL files
subject_id=37;
muscle_id=[1 2 5];
input_path=strcat('C:\Users\uos\Dropbox\
    University_and_PhD\Multiscale_modelling\Writing\
    Leuven\Data\Simulation\input\foot',num2str(
    subject_id),'\');
output_path=strcat('C:\Users\uos\Dropbox\
    University_and_PhD\Multiscale_modelling\Writing\
    Leuven\Data\Simulation\output\foot',num2str(
    subject_id),'\');
```

```
load(strcat(input_path,'Kinematics_foot',num2str(
    subject_id),'.mat'));
load(strcat(input_path,'Pressure_foot',num2str(
    subject_id),'.mat'));
load(strcat(input_path,'TransformationMatrices_foot',
    num2str(subject_id),'.mat'));
load(strcat(input_path,'sensor_faces'));
load(strcat(input_path,'musclesvoet',num2str(
    subject_id),'.mat'));

%% Load the faces and vertices of the STL files
[V_Tib, FixFaces] = stlRead(strcat(input_path,'
    Tibia_extreme_cut_malleolus1.stl'));
[V_Tal, F_Tal] = stlRead(strcat(input_path,'Talus.stl'
    ));
%% Obtain the sensor mesh in STL
[MobileVertices, MobileFaces] = obtain_reduced_mesh(
    Vertices.Talus,V_Tal,F_Tal,valid_triangle);
[MobileVertices, MobileFaces] = stlRead(strcat(
    input_path,'talus_sub35.stl'));
%% Load muscle attachment points in STL
load('attach_muscles.mat');
%% Move bodies to HOME
V_Tal_Home = transformVector(inv(transfomat_StlBone.
    Tekscan.Tibia),MobileVertices);
V_Tib_Home = transformVector(inv(transfomat_StlBone.
    Tekscan.Tibia),V_Tib);
% Put muscles in home
gastroc_home=transformVector(inv(transfomat_StlBone.
    Tekscan.Tibia),gastroc);
tib_ant_home=transformVector(inv(transfomat_StlBone.
    Tekscan.Tibia),tib_ant);
tib_post_home=transformVector(inv(transfomat_StlBone.
    Tekscan.Tibia),tib_post);
%% Input definition: Tibia
geom.tibia.vertices=V_Tib_Home;
geom.tibia.faces=FixFaces;
%% Input definition: Talus (in Tibia home)
geom.talus.vertices=V_Tal_Home;
geom.talus.faces=MobileFaces;
```

```
geom.talus.centre=zeros(1,3);
%% Input definition: muscles
muscles.tib_post_home=tib_post_home;
muscles.tib_ant_home=tib_ant_home;
muscles.gastroc_home=gastroc_home;
muscles.muscle_id=muscle_id;
%% Input definition: reference frames
reference_frames.R_Tal_Home=R_Tal_Home;
reference_frames.R_Tal=R_Tal;
%% Input definition: material properties and gap
N=length(MobileFaces);
material_prop.Ey=ones(N,1)*10.35e6;
material_prop.nu=0.42;
material_prop.ks=ones(N,1)*1e3*0;
gap=3.5;
%% Input definition: force
time_max=100;
musclesvoet37=musclesvoet37(1:time_max,:);
%% RUN SIMULATION AND SAVE RESULTS
output=Hammurabi(gap,reference_frames,
    transfomat_ProxDist,transfomat_StlBone,
    musclesvoet37,muscles,geom,material_prop);
toc
```

A.2 Solver

```
function [output] = Hammurabi(gap,reference_frames,
    transfomat_ProxDist,transfomat_StlBone,
    musclesvoet37,muscles,geom,material_prop)
%% DEFINE time_max
time_max=size(musclesvoet37,1);
%% IMPORT MESHES
% Tibia
V_Tib_Home = geom.tibia.vertices;
FixFaces = geom.tibia.faces;
% Talus
V_Tal_Home = geom.talus.vertices;
MobileFaces = geom.talus.faces;
N=length(MobileFaces);
% Talus centre
MobileCentre=geom.talus.centre;
```

```
%% PRELOAD
fprevious=zeros(3,N);
%% IMPORT REFERENCE FRAMES
R_Tal_Home=reference_frames.R_Tal_Home;
R_Tal=reference_frames.R_Tal;
%% IMPORT MATERIAL PROPERTIES
Ey=material_prop.Ey;
nu=material_prop.nu;
%% DEFINE OUTPUT
stressStory=zeros(N,time_max);
dispStory=zeros(6,time_max);
hstory=zeros(N,time_max);
CentreStory=zeros(3,time_max);
CentreStory(:,1)=MobileCentre';
keepstory=zeros(N,time_max);
spring_story=zeros(length(MobileFaces),3,time_max);
maxStress=zeros(1,time_max);
activeArea=zeros(1,time_max);
diff_err=zeros(1,time_max);
iter_story=zeros(1,time_max);
activeElem=zeros(1,time_max);
kin = zeros(4,4,time_max);
%% MUSCLE ATTACHMENT POINTS
tib_post_home = muscles.tib_post_home;
tib_ant_home = muscles.tib_ant_home;
gastroc_home = muscles.gastroc_home;
muscle_id=muscles.muscle_id;
%% FOR CYCLE
U=zeros(6,1);
for k=1:time_max

    % Input transformation matrix
    T=transfomat_ProxDist.Tekscan.Tekscan_10.
        Tibia_Talus{k};
    % Obtain the input kinematic position
    R_Tal_New=transformVector(T,transformVector(inv(
        transfomat_StlBone.Tekscan.Talus),R_Tal));
    % Compute transformation matrix between the
        kinematics position and talus in Tibia Home
    TT=transform_reference_frames(R_Tal_Home,R_Tal_New
        );
```

```
kin(:,:,k)=TT';
% Obtain desired position of the talus
VV_Tal_New=transformVector(TT',V_Tal_Home);
VV_Tal_New=VV_Tal_New+repmat(sum(dispStory(1:3,:)
    ,2)',size(VV_Tal_New,1),1);
% Obtain final muscle attachments
tib_post_kin=[tib_post_home(1,:);transformVector(
    TT',tib_post_home(2,:))];
tib_ant_kin=[tib_ant_home(1,:);transformVector(TT
    ',tib_ant_home(2,:))];
gastroc_kin=[gastroc_home(1,:);transformVector(TT
    ',gastroc_home(2,:))];
% Compute force
F=compute_force(tib_post_kin,tib_ant_kin,
    gastroc_kin,musclesvoet37(k,muscle_id))/2*scal(
    k);
%% LOAD BEARING ELEMENTS
% Define springs
MMobileSprings=ComputeSprings(VV_Tal_New,
    MobileFaces);
% Define direction of normal vectors to mobile
    body
[Area,NormalMatrix]=ComputeArea(VV_Tal_New,
    MobileFaces,MMobileSprings);
%% Store configuration at time k
mobile_story(:,:,k)=VV_Tal_New;
spring_story(:,:,k)=MMobileSprings;
%% Compute cartilage thickness
h=zeros(length(MMobileSprings),1);
parfor i=1:N
    [intersect,t, ~, ~]=TriangleRayIntersection(
        MMobileSprings(i,:),NormalMatrix(i,:),
        V_Tib_Home(FixFaces(:,1),:),V_Tib_Home(
        FixFaces(:,2),:),V_Tib_Home(FixFaces(:,3)
        ,:));
    if sum(intersect)>0
        h(i)=min(t(intersect==1));
    end
end
% Define service variables
keep=h>0;
```

```
hh=h;
keep(h>gap)=0;
h(h==0)=Inf;

updateElem=keep>0;
NormalStress=-ones(N,1);

% Define normal stiffness of the cartilage
kd=(1-nu)/((1+nu)*(1-2*nu))*Ey.*Area./h;
% Import shear stiffness of the cartilage
ks=material_prop.ks;
%% COMPUTE SOLUTION
iteration=0;

while (find(NormalStress<0)~=0)

    % Construct cartilage matrices
    [BB,DD]=BDMatrices(MMobileSprings,MobileCentre
        ,NormalMatrix,kd,ks,updateElem,keep);
    % Construct stiffness matrices
    Kprov=GlobalMatrix(BB,DD);

    % Define applied force
    Fprevious=[sum(fprevious')';zeros(3,1)];
    F=[F';zeros(3,1)];
    U=Kprov\(F-Fprevious);

    %% Compute cartilage and ligament forces
    [f,NormalStress,updateElem,fprevious]=
        ComputeForceStress(BB,DD,NormalMatrix,U,
        fprevious,updateElem,Area);
    iteration=iteration+1;
end
diff_err(k)=norm(sum(f')'-F(1:3));
iter_story(k)=iteration;
activeElem(k)=sum(keep);
dispStory(:,k)=U;
maxStress(k)=max(NormalStress)*1e6;
normF(k)=norm(F);
normfcart(k)=norm(sum(f')');
max_pressure_location(k)=find(NormalStress==max(
```

```
        NormalStress));
    activeArea(k)=Area'*updateElem;
    hstory(:,k)=hh;
    keepstory(:,k)=keep;
    Fstory(:,k)=F;
    updateStory(k)=sum(updateElem);
    % Update status
    fprevious=f;
    CentreStory(:,k+1)=MobileCentre'+U(1:3);


    clc
    % PROGRESS BAR
    cprintf('*blue',strcat(repmat('=',1,k),''));
    cprintf('*err',strcat(repmat('=',1,time_max-k),'\n
        '));

end

output.stressStory=stressStory;
output.dispStory=dispStory;
output.activeElem=activeElem;
output.hstory=hstory;
output.CentreStory=CentreStory;
output.keepstory=keepstory;
output.mobile_story=mobile_story;
output.spring_story=spring_story;
output.maxStress=maxStress;
output.activeArea=activeArea;
output.updateStory=updateStory;
output.diff_err=diff_err;
output.normF=normF;
output.mob_faces=MobileFaces;
output.fix_faces=FixFaces;
output.Fstory=Fstory;
output.normfcart=normfcart;
output.max_pressure_location=max_pressure_location;
output.iter_story=iter_story;
output.kin=kin;
output.Area=Area;
end
```

A.3 Meshing

```
function [V_Talus, F_Talus] = obtain_reduced_mesh(
    Vertices_Talus,V_Tal_Home,F_Tal,valid_triangle)

vertices = unique(Vertices_Talus);
sensor_points=V_Tal_Home(vertices,:);
F_Sensor = F_Tal(valid_triangle,:);
for i=1:size(F_Sensor,1)
    c(i,1)=find(vertices==F_Sensor(i,1));
    c(i,2)=find(vertices==F_Sensor(i,2));
    c(i,3)=find(vertices==F_Sensor(i,3));
end
V_Talus=sensor_points;
F_Talus=c;
```

A.4 Linear transformations

```
function T = transform_reference_frames(Rinitial,
    Rtarget)

RinitialOrigin=plot_in_the_origin(Rinitial,1,1,0);
RtargetOrigin=plot_in_the_origin(Rtarget,1,1,0);
Rot = RtargetOrigin*inv(RinitialOrigin);
transl= Rtarget(1,:)'-Rinitial(1,:)';
T=[Rot transl/2; 0 0 0 1];

function V = transformVector(M, V)
V = M*[V'; ones(1,size(V,1))];
V = V(1:3,:)';
end
```

A.5 Attachment points

```
function springs=ComputeSprings(V,F)
for i=1:size(F,1)
    springs(i,:)=mean(V(F(i,:),:));
end
```

A.6 Areas

```
function [Area,NormalMatrix]=ComputeArea(FemurVertices
    ,FemurFaces,FemurSprings)

tol=1e-9;
N=length(FemurSprings);
NormalMatrix=zeros(N,3);
Area=zeros(N,1);

parfor i=1:size(FemurFaces,1)
    Vface=FemurVertices(FemurFaces(i,:),:);
    v1=Vface(2,:)-Vface(1,:);
    v2=Vface(3,:)-Vface(1,:);
    % Compute area
    Area(i)=0.5*norm(cross(v1,v2));
    % Normal vector
    normal=cross(v1,v2)/norm(cross(v1,v2));
    % Check outer normal
    if normal*FemurSprings(i,:)'<0
        normal=-normal;
    end

    % Assemble output
    if Area(i)<=tol
        NormalMatrix(i,:)=zeros(1,3);
    else
        NormalMatrix(i,:)=normal;
    end

end
```

A.7 Local matrices

```
function [B,D]= BDMatrices(MMobileSprings,MobileCentre
    ,NormalMatrix,kd,ks,updateElem,keep)

% Number of elements
N=length(MMobileSprings);
% B and D
B=zeros(3,6*N);
D=zeros(3,3*N);
for i=0:N-1
```

```
    if keep(i+1)==1
        % Local B matrix
        Bi=[eye(3) [0 0 0; 0 0 -1; 0 1 0]*(
            MMobileSprings(i+1,1:3)-MobileCentre)' [0 0
             1; 0 0 0; -1 0 0]*(MMobileSprings(i+1,1:3)
            -MobileCentre)' [0 -1 0; 1 0 0; 0 0 0]*(
            MMobileSprings(i+1,1:3)-MobileCentre)']*
            updateElem(i+1);
        % Unit i-th spring
        ni=NormalMatrix(:,i+1);
        % i-th projector
        Di=kd(i+1)*ni*ni'+ks(i+1)*(eye(3)-ni*ni');
    else
        % Eliminate stretched springs
        Di=zeros(3);
        Bi=zeros(3,6);
    end
    % Assemble
    D(:,i*3+1:(i+1)*3)=Di;
    B(:,i*6+1:(i+1)*6)=Bi;
end
```

A.8 Stiffness matrix

```
function K=GlobalMatrix(B,D)

% Number of springs and initialisation
N=length(B)/6;
K=zeros(6);
% Integrate
for i=0:N-1
    % Local matrices
    Bi=B(:,i*6+1:(i+1)*6);
    Di=D(:,i*3+1:(i+1)*3);
    % Individual contribution
    Ki=(Bi'*Di*Bi);
    % Sum
    K=K+Ki;

end
```

A.9 Pressure computation

```
function [f,NormalStress,updateElem,fprevious]=
    ComputeForceStress(BB,DD,NormalMatrix,U,fprevious,
    updateElem,Area)
N=length(BB)/6;
f=zeros(3,N);
NormalStress=zeros(N,1);
for i=0:N-1
    % Force in the i-th spring
    felastic=DD(:,i*3+1:(i+1)*3)*BB(:,i*6+1:(i+1)*6)*U
        *updateElem(i+1);
    f(:,i+1)=felastic+fprevious(:,i+1);
    % Pressure
    NormalStress(i+1)=NormalMatrix(:,i+1)'*f(:,i+1)/
        Area(i+1); % This is the pressure on the i-th
        spring

end
% Eliminate stretched springs for the next iteration
updateElem(NormalStress<=0)=0;
end
```

B

Publications and presentations from this thesis

B.1 Full papers on scientific journals

- Benemerito, I., Modenese, L., Montefiori, E., Mazzà, C., Viceconti, M., Lacroix, D., Guo, L.: *Extended discrete element method can evaluate the effect of time dependency and translation of the talus on the estimation of cartilage pressure at the ankle joint,* submitted to Journal of Applied Biomechanics (2018).

B.2 Oral presentations in conferences

- Benemerito, I., Modenese, L., Montefiori, E., Mazzà, C., Viceconti, M., Lacroix, D., Guo, L.: *Evaluation of joint contact pressure in four subject specific discrete element based models of the ankle joint,* 8th World Congress of Biomechanics, July 2018, Dublin, Ireland.
- Benemerito, I., Modenese, L., Montefiori, E., Viceconti, M., Lacroix, D., Guo, L.: *Computation of joint contact pressure in a patient specific ankle model,* 26th Congress of the International Society of Biomechanics, July 2017, Brisbane, Australia.

- Benemerito, I., Lacroix, D., Guo, L.: *A comparison of elastic and viscoelastic hip contact models by using extended discrete element method*, 23rd Congress of the European Society of Biomechanics, July 2017, Seville, Spain.
- Benemerito, I., Lacroix, D., Guo, L.: *A nonlinear optimisation approach to compute the contact pressure in the hip during walking*, 22nd Congress of the European Society of Biomechanics, July 2016, Lyon, France.

B.3 Poster presentations in conferences

- Mengoni, M., Benemerito, I., Lu, Y., Guo, L.: *Reduced-order modelling of periprosthetic bone remodelling for joint replacements*, 22nd Congress of the European Society of Biomechanics, July 2016, Lyon, France